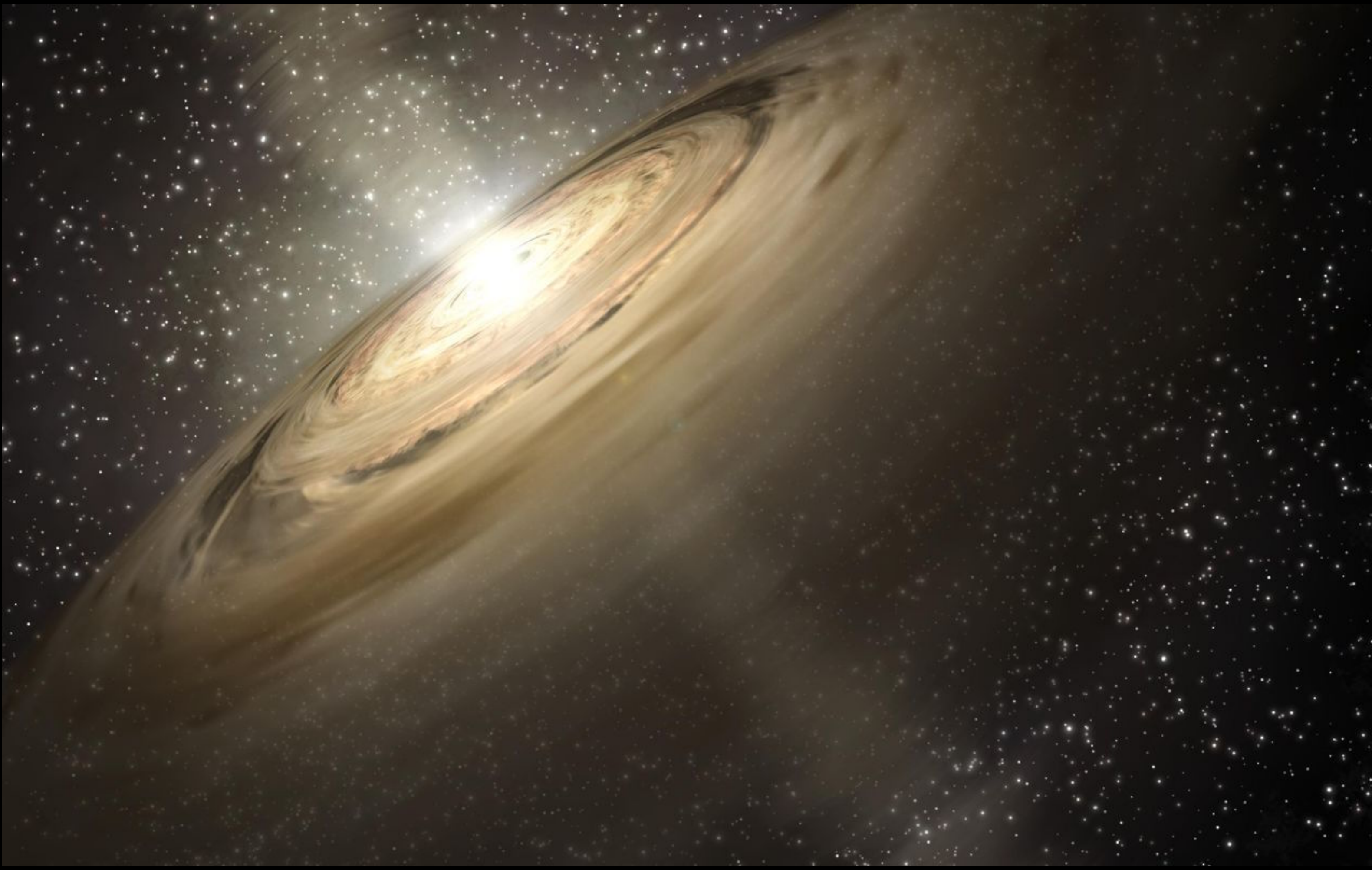

High Resolution Simulations of Structure Formation in Turbulent Protoplanetary Disks

A Case Study of the Vertical Shear Instability

Natascha Manger

2019

Dissertation
submitted to the
Combined Faculties for the Natural Sciences and for Mathematics
of the Ruperto-Carola University of Heidelberg, Germany
for the degree of
Doctor of Natural Sciences

Put forward by
M.Sc. NATASCHA MANGER
born in NEUSTADT A.D. WEINSTRASSE, GERMANY
Oral examination: 16.07.2019

High Resolution Simulations of Structure Formation in Turbulent Protoplanetary Disks

A Case Study of the Vertical Shear Instability

Referees:	apl. Prof. Dr. H. Hubertus Klahr Prof. Dr. Cornelis P. Dullemond

Abstract

Disks around young stars are the birth place of planetary systems like our own solar system. Thus, the study of turbulent processes in protoplanetary disks is not only important to understand the transport of angular momentum to explain for example the angular momentum deficit of our own sun, but also to understand how large scale structures emerge, which are recently regularly observed and which also represent a crucial puzzle piece in the understanding of how dust grains can grow into planetesimals via gravoturbulent processes. In this thesis, I conduct high resolution studies of three-dimensional global models of turbulent protoplanetary disks using the magneto-hydrodynamics code PLUTO. I focus my studies on the Vertical Shear Instability (VSI), which has been shown to operate efficiently at disk radii beyond a few AU in typical protoplanetary disks. I show that vortices with radial diameters of around 1.5 local pressure scale heights and aspect ratios $\chi > 8$ form in VSI turbulent disks and that these vortices can survive more than 500 orbits. The vortices are forming irrespective of the underlying disk density gradient and aspect ratio and can therefore act as pressure traps for small to medium sized particles over a wide range of the disk. I also show evidence that these dusty vortices are compatible with detections of dust concentrations by current sub-mm interferometers. These findings therefore present a crucial puzzle piece which will help the understanding under which conditions and how early after the formation of a disk around a young star planetesimals can form via gravoturbulent planetesimal formation.

Zusammenfassung

Scheiben um junge Sterne sind die Geburtsstätten von Planetensystemen wie unser Sonnensystem. Daher ist das Studium turbulenter Prozesse in diesen Protoplanetaren Scheiben bedeutsam, und zwar nicht nur um den Drehimpulstransport zu verstehen und damit zum Beispiel das Drehimpulsdefizit unserer Sonne zu erklären, sondern auch um die Entstehung ausgedehnter Strukturen in diesen Scheiben zu verstehen, welche in jüngster Zeit regelmäßig in Beobachtungen gefunden werden und welche außerdem ein entscheidendes Puzzleteil in unserem Verständnis des Prozesses bilden, welcher mit Hilfe von gravoturbulenten Prozessen Planetesimale – Asteroiden und Kometen – aus Staubteilchen wachsen lässt. In dieser Dissertation präsentiere ich hochaufgelöste Simulationen von dreidimensionalen Modellen turbulenter protoplanetarer Scheiben unter Verwendung des magneto-hydrodynamik Simulationsprogramms PLUTO. Im Zentrum meiner Arbeit steht die Vertikale Scherinstabilität (VSI), welche in früheren Studien als effizient operierende Instabilität in typischen protoplanetaren Scheiben bei radialen Abständen von mehr als einer Astronomischen Einheit vom Zentralstern identifiziert wurde. Ich zeige, dass in Scheiben mit VSI generierter Turbulenz großflächige Wirbel mit einer radialen Ausdehnung von ca. 1.5 lokalen Druckskalenhöhen und einem Achsenlängenverhältnis $\chi > 8$ entstehen und dass diese Wirbel für mehr als 500 Umläufe um den Zentralstern bestehen bleiben. Die Wirbel formieren sich dabei unabhängig vom Dichtegradienten und Radius-zu-Druckskalenhöhenverhältnis der unterliegenden Scheibe und können daher als Hochdruckfallen für kleine und mittelgroße Staubteilchen über weite Teile der Scheibe dienen. Ich präsentiere außerdem Belege dafür, dass diese staubigen Wirbelstrukturen kompatibel sind mit aktuellen sub-mm Interferometer Beobachtungen von Staubansammlungen in protoplanetaren Scheiben. Diese Ergebnisse sind daher ein wichtiger Baustein in unserem Verständnis unter welchen Bedingungen und ab welcher Zeit nach der Entstehung des jungen Sterns und seiner Scheibe die Formation von Planetesimalen durch gravoturbulente Prozesse möglich ist.

For my mum
You always believed in me, even if I couldn't

CONTENTS

CHAPTER 1

INTRODUCTION

> Space: the final frontier.
>
> ---
>
> Star Trek, Roddenberry (1987-1994)

Have you ever looked at the night sky and thought: What else is out there? If the answer is yes, then you are in very good company. Astronomers (from the ancient greek astronomy meaning 'the law of the stars') have looked at the night sky for thousands of years, with historical documents going back to the times of ancient Greece and Mesopotamia.

Some of the questions driving astronomical advance in modern times, especially in the field of planet formation are: How did earth, and in extension our solar system, form? And is our solar system unique or are there other systems just like it out there around other stars? And if this is the case, how typical is our solar system compared to all the others? And although observational breakthroughs in the last few decades, from the first planet detected around a solar type star (Mayor & Queloz 1995), via the 4200 confirmed exoplanets from the Kepler space mission[1], to the high resolution observations of structures in protoplanetary disks with ALMA ALMA Partnership et al. (2015) and the recent discovery of a planet still forming in the disk around PDS 70 (Keppler et al. 2018), some of these questions still elude a definitive answer. But before I introduce the concept of how we think planetary systems are formed, lets take a look at the road astronomy took to get there.

A Historical perspective

One of the first attempts to explain the formation of our solar system, the nebula hypothesis, goes back to Immanuel Kant Kant (1755) and Pierre-Simon Laplace Laplace (1796). They theorised that the solar system formed out of a rotating nebula which flattens due to angular momentum conservation and eventually forms rings around the young star which contract seperately to form the planets. But in this model the sun has orders of magnitude less angular momentum than it should have (this problem is known as the solar angular momentum problem). Other models were proposed to solve this, e.g. explaining the solar system as the result of a proto-

---

[1] `http://exoplanet.eu/diagrams/`, accessed on 05.03.2019

stellar fly-by, which extracted material from the young sun (see Woolfson (1993) for an overview).

Parallel to the discussion of other models, the solar nebula theory was significantly advanced during the second half of the 20th century. Weizsäcker (1943) put Laplaces model on a modern theoretical footing and already postulated the formation of vortices in circumstellar disks. He also theorised that they are the places where planets form. Von Weizsäcker also argued that turbulent motions must be present in the disk and that the viscosity from this motions must drive disk evolution (Weizsäcker 1948). Later, the work of Safronov (1972) significantly advanced the theory of both disk and planet formation and contains the analytic footing of many current theories in the field.

The Modern perspective

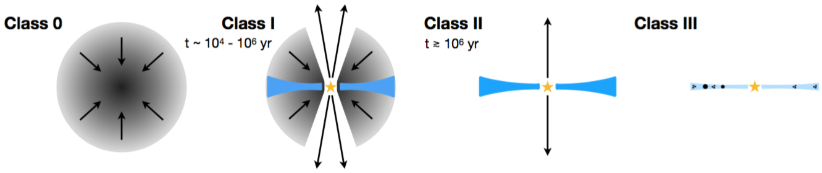

Figure 1.1: Observational classification of Young Stellar Objects according to the Lada sequence. Class 0 objects are protostars in their early collapsing phase while Class I objects have already formed a protostellar disk, though both are still embedded in a substantial envelope. Class II systems do not have an envelope but consist of a central protostar and a thin, gas-dominated disk. Class III systems are gas-poor and commonly known as debris disks. *Image from: Pohl (2018). The images are not to scale.*

In modern astronomy, planet formation is explained as a by-product of star formation, where planets are formed in disks of dust and gas around young stars. The formation of the stars themselves occurs in dense molecular clouds. Once a part of the cloud becomes massive (or cold) enough to exceed the Jeans mass it collapses, as the internal pressure cannot balance the gravitational pull. This initial collapse happens on a timescale of $\sim 10^5$ yr (essentially the free-fall time) and is halted once the gas in the inner parts becomes optically thick to its own radiation, forming the protostar (Class 0 object). Because the protostar is rotating and has to conserve angular momentum, it has to rotate faster. This halts the direct infall of the outer shells, which instead form a protostellar disk in the plane perpendicular to the angular momentum vector. Initially, the protostar and the disk will be surrounded by an envelope of infalling gas, which is accreted or dispersed through jets within another few $\sim 10^5$ years (Class I objects). Once the envelope is accreted, the essentially formed protostar is surrounded by a disk containing only a fraction of the stellar mass, a configuration called Class II object. During this stage, the protostar accretes mass from the protoplanetary disk while angular momentum is carried away by the disk, slowing down the protostellar rotation. During this phase, dust grains are believed to grow from micron sized objects to km-sized boulders, first through mutual sticking and later through concentration towards the midplane of the disk and in traps forming in the turbulent disk environment. Also, the formation of gas and ice giants happens during this stage. Once the accretion onto the central star ceases after roughly 10 Myr, the disk disperses rather quickly ($\lesssim 0.5 Myr$), leaving behind a gas poor disk dominated by n-body interactions of asteroids and already formed giant planets. These disks are termed Class III objects, also known as debris disks. In these disks, rocky planets then form through the mutual interaction and collision of asteroid sized objects and accretion of the remaining dust (see e.g. Raymond et al. 2014, and references therein).

Although this model gives us a basic outline as to how planetary systems form, many detailed questions are still waiting to be answered. For example, as stated above, during the gas-rich phase of disk evolution, the disk has to shed significant amounts of angular momentum. This is thought to occur, at least partially, through viscously driven accretion. But, to accomplish this in the time frame laid out above, the evolution cannot happen through molecular viscous forces alone. This problem has been mitigated with the discovery that the Magneto Rotational Instability (MRI, Balbus & Hawley 1991) can operate in protoplanetary disks, as the turbulence generated by the instability generates an effective viscosity (Shakura & Sunyaev 1973) orders of magnitude larger than molecular viscosity, strong enough to drive accretion on observed time scales. More recent work done on the MRI however shows that it is inactive near the midplane over a significant range of the disk (Gammie 1996; Dzyurkevich et al. 2013; Lesur et al. 2014). Therefore, hydrodynamic instabilities are considered as a source of turbulence (Lyra & Klahr 2011).

In recent years, many hydrodynamic instabilities have been (re-)discovered for protoplanetary disks. The most important class of instabilities for this thesis are entropy-driven instabilities. They arise because protoplanetary disks are baroclinic, which means that isobars (areas of constant pressure) and isopycnals (areas of constant density) are not aligned. Therefore, under the right conditions, the system can violate or circumvent the Solberg-Høiland criteria, which govern the hydrodynamic stability of the system. Examples of this are the Convective overstability (Klahr & Hubbard 2014) and the Vertical Shear Instability (Nelson et al. 2013), an instability known for stellar atmospheres as the Goldreich-Schubert-Fricke instability (Goldreich & Schubert 1967; Fricke 1968). These instabilities have been shown to support turbulence on a sufficient level to explain current observations (e.g. Lyra 2014; Stoll & Kley 2014).

Another question still not fully answered is how the growth of dust grains proceeds from sub-micron sized particles in the interstellar medium from which the disk around the newborn star is formed, to the >1000 km sized object known to us as earth. In the current model, small dust grains grow through sticking collisions, but this is only possible up to the size of a few millimeters to meters, depending on the surrounding disk conditions (see e.g. Testi et al. 2014, and references therein). To grow to sizes above this threshold, many models have been proposed, relying on mass transfer collisions or the 'fluffyness' of the grains. Another avenue pursued is to skip the growth through the regime of tens of meters sized objects entirely and form > km sized objects via gravitational collapse of a dust cloud (e.g. Johansen et al. 2006; Klahr & Schreiber 2016). This method relies however on the existence of conditions in the disk which are able to efficiently concentrate particles. Especially in the early protoplanetary disk, these structures have to form out of the turbulence itself. Promising candidates to work as these 'particle traps' are zonal flows (Dittrich et al. 2013) and vortices (Barge & Sommeria 1995), and the search especially for vortices formed from purely hydrodynamic turbulence is one of the primary topics of this thesis.

An Observational Perspective

For now, I only presented theoretical concepts of how we think the solar system formed out of a cloud of interstellar gas. But as the solar system is already several billion years old, we cannot test these theories from looking at our solar system alone. We have to turn to observations of other stars in our neighbourhood.

The first evidence of protoplanetary disks come from unresolved observations of stars performed in the second half of the 20th century. This was possible because the presence of the disk alters the Spectral Energy Distribution (SED) of the object. The SED is a measure of the Flux F_λ of a star as a function of wavelength and for a main sequence star, it is approximately equal to a black-body of stellar temperature. For a protostar however, the SED shows excess emissions in the infrared part of the spectrum due to the dust surrounding the star, as the dust reprocesses the starlight and emits it at wavelengths corresponding to the ambient dust temperature. This leads to emission in the near infrared from hot grains close to the central source, while colder dust far out in the disk will emit in the mid- or even far-infrared. This classification, proposed in Lada & Wilking (1984); Lada (1987) and Adams et al. (1987) and extended by Andre et al. (1993), is known as the Lada sequence and describes the SED according to its near- to mid-infrared slope, with Class 0 objects showing no excess (undefined slope), Class I showing a positive slope and Class II and III showing negative slopes, with slopes for Class III being distinctively steeper than for Class II.

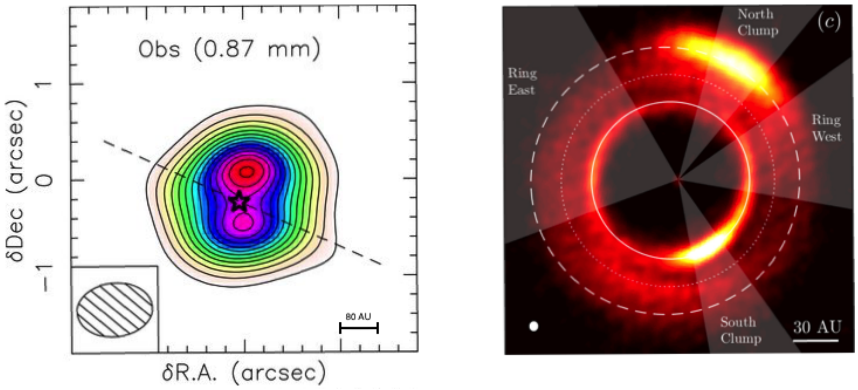

Figure 1.2: The disk MWC 758, imaged with the SMA in 2008 and with ALMA nearly ten years later. Although the SMA images already showed an asymmetric blob structure, the advances in resolution capability accomplished with ALMA allowed to identify and investigate the vortices in more detail and additionally reveal an inner ring and a gap not detectable with previous instruments. The hatched oval in the left image and the white oval in the right image represent the beam size of the respective observation.

With the development of high-angular resolution telescopes and interferometers, it has become possible to detect protoplanetary disks directly (fig. 1.2). With increasing resolution over the years, especially with the commissioning of the Atacama Large (sub-)Millimetre Array (ALMA), many more disks have been shown to have rings and gap structures as well as asymmetric, vortex-like features which were not as easily determined in previous observations and could not be inferred from simple SED measurements. Although the detection of the disks is also possible in optical and near-infrared observations, the cold dust traced by far infrared/sub-mm observations gives an unique insight into the inner parts of the disk, as it is, especially in the outer parts, mostly optically thin to radiation emitted at those wavelengths. This enables a detailed study of the environment in which planetesimals and planetary cores form, and for the firs time allows direct and detailed comparisons of theoretical models and simulations with observational data.

Outline of this Thesis

The goal of this thesis is to investigate the structure formation capabilities of hydrodynamic turbulence on the special case of the Vertical Shear Instability. To this end, I perform high resolution simulations of protoplanetary disks using the multi-purpose MDH code PLUTO, re-examining the numerical and physical conditions used in previous work. I will demonstrate that using a sufficiently realistic numerical setup, the VSI is capable to form large scale non-axisymmetric structures identified as vortices similar to the structures found in current observations of protoplanetary disks. The thesis is structured as follows:

Chapter 2 In this chapter, I introduce the basic concepts governing the evolution of protoplanetary disks in the gas and dust phase, with emphasis on the processes and equations necessary to understand the work done in this thesis. Additionally, I introduce the numerical codes used throughout this work.

Chapter 3 *Are partial simulations of 3 dimensional protoplanetary disks sufficient to investigate hydrodynamic instabilities? Or are they missing something?* This chapter presents a disk setup investigated in different numerical setups and discusses the influence the choice of disk extent has on the saturated state of the instability. It also presents the first hydrodynamical simulations of long lived vortices formed from the VSI in a global disk.

Chapter 4 *Is vortex formation always a consequence of a saturated Vertical Shear Instability?* Following on the results from chapter 3, this chapter presents a parameter study varying the disk density gradient and aspect ratio. It shows that vortices form in many different disk conditions, but always in a similar shape.

Chapter 5 *Can the structures found in our simulations be detected in observations? Or did we already do?* In this chapter, I use analytic modelling of dust trapping in vortices and radiative transfer calculations to show that the vortices found in our gas-only simulations can theoretically be observed with state-of-the-art sub-mm interferometers.

Chapter 6 This chapter presents a summary of the work presented in this thesis and conclusions drawn. It also addresses possible future research projects.

CHAPTER 2

A SHORT THEORY OF DISKS AROUND YOUNG STARS

Disks around forming stars are believed to be the cradles of planet formation and in this chapter, I will introduce the main equations and concepts necessary to understand the evolution of those disks. From observations of the interstellar medium (ISM), we assume that protoplanetary disks consist to about 99.8% out of Hydrogen and Helium, whereas the mass of all other elements, colloquially called 'metals', combined makes up the remaining 2% of the mass (Ansdell et al. 2016). Because the temperature of the material in the disk is lower than a few hundred Kelvin everywhere in the disk except in the innermost part, most of the metal elements will be in the form of solids rather than gaseous. Therefore it is necessary to define two different phases in the disk – the gas and the dust phase – where the gas phase is given by the Hydrogen-Helium mixture and the dust phase is comprised of the metals in the disk.

Because the gas and the dust phase are governed by similar but different equations of motion, I start with the equations for the gas phase of protoplanetary disks, before I introduce the equations governing the dust phase of the disk in section 2.2. Section then briefly summarizes the equations to calculate radiative transfer models while section introduces the numerical codes used in this thesis. In sections 2.1 and 2.2 I mainly follow the calculations of Armitage (2009), while section 2.3 is based on Rybicki & Lightman (1986), Dullemond (2013) and Pohl (2018).

2.1 Protoplanetary Disks: The Gas View

2.1.1 The Equations of Hydrodynamics

The gas phase of the protoplanetary disk has typical particle number densities of $n \approx 10^{14}\,\frac{1}{\mathrm{cm}^3}$, leading to a typical mean free path of the gas molecules in the disk on the order of 1 cm. This distance is orders of magnitude smaller than the typical length scale of the disk system, the pressure scale height $H \approx 5 \cdot 10^{11}\,\mathrm{cm}$. It is therefore possible to treat the gas of the disk as a continuous fluid. The dynamics of the gas can therefore be described using the *equations of mass* (2.1), *momentum* (2.2) and *energy* (2.3) *conservation*. The equations are presented in conservation form, as they will be employed in this form throughout this thesis. A derivation can be found in many fluid dynamics books (e.g. Clarke & Carswell 2007).

$$\frac{\partial}{\partial t}\rho + \nabla \cdot (\rho \mathbf{v}) = 0 \tag{2.1}$$

$$\frac{\partial}{\partial t}(\rho \mathbf{v}) + \nabla \cdot \left(\rho \mathbf{v}\mathbf{v}^T\right) = -\nabla P - \rho \nabla \Phi + S \tag{2.2}$$

$$\frac{\partial}{\partial t}E + \nabla \cdot ((E+P)\mathbf{v}) = -\rho \mathbf{v} \nabla \Phi + S^\star \tag{2.3}$$

Here, ρ represents the gas density, $\mathbf{v}$ its velocity and P the gas pressure. $E = \rho\frac{\mathbf{v}^2}{2} + \rho e$ is the total energy density of the gas with e representing the specific internal energy. Φ represents the external gravitational potential of the central star

$$\Phi = -\frac{GM_\star}{|\mathbf{r}|} \quad . \tag{2.4}$$

Including gravity in this way neglects the mass of the disk relative to the mass of the star, which is appropriate for protoplanetary disks with $M_{Disk} < 0.01 M_\star$. For massive disks with $M_{Disk} \gtrsim 0.01 M_\star$, the disks own gravity becomes important and and Poisson's equation for the gravitational potential has to be solved. For the remainder of this work, I will assume disks with low mass and neglect disk self-gravity.

As the gas in protoplanetary disks can be described as a subsonic Newtonian fluid, equation 2.2 can be rewritten into the Navier-Stokes-equations, where the terms S and $S^\star$ represent the viscous terms in the momentum and energy equation, although the terms can include other body or surface forces. Neglecting the additional source terms, the Euler equations are recovered.

The system is closed by prescribing an *Equation of State* (EoS). Throughout this thesis, the gas will be treated as an ideal gas, and the EoS will be written in either thermal or caloric form.

$$P = \frac{\rho}{\mu m_H} k_\mathrm{B} T \qquad \text{thermal EoS}$$

$$P = \rho e \sqrt{\gamma - 1} \qquad \text{caloric EoS}$$

For a gas with constant temperature, this reduces to the isothermal EoS $P = c_s^2 \rho$ with constant isothermal sound speed $c_s = \sqrt{\frac{k_\mathrm{B}}{\mu m_H} T}$.

2.1.2 Equilibrium Structure of Protoplanetary Disks

A first insight into the structure of protoplanetary disks is given by solving for the hydrostatic equilibrium of equations 2.2, in which one assumes constant velocities ($\partial/\partial t = 0$ and $\partial v_i / \partial x_j = 0$). Because protoplanetary disks can be described as approximately cylindrical, I will use cylindrical coordinates (R,ϕ,z) for the following derivations. Transforming equations 2.2 using equation 2.1 and assuming axisymmetry for the ϕ-axis ($\partial/\partial\phi = 0$) leads to:

$$\frac{v_\phi^2}{R} = \frac{GM_\star R}{|\mathbf{r}|^3} + \frac{1}{\rho}\frac{\mathrm{d}P}{\mathrm{d}R} \tag{2.5}$$

$$0 = \frac{GM_\star z}{|\mathbf{r}|^3} + \frac{1}{\rho}\frac{\mathrm{d}P}{\mathrm{d}z} \tag{2.6}$$

Because in protoplanetary disks the vertical extension is generally much smaller than the radial one ($R \gg z$), the gravitational force can be simplified using the thin-disk approximation: $|\mathbf{r}| = \sqrt{R^2 + z^2} \approx R$.

Assuming an isothermal equation of state, Equation 2.6 then transforms to:

$$\frac{1}{\rho}\frac{\mathrm{d}\rho}{\mathrm{d}z} = -\frac{\Omega_{\mathrm{K}}^2}{c_s^2} z \tag{2.7}$$

where I introduce the Keplerian angular frequency $\Omega_{\mathrm{K}}(R) = \sqrt{\frac{GM_\star}{R^3}}$. Solving the equation for ρ then leads to the vertical equilibrium structure of the disk:

$$\rho(R, z) = \rho(R) e^{-\frac{z^2}{2H^2}} \qquad , \tag{2.8}$$

where $H(R) = \frac{c_s(R)}{\Omega_{\mathrm{K}}(R)}$ is the vertical *pressure scale height* of the gas.

In this context, the vertical *column density* of the gas can be defined as

$$\Sigma = \int_{-\infty}^{\infty} \rho(\mathbf{r}) dz \tag{2.9}$$

and volume and column density are related via

$$\Sigma = \rho(R) \cdot \sqrt{2\pi} H \qquad . \tag{2.10}$$

To gain a first estimate on the column density in the early solar system, Weidenschilling (1977) spread the mass of the current solar system planets over a disk annulus defined by the distances between the planets and added enough Hydrogen and Helium to the mix to gain solar metallicity everywhere in the disk. This model is known as the *Minimum Mass Solar Nebula* (MMSN) and, neglecting Mercury, Mars and the asteroid belt, yields a radial power law distribution with an exponent of $-3/2$. With the normalization of Hayashi (1981), the column density is commonly written as

$$\Sigma = 1700 \left(\frac{R}{\mathrm{AU}}\right)^{-\frac{3}{2}} \frac{\mathrm{g}}{\mathrm{cm}^2} \qquad . \tag{2.11}$$

This estimate has however significant drawbacks, as it does neglect many disk evolution processes, e.g. planet migration. From observations, one finds a range of slopes generally shallower than the MMSN, for example, Andrews et al. (2009) find a mean slope of -0.9 for disks in the Ophiuchus star-forming region.

The azimuthal velocity structure of the disk can be obtained from the radial equilibrium equation 2.5.

$$v_\phi^2 = v_{\mathrm{K}}^2 + \frac{R}{\rho}\frac{\mathrm{d}P}{\mathrm{d}R} = v_{\mathrm{K}}^2 \left[1 - \eta\right] \tag{2.12}$$

Here $v_{\mathrm{K}}(R) = \Omega_{\mathrm{K}}(R) R$ is the keplerian azimuthal velocity and η the pressure support parameter of the disk, defined as

$$\eta = -\frac{R}{\rho v_{\mathrm{K}}^2}\frac{\mathrm{d}P}{\mathrm{d}R} \sim \frac{c_s^2}{v_{\mathrm{K}}^2} \tag{2.13}$$

with the geometric scale height $h(R) = \frac{H(R)}{R} = \frac{c_s}{v_\mathrm{K}} \ll 1$. This means that protoplanetary disks rotate not strictly at keplerian, but, as the radial pressure gradient is in general negative, at slightly sub-keplerian velocities. The deviation is small, but will become important later on when the dust phase is introduced. As the geometric scale height is related to the Mach number of the disk flow via $h = \mathrm{Ma}^{-1}$, this also implies that the azimuthal rotation velocity is highly *supersonic* throughout most of the disk.

2.1.3 Viscous and Turbulent Stresses

From the derivations above, we see that the disk, to first order rotates at keplerian velocity. Therefore the specific angular momentum of the disk gas is given as $l = R^2\Omega_\mathrm{K} = \sqrt{GM_\star R}$, which is an increasing function of radius. But to accrete mass, the gas has to lose angular momentum. One possibility for the gas to do so, is viscous dissipation. Lynden-Bell & Pringle (1974) derived the viscous evolution for a 1D radial disk model ($\Sigma = \Sigma(R,t)$, $v_R = v_R(R)$) using the vertically integrated equations of mass (cf. eq. 2.1)

$$\frac{\partial}{\partial t}(\Sigma) + \frac{1}{R}\frac{\partial}{\partial R}\left(R\Sigma v_R\right) = 0 \tag{2.14}$$

and angular momentum

$$\frac{\partial}{\partial t}(\Sigma R^2\Omega) + \frac{1}{R}\frac{\partial}{\partial R}\left(Rv_R\Sigma R^2\Omega\right) = \frac{1}{2\pi}\frac{\partial}{\partial R}T \qquad . \tag{2.15}$$

Here, $T = R \cdot 2\pi R \cdot \Sigma\nu R\frac{\partial\Omega}{\partial R}$ represents the viscous torque from outer layer shearing past inner layer. The right hand side in the equation above then describes the net viscous torque on the disk.

Combining equations 2.14 and 2.15 to eliminate v_r and substituting $\Omega = \Omega_\mathrm{K}$ then yields the equation describing the viscous evolution of a protoplanetary disk in radial direction.

$$\frac{\partial\Sigma}{\partial t} = \frac{3}{R}\frac{\partial}{\partial R}\left[R^{1/2}\frac{\partial}{\partial R}\nu\Sigma R^{1/2}\right] \tag{2.16}$$

For $\nu = \mathrm{const.}$ it can be shown, by using simple substitutions, that this is a diffusion equation with the diffusion time scale

$$t_\mathrm{diff} = \frac{4R^2}{3\nu} \qquad . \tag{2.17}$$

Using the molecular viscosity $\nu_\mathrm{mol} \sim \lambda c_s$ we can then estimate the time scale for molecular viscosity to disperse a protoplanetary disk. The typical mean free path λ is, as stated already at the beginning of the chapter, on the order of 1 cm at 1 AU. The typical sound speed of a disk with geometrical scale height $h = 0.05$ is $c_s = 1.5 \cdot 10^5 \frac{\mathrm{cm}}{\mathrm{s}}$ at 1 AU, giving a viscosity of $\nu_\mathrm{mol} \sim 1.5 \cdot 10^5 \frac{\mathrm{cm}^2}{\mathrm{s}}$. This yields a diffusion time scale of $t_\mathrm{diff,mol} \sim 10^{13}$ yr, which is orders of magnitude larger than the typical lifetime of protoplanetary disks obtained from observations, which is on the order of $10^6 - 10^7$ yr. Therefore, molecular diffusion cannot drive the evolution of protoplanetary disks.

The Alpha Disk Model

A model saving the explanation of the viscous disk evolution is the so-called α-model (Shakura & Sunyaev 1973). Here, the molecular viscosity ν_{mol} is replaced by the *turbulent viscosity* ν_{turb} described via a characteristic velocity u and length L. For (nearly) isotropic turbulence in a protoplanetary disk it is reasonable to assume that the turbulent eddies have a size smaller or comparable to the pressure scale height $L \lesssim H$ and that the turbulent velocities are smaller or comparable to the gas sound speed $u \lesssim c_s$. Note that the α-prescription, originally developed for disks around black holes, does not make any assumption on how the turbulence in the flow is created.

With these assumptions, the turbulent kinematic viscosity can then be expressed as

$$\nu_{\mathrm{turb}} = \alpha c_s H \tag{2.18}$$

where α is a free parameter. The only condition on alpha from our assumptions above is that it has to fulfil $0 < \alpha < 1$, as turbulence with $\alpha \geq 1$ would be supersonic and would lead to heating which would lead to $\alpha < 1$. It should be noted that α can and should be space and time dependent. Though using a strictly constant α allows for rigorous analytical derivations otherwise impossible, it should always be clear that this is a simplification and does not apply in most astrophysical applications.

To measure α in hydrodynamical simulations, the Reynolds averaged fluid equations (see e.g. Pedlosky (1992) for a derivation) can be used to find an effective viscous stress tensor describing the turbulent flow by splitting the velocity into a mean flow $\bar{v}$ and residual fluctuations v'. The $R\phi$ component of the Reynolds stress tensor, which facilitates the angular momentum transport in radial direction, can then be expressed as

$$T_{R\phi} = \langle \rho v'_R v'_\phi \rangle \tag{2.19}$$

where $\langle\,\rangle$ denotes an average over space and/or time. Combining this with equation 2.18 leads to

$$\langle \rho v'_R v'_\phi \rangle = \alpha \rho c_s^2 = \alpha P \qquad , \tag{2.20}$$

which is the form used to calculate α throughout this work.

To get an estimate how large α should be to explain the observations, we can use equation 2.17 in combination with equation 2.18. Assuming $t_{diff} = 5 \cdot 10^6$ yr at 10 AU then gives an α of about $5 \cdot 10^{-4}$, which, as will become apparent in the next section, is on the order of magnitude of what is expected from (magneto-) hydrodynamical turbulence models.

2.1.4 Instabilities in Protoplanetary Disks

Until now we have only assumed that some kind of turbulence is active in protoplanetary disks, because it is a likely explanation for the strong viscous accretion needed to explain the angular momentum transport. Although other means of angular momentum removal, e.g. magnetically driven winds, are discussed, the focus in this work lies with instabilities acting throughout the body of the disk.

The first instability of this kind proposed to act in protoplanetary disks is the *Magneto Rotational Instability* (MRI, Balbus & Hawley (1991)). The MRI, as the name suggests, requires a weak magnetic field threading the disk. Additionally, it

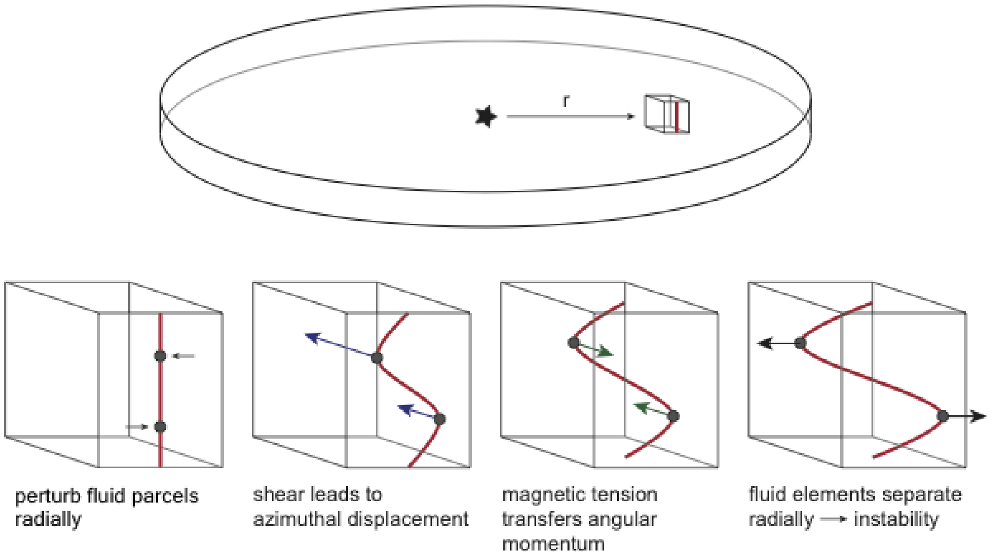

Figure 2.1: Schematic explanation of the MRI mechanism. The box represents a small volume within the disk, the black dots the fluid parcels and the red line a vertical magnetic field line. The arrows show the direction of the force on the fluid parcels due to the respective mechanism discussed. *Adapted from Armitage (2011)*

requires that the disk gas is ionized so it can couple to the magnetic field. Under these conditions, the instability works as follows: Two gas parcels coupled through a magnetic field line are slightly perturbed to orbiting on neighbouring annuli. To conserve angular momentum, the inner parcel then rotates with a slightly larger angular velocity, causing it to drift away from the outer parcel in azimuthal direction. The magnetic coupling tries to oppose this, creating magnetic tension that effectively removes angular momentum from the inner parcel and transferring it to the outer one. This, in turn, forces the inner parcel to drift further inward and the outer to drift outward to annuli matching their new amount of angular momentum. This leads the whole cycle to repeat itself, signifying an instability.

Although the MRI was long seen as the main driver for turbulence in protoplanetary disks due to its fast growth rate and strong turbulent viscosity ($\alpha \sim 10^{-2}$, e.g Davis et al. (2010)), its relevance to protoplanetary disk has been debated in recent years. Unlike in disks around black holes or neutron stars, protoplanetary disks are at best only weakly ionized. Therefore non-linear Magneto-Hydrodynamic effects have to be considered, namely Ohmic resistivity, ambipolar diffusion and the Hall effect. These all work to significantly damp the MRI outside of a few tens of AU and create a so called ”dead zone” where the MRI is not active (e.g. Gammie (1996); Dzyurkevich et al. (2010, 2013); Lesur et al. (2014), see Armitage (2019) for a recent review).

In this so called dead zone, hydrodynamically driven instabilities have to be considered (Lyra & Klahr 2011). A main group of instabilities considered here are instabilities thriving on the baroclinicity of the disk and the entropy gradient created as a result. Baroclinicity describes a fluid state where the pressure is not only a function of density, but also of other variables like temperature. Three different instabilities should be noted here: The convective overstability (Klahr & Hubbard

2014; Lyra 2014), the zombie vortex instability (Marcus et al. 2015, 2016; Barranco et al. 2018) and the vertical shear instability (Fricke 1968; Goldreich & Schubert 1967; Urpin 2003; Arlt & Urpin 2004; Nelson et al. 2013; Lin & Youdin 2015), and the latter of those three I will introduce in more detail later. For a comprehensive introduction into all three instabilities I refer the reader to recent reviews by Klahr et al. (2018) and Lyra & Umurhan (2018).

As a result of the perturbations generated by linear instabilities or overstabilities, other instabilities can grow. The subcritical baroclinic instability (Klahr & Bodenheimer 2003; Petersen et al. 2007a,b) has been shown to be a non-linear cousin of the convective overstability (Lyra 2014) and has been show to form and amplify vortices in protoplanetary disks Lyra & Klahr (2011); Raettig et al. (2013). Another Instability that forms as a secondary instability is the Rossby wave instability (Lovelace et al. 1999; Li et al. 2000, 2001), which occurs wherever a steep gradient in vorticity or entropy is present. The presence of vortices will become important once dust grains are introduced in section 2.2.

It should also be noted, that at early times, when the disk is still very massive ($M_{\rm Disk} \geq 0.1 M_\star$), the disks own gravity cannot be neglected. The disk self-gravity can then also lead to an instability of the disk (see e.g. Kratter & Lodato (2016) for an overview). Depending on the disk cooling and mass, the disk then either enters a quasi-stable state forming large spiral arms or it fragments into clumps. The spiral arm forming form has been shown to be able to transport angular momentum outwards, while the fragmenting form can explain the existence of wide orbit giant planets or brown dwarf companions. Throughout this work, self-gravity of the disk will be neglected, as the disks are assumed to have a low mass compared to the central object.

Stability Criteria of Rotating Fluids

Although much research has shown instabilities to act in protoplanetary disks, the fact that those disks become hydrodynamically unstable is non-trivial. To show this, I will in the following briefly introduce the criteria for stability against perturbations in rotating fluids.

The most fundamental stability criterion for rotating fluids is the *Rayleigh criterion*. It describes the stability of an inviscid rotating fluid between 2 cylinders (Taylor-Couette flow). A derivation can be found in many fluid dynamics textbooks, e.g. Drazin & Reid (2004). It states that for the flow to be stable, the angular momentum of the flow has to increase with radius, equal to

$$\frac{1}{R^3}\frac{\partial}{\partial R}(\Omega^2 R^4) > 0 \qquad . \tag{2.21}$$

As a protoplanetary disk can be approximated as a cylindrical flow with $\Omega = \Omega_{\rm K} \propto R^{-3/2}$, we directly see that the flow in a keplerian disk is unconditionally stable.

Strictly speaking, the Rayleigh criterion only applies to disks which do not have any stratification. As disk unfortunately have both radial and vertical stratification, the stability of the disk is governed by the more general *Solberg-Høiland criteria*

(Tassoul 1978):

$$\frac{1}{R^3}\frac{\partial j^2}{\partial R} - \frac{1}{C_P \rho}\nabla P \cdot \nabla S > 0 \tag{2.22}$$

$$\frac{\partial P}{\partial z}\left(\frac{\partial j^2}{\partial R}\frac{\partial S}{\partial z} - \frac{\partial j^2}{\partial z}\frac{\partial S}{\partial R}\right) < 0 \tag{2.23}$$

where $j = R^2\Omega$ denotes the specific angular momentum of the disk. Note that for a keplerian disk, for which generally $\frac{\partial P}{\partial z} < 0$, equation 2.23 reduces to the Schwarzschild criterion for stability against convection $\frac{\partial S}{\partial z} > 0$, which is more readily expressed as $|\nabla T_{\mathrm{ad}}| > |\nabla T|$ (i.e. the disk temperature gradient has to be *subadiabatic* for the disk to be stable).

Rüdiger et al. (2002) performed a linear stability analysis for the case of rotating accretion disks. Introducing the radial and vertical buoyancy frequency as

$$N_x^2 = -\frac{1}{\gamma\rho_0}\left(\frac{\partial P_0}{\partial x}\right)\frac{\partial}{\partial x}\log\left(\frac{P_0}{\rho_0^\gamma}\right) \qquad x \in R, z \tag{2.24}$$

and using a perturbation ansatz in cylindrical coordinates, they show that the Solberg-Høiland criteria can be expressed as

$$N_R^2 + N_z^2 + \kappa_R^2 > 0 \tag{2.25}$$

$$\frac{N_z^2}{N_R^2}\frac{H_z}{H_R}\kappa_R^2 - \kappa_z^2 > 0 \tag{2.26}$$

where $H_x = \frac{P}{\partial_x P}$ is the local pressure scale height with ∂_x expressing the derivative in $x \in R, z$ direction. The subscript 0 refers to the unperturbed base state and $\kappa_{R,z}$ is the epicyclic frequency in radial or vertical direction:

$$\kappa_x = \frac{1}{R^3}\frac{\partial j^2}{\partial x} \qquad x \in R, z\,. \tag{2.27}$$

Looking at equation 2.26, it is already clear that once the disk possesses vertical shear ($\kappa_z \neq 0$), the disk is mainly kept stable by vertical buoyancy forces. If these can be diminished somehow, the disk is vulnerable to instability.

The Vertical Shear Instability

The *Vertical shear Instability* (VSI) relies, as the name already suggests, on the existence of vertical shear in the disk. But as stated above, this alone is not sufficient to trigger the instability. Additionally, the vertical buoyancy has to be diminished, which is possible if the disk is either adiabatic or cools nearly isothermal. That these conditions lead to instability has been first discovered in the analysis of radiative zones of rotating stars by Goldreich & Schubert (1967) and independently by Fricke (1968), where the instability is known as the Goldreich-Schubert-Fricke instability. Urpin (2003) first suggested that the instability could also operate in protoplanetary disks.

Figure 2.2 shows a schematic view of the vertical shear of the protoplanetary disk necessary for the VSI to operate. Because the angular frequency Ω (blue solid

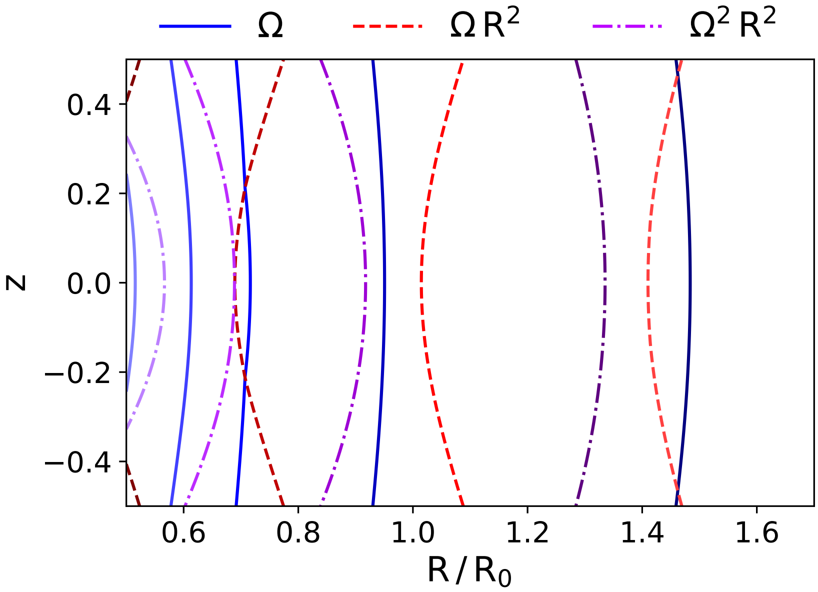

Figure 2.2: Schematic view of the shear in baroclinic disks. The blue solid lines show contours of constant angular frequency Ω, the red dashed lines contours of constant angular momentum ΩR^2 and the purple dashed-dotted lines represent contours of constant angular kinetic energy $\Omega^2 R^2$. Lighter colors represent larger values of the respective quantity, so while Ω and $\Omega^2 R^2$ decrease with increasing radius, ΩR^2 increases. This is known as radial shear. Additionally, the contours are not straight lines independent of z, but are bent inwards or outwards, which produces vertical shear in the disk. A gas parcel displaced along the lines of constant angular momentum changes now its radial and vertical position, enabling the onset of the vertical shear instability under certain conditions.

lines) depends not only on the radial but also on the vertical position in the disk, the surfaces of constant angular frequency are not cylinders but parabolas. The same then also applies to the surfaces of constant angular momentum ΩR^2 (red dashed lines) and angular kinetic energy $\Omega^2 R^2$ (purple dash-dotted lines). Additionally, while angular frequency $\Omega \sim R^{-3/2}$ and angular kinetic energy $\Omega^2 R^2 \sim R^{-1}$ decrease with radius, angular momentum $\Omega R^2 \sim R^{1/2}$ increases with radius. We can now think of the following scenario: A gas parcel is displaced upward along a surface of constant angular momentum, which also displaces it slightly outward. The gas parcel is now in a region where it has excess kinetic energy, so it can accelerate and move further upwards and outwards. In a stably stratified disk buoyancy will now counteract the upward motion. But in a disk which is cooled isothermal or at least where thermal diffusivity is large (so the cooling timescale is short compared to other timescales), the gas parcel (nearly) immediately thermalizes with the surrounding gas which diminishes the counteracting buoyancy. The disk then becomes unstable to small perturbations.

The instability in disks with cooling is not given by the Solberg-Høiland criteria, but by criteria derived by Arlt & Urpin (2004) for incompressible and more recently by Nelson et al. (2013) for compressible flow. They find the stability criterion for a locally isothermal disk to be:

$$\kappa_R - \frac{k_R}{k_z}\kappa_z > 0 \tag{2.28}$$

which immediately shows that the motions in VSI unstable disks are primarily vertical as the wavelengths in the vertical direction have to be much larger than the radial ones. Simulations indeed show that the VSI shows structures that are vertically elongated. Nelson et al. (2013) also show that the VSI grows in two distinct phases governed by two different types of modes, dubbed 'finger' and 'body' modes. The finger modes are radially narrow and occur in the upper layer of the disk descending to the midplane while the body modes are more radially extended and occupy the whole vertical extent of the disk. As the finger modes are the first to grow and appear more prominent, the VSI turbulence first appears as growing symmetric (with respect to the midplane) in the upper layers descending towards the midplane, while it later shows an anti-symmetric pattern.

Nelson et al. (2013) also calculated the growth rate of the instability for a locally isothermal, compressible gas in the shearing-sheet approximation as:

$$\Gamma^2 = \frac{-\kappa_{R,0}^2(c_0^2k_z^2 + N_{z,0}^2) + 2\Omega_0 c_0^2 k_R k_z \partial_z V_\phi}{c_0^2(k_z^2 + k_R^2) + \kappa_{R,0}^2 + N_{z,0}^2} \tag{2.29}$$

where the subscript 0 denotes the values at the base state and V_ϕ is the azimuthal velocity. In the case of $N_z \to 0$, small geometric scale height h_0 and $\frac{k_z}{k_R} \sim \mathcal{O}\left(q\frac{H_0}{R_0}\right)$ the growth rate can to first order be expressed as

$$\Gamma \sim |q|\frac{H}{R}\Omega \qquad . \tag{2.30}$$

Therefore the growth rate depends to first order on the slope temperature gradient q as well as the the geometric scale height of the disk. This behaviour has been confirmed in two dimensional axisymmetric simulations (Nelson et al. 2013). They also showed the VSI to be able to generate turbulent angular momentum transport on the order of $\alpha \sim 10^{-3}$. Further simulations showed α to be generally on the order of $10^{-5} - 10^{-3}$ depending on the chosen parameters, with shorter cooling times and higher disk aspect ratio giving stronger transport as expected (Stoll & Kley 2014; Richard et al. 2016; Flock et al. 2017b). Stoll & Kley (2016) and Flock et al. (2017b) performed simulations of the VSI using radiation hydrodynamical simulations and confirmed the existence of the instability in more realistic models, while finding α to be slightly lower than in locally isothermal calculations. Stoll et al. (2017) showed that the turbulence created by the VSI is not isotropic, but rather that the stresses in vertical-azimuthal direction are much stronger than in the radial-azimuthal direction (which determine angular momentum transport).

Above I already stated that the VSI works preferentially in disks where the cooling time is short because longer cooling times mean that buoyancy can stabilize otherwise unstable modes. Lin & Youdin (2015) calculated the longest critical cooling time for which the VSI can operate as

$$t_{\mathrm{crit}} \leq \frac{|\partial_z v_\phi|}{N_z^2} \approx \frac{h|q|}{\gamma - 1}\Omega_{\mathrm{K}}^{-1} \tag{2.31}$$

where the approximation on the right holds for global models. For typical disk parameters this critical cooling time is on the order of 0.1 orbits. In disks cooling on longer timescales the growth of the VSI will be suppressed. Because of this dependence on short cooling times the VSI mainly operates in the outer disk beyond 5 - 10 AU and generally favours more massive disks and host stars (Pfeil & Klahr 2019).

2.1.5 Vortices in Protoplanetary Disks

Vortices are an inherent property of turbulent flow. They appear on all scales in our everyday life, from the small vortex found when emptying the sink, over dust devils, tornado's and wingtip vortices on airplanes to hurricanes and cyclones. In astronomy, examples of vortices include the hexagon at Saturn's pole, Jupiter's great red spot and vortices found in observations of protoplanetary disks.

In general, vortices can be divided in two categories: *cyclonic* and *anti-cyclonic vortices*. Cyclonic vortices, usually referred to as cyclones in meteorology, have a pressure minimum in there center, whereas anti-cyclonic vortices have a pressure maximum at the center. Additionally, vortices can be sorted into categories determining which forces are important when looking at a steady state solution. For tornado's for example, the pressure force is balanced by the centrifugal force, whereas for Jupiter's Great Red Spot it is the Coriolis force which balances the pressure force. An important dimensionless number in this context is the Rossby number, which compares the Coriolis force to the inertial forces in the Navier-Stokes-Equations:

$$\mathrm{Ro} = \frac{V}{L\Omega} \tag{2.32}$$

where V represents a characteristic velocity of the flow, L a characteristic length of the system and Ω the rotation frequency of the rotating system. For tornado's typical values of the Rossby number are $\mathrm{Ro} \gtrsim 1000$, meaning the Coriolis force is negligible, whereas for Jupiter's Great Red Spot $\mathrm{Ro} \approx 0.07$ (Hess 1969), making the Coriolis force dominant. Hurricanes usually have $\mathrm{Ro} \approx 1$, especially close to the center, and therefore neither Coriolis nor centrifugal forces can be neglected. In protoplanetary disks, large scale vortices typically have $\mathrm{Ro} < 1$ and are therefore considered to be dominated by a balance of pressure and Coriolis forces, a state termed geostrophic balance. Because of geostrophic balance, cyclonic vortices rotate prograde (with the disk rotation), whereas anti-cyclonic vortices rotate retrograde (opposite to the disk rotation) in the frame co-moving with the vortex. In the inertial frame anti-cyclonic vortices can nevertheless be rotating prograde if their rotation is slow compared to the disk rotation.

Contrary to earths atmosphere, where both cyclonic and anti-cyclonic large scale flows are observed, protoplanetary disks only permit anti-cyclonic vortices as stable solutions. Adams & Watkins (1995) showed that prograde rotation with respect to the disk rotation leads to the vortices being sheared away (see figure 2.4), because the vortex rotation leads to velocities opposite to the disks shear flow. This leads to the fast destruction of cyclonic vortices. Contrary to this, anti-cyclonic vortices, which rotate retrograde, have velocities similar to the background shear flow of the disk, and the vortices are stable for hundreds of orbits. This behaviour has been

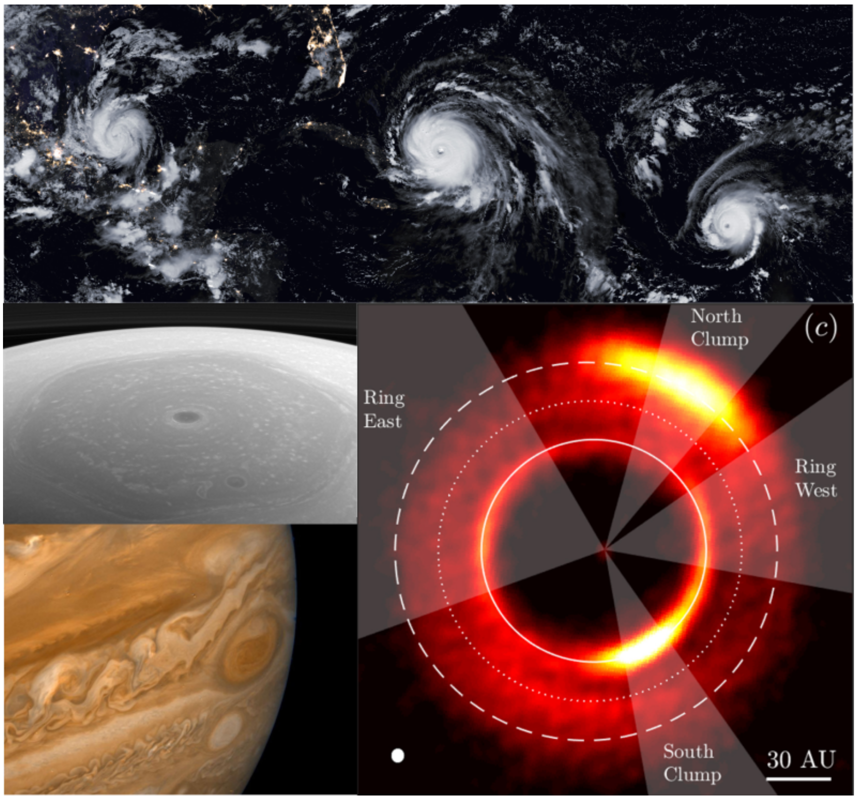

Figure 2.3: Examples of vortices in atmospheric and accretion disk flow. The top images shows hurricanes Katja, Irma and Jose approaching the Gulf of Mexico in September 2017 (Image credit: NASA Earth Observatory images by Joshua Stevens and Jesse Allen). The image in the middle left shows a near-infrared image taken by the Cassini probe of the polar hexagon, a large scale stable vortex system at Saturn's north pole (Image credit: NASA/JPL-Caltech/Space Science Institute) and the image below depicts an optical images of the Great Red Spot on Jupiter, taken with the narrow-angle camera of Voyager 2 (Image credit: NASA/JPL). The image on the right is a sub-mm image of the disk MWC-758 and shows the particle concentration in asymmetric features typically identified as vortices (Dong et al. 2018).

well documented in simulations (e.g. Godon & Livio 1999; Li et al. 2001; Barranco & Marcus 2005; Meheut et al. 2010; Raettig et al. 2013).

The Vorticity Equation

A key quantity when working with vortices is the vorticity of the flow, which is defined as the local rotation of the velocity field:

$$\omega = \nabla \times \mathbf{v} \qquad . \tag{2.33}$$

To gain some insight into the behaviour of vorticity, one can look at the evolution equation of vorticity. The following derivations follow Thompson (2006).

Taking the curl of equation 2.2 and neglecting source terms for now we obtain

$$\nabla \times \left[\frac{\partial}{\partial t} (\mathbf{v}) + (\mathbf{v} \cdot \nabla) \mathbf{v} \right] = \nabla \times \left[-\frac{1}{\rho} \nabla P \right] \qquad . \tag{2.34}$$

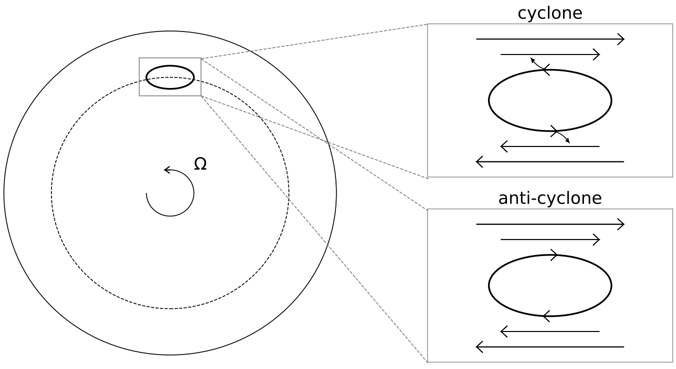

Figure 2.4: Schematic explanation why cyclonic and anti-cyclonic vortices behave differently in protoplanetary disks. The upper right panel shows a cyclonic vortex in its co-moving frame of reference. The vortex rotation is shown by the arrows on the vortex ellipse and is in the same sense as the disk rotation shown on the left (prograde). The shear flow of the background disk is given by the arrows above and below the vortex. The vortex rotation leads to opposite relative velocities of the vortex flow and the disk background, destroying the vortex. The lower right panel shows the case of the anti-cyclonic vortex, which rotates in the opposite direction as the disk (retrograde). The velocities of the vortex in the rotating frame are now parallel to the background shear flow, allowing the vortex to stay stable. *Adapted from Adams & Watkins (1995).*

In this step, all source terms representing conservative force fields would drop out as the curl of the gradient of a scalar field is zero. Non-conservative forces and source terms such as viscosity however will not generally vanish. Using the vector identity $(\mathbf{v}\cdot\nabla)\,\mathbf{v} = (\nabla\times\mathbf{v})\times\mathbf{v} + \nabla\left(\frac{1}{2}\mathbf{v}^2\right)$ and equation 2.33 leads to

$$\frac{\partial}{\partial t}\omega + \nabla\times[\omega\times\mathbf{v}] = \nabla\times\left[-\frac{1}{\rho}\nabla P\right] \tag{2.35}$$

which we can further simplify by using the identity $\nabla\times[\omega\times\mathbf{v}] = (\mathbf{v}\cdot\nabla)\,\omega - (\omega\cdot\nabla)\,\mathbf{v} + \omega\,(\nabla\cdot\mathbf{v}) - \mathbf{v}\,(\nabla\cdot\omega)$ and noting that the last term of this identity vanishes due to equation 2.33:

$$\frac{\partial}{\partial t}\omega + (\mathbf{v}\cdot\nabla)\,\omega = (\omega\cdot\nabla)\,\mathbf{v} - \omega\,(\nabla\cdot\mathbf{v}) + \frac{1}{\rho^2}\,(\nabla\rho\times\nabla P) \qquad . \tag{2.36}$$

This equation is known as the vorticity equation and we can already learn a few things from it. For fluids which are barotropic, meaning the pressure $P = P(\rho)$ is only a function of density, the last term vanishes. If the flow is now assumed to be incompressible and confined to the x-y plane (2 dimensional flow) the right hand side vanishes completely and the vorticity of the flow is conserved along the flow:

$$\frac{\mathrm{D}}{\mathrm{D}t}\omega = 0 \tag{2.37}$$

where $\frac{\mathrm{D}}{\mathrm{D}t} = \frac{\partial}{\partial t} + (\mathbf{v}\cdot\nabla)$ is the definition of the material derivative. Returning back to 3 dimensional flow and relaxing the assumption of incompressibility, equation

2.36 can be rewritten using equation 2.1 to

$$\frac{\partial}{\partial t}\left(\frac{\omega}{\rho}\right) + (\mathbf{v}\cdot\nabla)\left(\frac{\omega}{\rho}\right) = \left(\frac{\omega}{\rho}\cdot\nabla\right)\mathbf{v} - \left(\frac{\omega}{\rho}\right)(\nabla\cdot\mathbf{v}) + \frac{1}{\rho^3}\left(\nabla\rho\times\nabla P\right) \tag{2.38}$$

where the quantity $\frac{\omega}{\rho}$ is known as one form of the the *potential vorticity* (also known as vortensity) and it is materially conserved for barotropic flow. Therefore, vortex lines (lines parallel to the vorticity vector) move with the flow. Using Kelvins circulation theorem, it can additionally be shown that if a vortex tube (defined as a bundle of non-crossing vortex lines) is stretched or compressed, it has to increase or decrease its vorticity to conserve its circulation.

For baroclinic flows, for which areas of constant pressure (isobars) are not aligned with areas of constant density (isopycnals), the potential vorticity defined above will generally not be materially conserved. It can however be shown, that the potential vorticity $\omega_p = \frac{\omega}{\rho}\cdot\nabla\psi$ is materially conserved if ϕ is conserved:

$$\frac{\mathrm{D}}{\mathrm{D}t}\omega_p = \frac{\mathrm{D}}{\mathrm{D}t}\left(\frac{\omega}{\rho}\cdot\nabla\psi\right) = \frac{1}{\rho^3}\left(\nabla\rho\times\nabla P\right)\cdot\nabla\psi + \left(\frac{\omega}{\rho}\cdot\nabla\right)\frac{\mathrm{D}}{\mathrm{D}t}\psi = 0 \tag{2.39}$$

where the last equality holds as long as $\frac{\mathrm{D}\psi}{\mathrm{D}t} = 0$. This also implies that if the planes of constant ψ move further apart (closer together), the vortex has to increase (decrease) its vorticity. A quantity typically chosen for ψ in atmospheric sciences is the potential temperature of the atmosphere.

A final observation can be made by changing to a rotating coordinate system. In the co-rotating frame, the *relative vorticity* can be defined as

$$\omega = \omega_{\mathrm{rel}} + \omega_{\mathrm{frame}} \tag{2.40}$$

where the vorticity due to the rotation of the frame is given by the vorticity $\omega_{\mathrm{frame}} = 2\Omega$ of a rigid rotator. It can be immediately seen that, as only the absolute vorticity (or potential vorticity) is conserved, once the rotation rate of the co-rotating frame changes (e.g. because the vortex migrates), the relative vorticity of the vortex has to change. If we now that the Rossby number is small ($|\omega_{\mathrm{rel}}| \ll |\Omega|$) and that temporal changes in the vorticity can be ignored, equation 2.36 becomes

$$2\boldsymbol{\Omega}\left(\nabla\cdot\mathbf{v}\right) - 2\left(\boldsymbol{\Omega}\cdot\nabla\right)\mathbf{v} = \frac{1}{\rho^2}\left(\nabla\rho\times\nabla P\right) \qquad . \tag{2.41}$$

If the fluid is then additionally barotropic and incompressible

$$2\left(\boldsymbol{\Omega}\cdot\nabla\right)\mathbf{v} = 0 \qquad , \tag{2.42}$$

implying that there is no flow permitted in the direction of the rotation axis of the underlying flow. This is the *Taylor-Proudmann theorem.*

Vortex Solutions in 2 and 3 Dimensions

Because vorticity is conserved in two dimensional barotropic, inviscid, incompressible fluids, many steady state vortex solutions have been proposed. One is the Goodman-Narayan-Goldreich (GNG) solution Goodman et al. (1987), which I will briefly introduce here.

The velocity field of the vortex in the GNG solution is described as

$$v_x = \eta \Omega_\mathrm{K} y / \chi \qquad\qquad v_y = -\eta \Omega_\mathrm{K} x \chi \tag{2.43}$$

where the ratio η of the angular velocity Ω of the vortex to the keplerian angular velocity is given by

$$\eta = \sqrt{\frac{3}{\chi^2 - 1}} \tag{2.44}$$

with the aspect ratio χ being the ratio of the semi-major to the semi-minor axis. Vortices following the GNG solution have streamlines describing perfect ellipses. Because the derivation naturally has $v_z = 0$, the solution even holds in three dimensions as the vortex solution has perfect vertical equilibrium, although in this case vorticity is no longer conserved. The solution however has some drawbacks. The derivation does not take the background flow into account leading to a discontinuity in the velocities at the vortex boundary. Also, the derivation assumes constant background density, ignoring radial stratification which is typically assumed in protoplanetary disks.

Surville & Barge (2015) developed a more general model of vortices in vertically integrated disks, which takes into account the background stratification of the disk. Their model also predicts 2 different classes of vortices, compressible vortices which are small ($\chi < 7$) but have a high absolute Rossby number and incompressible vortices which tend to be large but have smaller absolute Ro. The compressible vortices also exhibit stronger spiral waves than the incompressible ones. They also show that the GNG model presented above is an acceptable model for the incompressible vortex family.

As said above, vortex models are often developed neglecting the vertical component of the flow and it is not immediately clear that the 2D models are applicable. A first assumption is that three dimensional vortices can be described by vertically 'stacked' two dimensional ones into an infinite column. Barranco & Marcus (2005) showed that this assumption is only partially correct. They find that 3D vortices can indeed be described as columns, but only up to a few disk scale heights, above which the vortex is truncated by shear flows. Because vorticity is divergence free, streamlines have to be closed which leads to additional vertical motion in vertical direction.

Contrary to two dimensional models, 3D vortices are not in general stable. Barranco & Marcus (2005) already described the occurrence of an instability that destroyed the initial vortices in their simulations after a few hundred orbits. Lesur & Papaloizou (2009) propose the operation of a linear parametric instability which can destroy vortices, termed the *elliptic instability* (EI). The instability destabilizes elliptic streamlines by creating a positive resonance if the vortex turnover time matches a frequency of the underlying flow field. In vertically unstratified protoplanetary disks, the instability occurs for vortices with aspect ratios $1 < \chi < 4$ and $\chi > 6$, whereas vortices with aspect ratios in between are not affected by the EI. This is different for vertically stratified disks, in which vortices of all aspect ratios are vulnerable to the EI. The growth rate depends however on the strength of the stratification for $\chi > 4$, making large elongated vortices less likely to be disrupted. Contrary to this, vortices with small aspect ratio are always highly unstable independent of stratification.

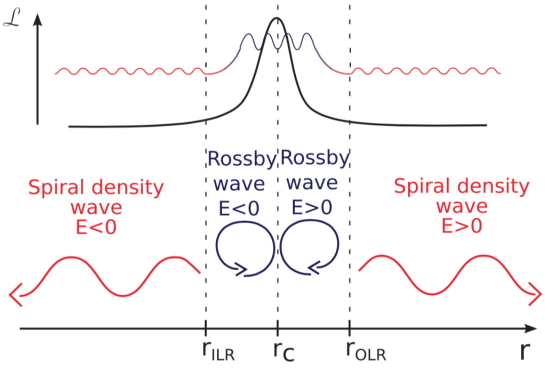

Figure 2.5: Schematic view of the Rossby Wave Instability mechanism. Rossby waves are triggered in regions with a strong gradient in $\mathscr{L}$ and trapped between the two Lindblad resonances $r_{\rm ILR}$ and $r_{\rm ORL}$ ($r_{\rm C}$ denotes the co-rotation radius). The rotational shear couples the Rossby Waves to density waves which can propagate away from the Lindblad resonances. *Image from Meheut et al. (2013).*

Vortex Formation in Protoplanetary Disks

In protoplanetary disk theory, there are currently two mechanisms discussed which can form vortices. One is the *Rossby Wave Instability* (RWI) first derived by Lovelace et al. (1999) and expanded upon in (Li et al. 2000, 2001), although similarities to the Papaloizou-Pringle (Papaloizou & Pringle 1984, 1985) instability exist. It operates in regions with an extremum in $\mathscr{L}$, defined as

$$\mathscr{L} = \frac{\Sigma}{2\omega_z}\left(\frac{P}{\Sigma^\gamma}\right)^{2/\gamma} \quad . \tag{2.45}$$

Inside this region, two Rossby waves are triggered, one with positive and one with negative energy. These waves interact and increase their amplitude, growing the instability. The rotational shear couples the Rossby waves to density waves, which propagating outside the Lindblad resonances, carrying away energy and decreasing the amplitude of the Rossby waves (Meheut et al. 2013). Once the amplitude of the Rossby waves has grown sufficiently, around 5 vortices appear, which immediately start to interact and typically merge within a few hundred orbits. On should note that the RWI is a global instability with maximum growth occurring for azimuthal wave numbers $m \approx 5$ (Li et al. 2000), so it cannot be observed in shearing-box or 2D axisymmetric simulations.

Whereas Lovelace et al. (1999) considered the RWI only in 2D vertically integrated disks, Meheut et al. (2010),Lin (2012a) and Richard et al. (2013) showed that the instability operates in a similar way in 3 dimensional disks. The vortices form columnar structures in the disk which resemble 2D vortices stacked in z-direction as described above, although only Meheut et al. (2010) and Lin (2012a) reported an additional vertical flow through the vortex in certain disk conditions. The growth of the instability is altered in massive disks in which self-gravity is non-negligible (Lyra et al. 2009; Lin 2012b), leading to the vortices being prohibited from merging and suppression of the instability for the most massive configurations.

Because $\mathscr{L}$ depends both on ω_z and Σ, the instability can be triggered in regions with bump in vertical vorticity as well as in density. The latter has been shown to enact the RWI at the edges of gaps carved by planets (e.g. Lin 2012b; Fu et al. 2014; Lobo Gomes et al. 2015; McNally et al. 2019; Baruteau et al. 2019) in low viscosity disks, which has become the most popular explanation for vortices found in observations (e.g. van der Marel et al. 2013, 2016; Dong et al. 2018; Baruteau et al. 2019). A density bump can also form at the inner edge of the dead-zone in non-ideal MHD disk simulations, where the turbulence strength changes abruptly (e.g. Varnière & Tagger 2006; Dzyurkevich et al. 2010; Lyra & Mac Low 2012; Flock et al. 2017a). The vortices at both the gap and the dead-zone edge can exist for hundreds of orbits, as the disk continually restores the density maximum the instability feeds off from. Flock et al. (2015) showed that vortices can occur at least intermittently also at the outer edge of the dead-zone, though the underlying mechanism is yet to be determined. In chapter 3 I will show that the RWI can also act as a secondary instability feeding on a maximum in vorticity created by the underlying hydrodynamic instability.

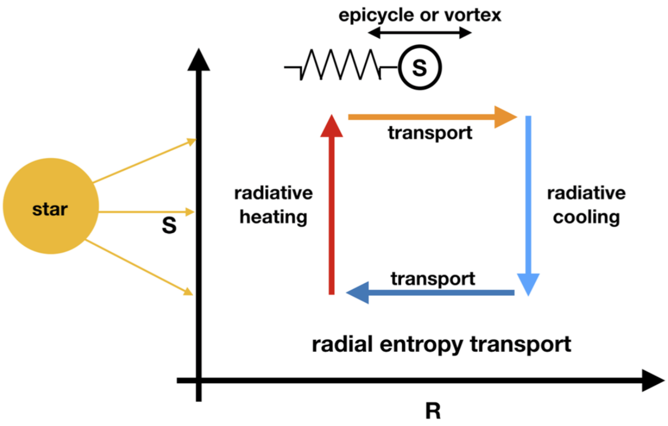

Figure 2.6: Schematic view of the SBI mechanism. A gas parcel displaced radially outward along a vortex streamline comes in contact with colder gas and experiences buoyant forces pushing it further out. Radiative cooling slowly thermalises the parcel while it moves half the way around the vortex. Arriving at the original radial position it is cooler and denser and is pulled towards the star by gravity. Moving along the second half of the vortex the gas parcel is slowly heated, arriving at the starting position hotter than the surrounding gas. The cycle then repeats, amplifying the vortex. *From Klahr et al. (2018).*

Another mechanism that forms vortices in protoplanetary disks is the *Subcritical Baroclinic Instability* (SBI) (Klahr & Bodenheimer 2003; Petersen et al. 2007a,b; Lesur & Papaloizou 2010), which Lyra (2014) identified as the non-linear saturated phase of the convective overstability. The instability mechanism forms and amplifies vortices as follows (Klahr et al. 2018, see also figure 2.5): A gas parcel moving around the vortex is moved radially outward, bringing it into contact with colder gas, creating buoyancy forces on the parcel pushing it further outwards. During the movement along the outer half of the vortex, the parcel thermalises with the environment, and once it is back at the original radius it is now cooler than in the beginning. The gas parcel next moves radially inward as it continues to move along the vortex streamline. The parcel is now brought in contact with hotter gas and the colder, denser parcel is pulled closer to the star by gravity. It then thermalises again with the disk gas and once it is at its original starting position, it is hotter than when it began the journey. The cycle then starts anew, creating a steady amplification of the vortex.

2.2 Protoplanetary Disks: The Dust View

2.2.1 The Coupled Dust-Gas Equations

Although the dust mass in protoplanetary disks is only 2% of the total disk mass, it is the the dust particles that form the asteroids and planets (or planetary cores in the case of gas giants) observed in our solar system and around other stars. However, in the ISM, dust grains have sizes on the order of microns, which makes planet formation a process spanning 13 orders of magnitude in size. Fortunately, for particles smaller than a few millimetres to centimetres (depending on distance to the star) the dust phase can be treated as a fluid, similar to the gas. The equations governing both the dust and the gas can then be written as a coupled system of equations

$$\frac{\partial}{\partial t}\rho_{\mathrm{g}} + \nabla \cdot (\rho \mathbf{v}_{\mathrm{g}}) = 0 \tag{2.46}$$

$$\frac{\partial}{\partial t}\rho_{\mathrm{d}} + \nabla \cdot (\rho \mathbf{v}_{\mathrm{d}}) = 0 \tag{2.47}$$

$$\frac{\partial}{\partial t}(\rho_{\mathrm{g}}\mathbf{v}_{\mathrm{g}}) + \nabla \cdot \left(\rho_{\mathrm{g}}\mathbf{v}_{\mathrm{g}}\mathbf{v}_{\mathrm{g}}^{T}\right) = -\nabla P_{\mathrm{g}} - \rho_{\mathrm{g}}\nabla\Phi + \frac{1}{t_{\mathrm{s}}}(\mathbf{v}_{\mathrm{d}} - \mathbf{v}_{\mathrm{g}}) \tag{2.48}$$

$$\frac{\partial}{\partial t}(\rho_{\mathrm{d}}\mathbf{v}_{\mathrm{d}}) + \nabla \cdot \left(\rho_{\mathrm{d}}\mathbf{v}_{\mathrm{d}}\mathbf{v}_{\mathrm{d}}^{T}\right) = -\rho_{\mathrm{d}}\nabla\Phi - \frac{1}{t_{\mathrm{s}}}(\mathbf{v}_{\mathrm{d}} - \mathbf{v}_{\mathrm{g}}) \tag{2.49}$$

where the subscript g denotes the gas and the subscript d the dust. The main difference between the dust 2.49 and gas 2.48 momentum equations is the absence of pressure in the dust phase. Additionally, the friction between both phases is introduced as an equal and opposite source term in both equations. The coefficient t_{s} is the timescale on which friction acts to equilibrate dust and gas velocities.

2.2.2 Dust Drag Forces

Although individual dust grains come in a myriad of shapes and sizes, their interaction with the surrounding gas can be described rather easily. This is because the interaction of particles with the surrounding gas can be described by friction. In this description, the shape of the particle, however complicated it may be, can be neglected and we can just assume every particle to be a sphere of some size a and particle density ρ_p. The force on the particle due to friction is then given as

$$F_{\mathrm{D}} = -\frac{1}{2}C_{\mathrm{D}}\pi a_{\bullet}^{2}\rho(\Delta\mathbf{v})^{2} \tag{2.50}$$

where $\Delta v = \mathbf{v}_\mathrm{d} - \mathbf{v}_\mathrm{g}$ is the differential velocity between dust and gas and C_D is a coefficient dependent on the drag regime the particle has to be treated in:

$$C_\mathrm{D} = \begin{cases} \dfrac{8 v_\mathrm{th}}{3\Delta v} & a_\bullet \leq \dfrac{9}{4}\lambda \\ 24\,\mathrm{Re}^{-1} & a_\bullet > \dfrac{9}{4}\lambda \end{cases} \tag{2.51}$$

where $v_\mathrm{th} = \left(\frac{8}{\pi}\right)^{1/2} c_s \approx c_s$ is the thermal speed of the gas and $\mathrm{Re} = \frac{2a_\bullet \Delta v}{\nu}$ is the Reynolds number of the dust. The first case is the *Epstein drag* regime, which applies for particles with sizes smaller than roughly the mean free path λ of the gas. Particles larger than the mean free path but with Reynolds numbers $\mathrm{Re} < 1$ are in the *Stokes drag* regime. Recollecting from the beginning of this chapter that the mean free path of the gas in the disk is on the order of 1 cm, we immediately see that most of the particles we are concerned with are in the Epstein regime, so the particles will be assumed to follow the Epstein drag law throughout this thesis.

The time on which the friction force becomes important to the hydrodynamical system is the friction time

$$t_\mathrm{s} = \frac{m_\bullet \Delta v}{|F_\mathrm{D}|} \tag{2.52}$$

also known as the stopping time, as it is equal to the time the gas needs to adjust the velocity of small grains to the gas velocity. In the Epstein and Stokes regime, the friction time takes the form

$$t_\mathrm{s} = \begin{cases} \dfrac{\rho_\bullet a_\bullet}{\rho v_\mathrm{th}} & a_\bullet \leq \dfrac{9}{4}\lambda \\ \dfrac{2\rho_\bullet a_\bullet^2}{9\rho\nu} & a_\bullet > \dfrac{9}{4}\lambda \end{cases} \tag{2.53}$$

Comparing the friction time to the timescale t_ed of the largest eddy then defines the Stokes number of the particles:

$$\mathrm{St} = \frac{t_\mathrm{s}}{t_\mathrm{ed}} = t_\mathrm{s}\Omega \tag{2.54}$$

where it is assumed that for protoplanetary disks $t_\mathrm{ed} = 1/\Omega$. As the Stokes number is dimensionless, it is also called the dimensionless stopping time of the particle τ_s. Both names will be used interchangeably throughout this thesis.

2.2.3 Equilibrium State

Nakagawa et al. (1986) derived the steady-state solution for equations 2.46-2.49 for particles with $\mathrm{St} \lesssim 1$. Following the notation of Youdin & Johansen (2007), the radial and vertical velocities of the gas and dust are given as:

$$v_{R,\mathrm{g}} = \frac{2\epsilon\tau_\mathrm{s}}{(1+\epsilon)^2+\tau_\mathrm{s}^2}\eta v_\mathrm{K} \tag{2.55}$$

$$v_{\phi,\mathrm{g}} = v_\mathrm{K} - \left[1 + \frac{\epsilon\tau_\mathrm{s}^2}{(1+\epsilon)^2+\tau_\mathrm{s}^2}\right]\frac{\eta}{1+\epsilon}v_\mathrm{K} \tag{2.56}$$

$$v_{R,\mathrm{d}} = -\frac{2\tau_\mathrm{s}}{(1+\epsilon)^2+\tau_\mathrm{s}^2}\eta v_\mathrm{K} \tag{2.57}$$

$$v_{\phi,\mathrm{d}} = v_\mathrm{K} - \left[1 - \frac{\tau_\mathrm{s}^2}{(1+\epsilon)^2+\tau_\mathrm{s}^2}\right]\frac{\eta}{1+\epsilon}v_\mathrm{K} \tag{2.58}$$

where ϵ is the ratio of the dust to the gas density and the subscripts d and g denote dust and gas variables, respectively.

Looking at the radial velocity of the dust and assuming $\epsilon \ll 1$, we discover a mayor problem: Dust naturally drifts towards the star. This happens because in a steady-state, the gas rotates at a slightly sub-keplerain velocity because of the gas pressure gradient. The dust on the other hand, which does not feel the gas pressure gradient of the disk, wants to rotate with keplerian orbital velocity. Because of the mutual drag force, small particles will now be forced to rotate at the orbital speed of the gas, while large particles will feel a head wind due to the gas, slowing them down in both cases. This forces the particles to move to a smaller orbit where their orbital velocity matches the keplerian speed, leading to steady inward drift. The fastest drift velocities are obtained for particles with $\tau_\mathrm{s} \approx 1$, while particles with $\tau_\mathrm{s} \ll 1$ will be tightly coupled to the gas and therefore rotate with the same speed as the gas. Particles with $\tau_\mathrm{s} \gg 1$ will on the other hand rotate on keplerian orbits and the gas drag will not influence them significantly. For increasing dust to gas ratios ϵ, the dust will eventually dominate the motion of the gas and the dust inward drift is replaced by an outward drift of the gas.

The equations for the azimuthal velocity of both dust and gas, we see that the velocities of both species are always sub-keplerian and for very small Stokes numbers, the azimuthal velocities approach the gas velocity of a pure gas disk. From the above form of the equations it is also directly visible that dust and gas rotate with a common center of mass velocity $v_\mathrm{COM} = v_\mathrm{K} - \frac{\eta}{1+\epsilon}v_\mathrm{K}$, and the deviations due to the stokes number are only of the order τ_s^2. For small dust to gas ratios the gas will again be unaffected by the dust drag, whereas for very large ϵ the dust will rotate almost keplerian as it would without the gas present.

To calculate the vertical settling velocity of the particles, we now to additionally assume that the disk is quiescent and that $v_\mathrm{g,z} = 0$. Then the particles fall with their *terminal velocity* which is determined by the balance of the vertical component of gravity $|F_{Grav}| = m_\bullet \Omega_\mathrm{K}^2 z$ and the drag force $|F_\mathrm{D}|$ from 2.50. Assuming the particle is in the Epstein regime, the particle settling velocity is given by

$$v_\mathrm{settle} = -\Omega_\mathrm{K}\tau_\mathrm{s}z \qquad . \tag{2.59}$$

This approximation only holds for particles with St< 1, for which particles settle down to the midplane. Particles with larger St will undergo a damped oscillation around the midplane with the largest particles moving similar to planets on inclined orbits.

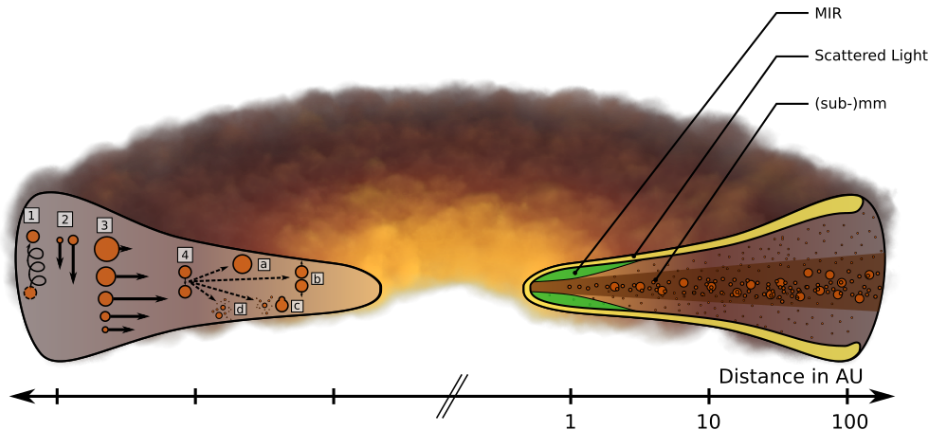

Figure 2.7: Artist impression of a protoplanetary disk showing the motion of dust particles on the left and the visibility of dust in different observation bands on the right. Dust particles are lifted from the midplane of the disk by turbulence (1) and settle down due to the vertical component of gravity (2). Additionally, they drift towards the star with a velocity depending on their size (3), with intermediate size particles with St=1 drifting the fastest. Particles will collide in the disk (4), with collisions having different outcomes depending on the relative particle sizes and velocities: slow collisions of small particles lead to sticking (4a), higher velocity collisions eventually lead to bouncing (4b), mass transfer (4c) and eventually catastrophic destruction (4d) for the highest velocity collisions. The right side displays the distribution of particles in the disk with larger particles settling down to the midplane and small particles staying suspended at higher altitude. The yellow band shows the regions of the disk probed with scattered light observations at visual wavelegths, the green shows the parts of the disk visible to mid-infrared observations which probe the warm dust in the inner few AU of the disk, whereas sub-mm observations show the emission of larger grains near the midplane of the mid to outer (cold) disk. *Adapted from Testi et al. (2014), T. Birnstil*

In a quiescent disk, small particles would now settle down into a razor thin particle disk. However, disks are always turbulent to a certain degree, either due to the turbulence mechanisms discussed in previous sections or due to the fact that dust dominated gas flow also develops turbulence. Turbulent motions lead to particle diffusion, which opposes settling and leads to a dust disk with finite thickness

$$\rho_d(R,z) = \rho_d(R) * e^{\left(-\frac{z^2}{2H_\mathrm{d}^2}\right)} \tag{2.60}$$

with the dust disk scale height H_d determined by (Dubrulle et al. 1995)

$$H_d = H_g\sqrt{\frac{\delta}{\tau_s + \delta}} \quad . \tag{2.61}$$

Here, the dust diffusion is given as $D = \delta c_s H$ with the coefficient δ determined in the same fashion as the turbulent gas diffusion parameter α. The ratio of mass diffusion of dust and gas, sometimes called the *Schmidt number*, is then given by

$$\mathrm{Sc} = \frac{D_\mathrm{g}}{D_\mathrm{g}} = \frac{\alpha}{\delta} \quad . \tag{2.62}$$

For the last equality it is assumed that the ratio of the momentum diffusivity (given by the kinematic viscosity) and the mass diffusivity D_g of the gas (confusingly also called the Schmidt number) is unity. Youdin & Lithwick (2007) showed that for general values of St the Schmidt number can be approximated as $\mathrm{Sc} \simeq 1 + \mathrm{St}^2$. For MRI disks, Sc has been determined in simulations as close to unity for small particles (Johansen & Klahr 2005) in agreement with the above formula, but this cannot generally be assumed for other instabilities, especially as e.g. the VSI exhibits anisotropic turbulent transport, where Sc depends on direction and care has to be taken in evaluating either form of Sc.

2.2.4 Dust Growth from ISM to Pebbles and Beyond

The growth of dust grains from sub-micron sized monomers to >km sized planetesimals is a complicated and not yet well understood process, though there have been significant advances in recent years. In this section, I will give a brief overview of the prevalent theories based mainly on the review by Birnstiel et al. (2016). For a more in-depth discussions of the individual theories I recommend the reviews by Birnstiel et al. (2016), Testi et al. (2014) and Johansen et al. (2014) for further reading.

Collisional growth

For micron to meter sized particles, growth mainly occurs through collisions, whose outcome mainly depends on the relative velocity of the colliding particles. For the smallest particles, this velocity is dominated by the particles Brownian motion. As the particles grow, first random motions due to turbulence become more important and then systematic velocity differences due to radial drift and vertical settling dominate. Figure 2.8 shows the combined differential velocity for different particle sizes.

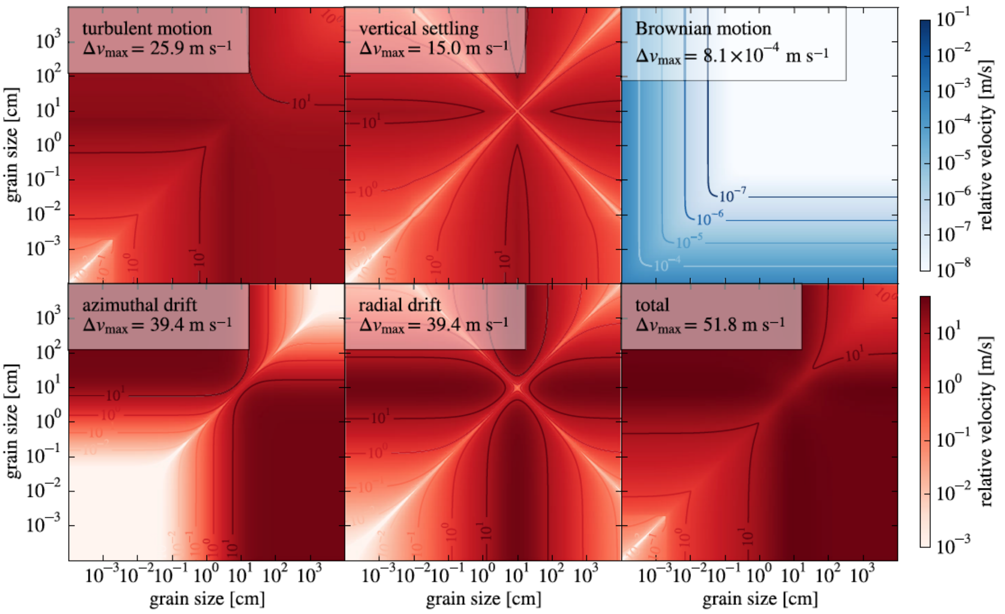

Figure 2.8: Contributions to the relative particle velocity as a function of both particle's sizes: Turbulence (upper left), vertical settling (upper center), Brownian motion (upper right) and azimuthal (lower left) and radial (lower center) drift. The lower right panel shows the total relative velocity. The values are calculated for a disk with $\alpha = 10^{-3}$, T=63 K and $\Sigma_{\rm g} = 16 {\rm g/cm}^2$ at a radius of 10 AU.

Because particle collisions don't depend only on the velocities of the collision partners, realistic collision models are complicated. They additionally depend on the size of the particles, the impact factor, their fractal dimensions, chemical composition, porosity and many other factors. Laboratory studies can aid to understand some of these properties (see e.g. Blum & Wurm (2008), Testi et al. (2014), Johansen et al. (2014) and references therein), but the size of the parameter space involved makes it impractical to explore. However, five different general outcomes of collisions have been identified (see also element 4 in figure 2.7):

Sticking: Particles undergoing low velocity collisions will stick together.

Bouncing: Particles colliding will bounce off each other with no changes in mass, though a compactification is possible (Zsom et al. 2010).

Fragmentation: High velocity collisions of similar size particles result in destruction of both collision partners (Brauer et al. 2008; Birnstiel et al. 2009).

Mass transfer: A small particle colliding with a large one is destroyed but deposits some of its mass on the large particle (Wurm et al. 2005).

Erosion: A small particle removes some of the mass of the larger particle it collides with.

The relative velocity at which catastrophic fragmentation occurs depends on the properties of the grains. Laboratory studies show that silicate grains fragment at collision velocities above ∼ 1 m/s, whereas icy grains fragment only above ∼ 10 m/s. Erosion sets in at relative velocities ∼ 15 m/s. Therefore the lower left panel of figure 2.8 already shows that silicate grains will not grow beyond a few mm whereas icy grains can reach cm or more at distances of about 10 AU from the star. Generally, this maximum grain size at which fragmentation occurs lies between around 1 millimeter in the outer parts of the disk and few meters in innermost parts. Grains cannot grow beyond this size, which is known as the *fragmentation barrier*.

Even below this critical threshold, compact particles will start to bounce off each other instead of sticking together. This stalls growth at sizes somewhat below the fragmentation barrier known as the *bouncing barrier*. Because bouncing does not happen for porous grains, this barrier is the easiest to overcome.

Another problem to growth is the radial drift of particles discussed in section 2.2.3. If the drift timescale of the dust grains is smaller than the time they need to grow, the particles will drift towards the star before they are fully grown. Because larger grains drift faster than smaller ones (at least for St<1), the larger grains are removed preferentially, leading to a maximum size for the particles that remain at a certain location. This largest size is termed the *drift barrier*. Because both the drift barrier and the fragmentation barrier occur at particle sizes of about 1 m at 1 AU, both are sometimes summarized under the more general term *meter-size barrier*.

Growing beyond the ”meter-size” barrier

Many pathways have been proposed to overcome these barriers and grow to sizes beyond a few meters. One is to assume that there exist lucky seed particles which are larger than most of the grains. These grains could then grow through mass transfer collisions. Windmark et al. (2012) and Garaud et al. (2013) showed that using a velocity distribution for the collision calculations instead of a single mean velocity allows some lucky particles to avoid getting stuck at the bouncing. But the use of a velocity distribution also means that smaller particles fragment in collisions with partners of similar size slowing down the overall growth of particles. And even if a particle is lucky enough to avoid the bouncing and the fragmentation barrier, it has to be very lucky to grow significantly in size through mass transfer collisions before getting destroyed.

Another possibility arises when the porosity evolution of the grain is taken into account. Up until now, collisions were assumed to be between two compact grains, but simulations have shown that grains grow rather fluffy (Dominik & Tielens 1997; Paszun & Dominik 2009; Ormel et al. 2007; Okuzumi et al. 2012). Additionally, icy grains fragment at higher collision velocities. Therefore, beyond the ice line but inside 10 AU, it is possible for icy grains to grow in a porous fasion fast enough to reach the stokes drift regime. There the growth time scale is inversely proportional to the particle size leading to fast growth and circumvention of the drift barrier (Okuzumi et al. 2012). Compactification of the grains then occurs for larger grains due to ram pressure and self-gravity (Kataoka et al. 2013). However, Krijt et al. (2015) showed that the inclusion of erosion can stall the growth of the particles at St $\approx$ 1 if the collision velocity surpasses the threshold velocity for erosion.

Planetesimal Formation in Dust Traps

An entirely different way to circumvent the growth barriers is to jump the size regime entirely and grow from cm sized grains to km sized boulders via gravitational collapse

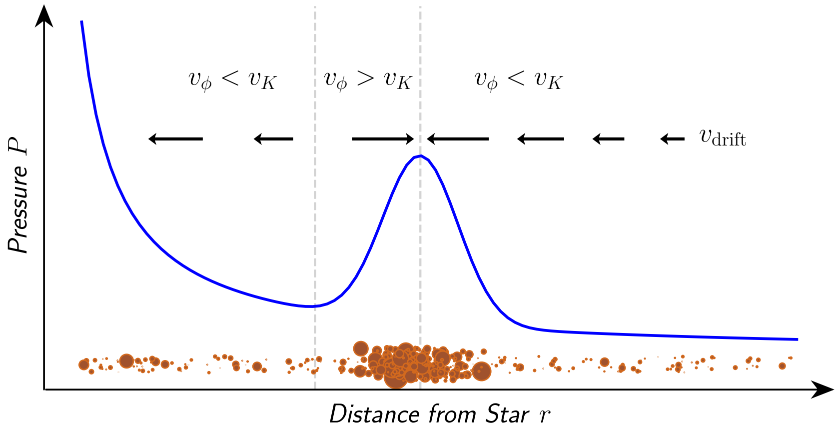

Figure 2.9: Illustration explaining the concentration of particles in local pressure maxima. The blue curve shows the global pressure gradient of a protoplanetary disk overlaid with a local pressure bump. The pressure maximum alters the local azimuthal velocity ϕ, leading to outward particle drift in the region with radii slightly smaller than the P maximum and enhanced inward drift at radii slightly larger than it, indicated by the black arrows. This enables particles to swiftly accumulate inside the pressure bump, as shown by the distribution of brown pebbles.

(Johansen et al. 2006, 2007, 2011). This collapse can happen because for dust-to-gas ratios above unity, the concentration of dust becomes self-amplifying due to a process termed streaming instability (Youdin & Goodman 2005). Then the dust load can become large enough inside a clump formed that it exceeds the minimum density required to collapse despite turbulence and disk shear. A criterion defining this critical density was presented in Klahr & Schreiber (2016) and elaborated on in Schreiber (2018). They also show that via the collapse of a particle cloud objects of ~ 100 km form, a size characteristic of objects in both the asteroid and Kuiper belts.

A hindrance to this model is however the requirement of $\epsilon \geq 1$, which is not generally given in a protoplanetary disk where the typical value of ϵ is 0.01, two orders of magnitude below the necessary value. The solutions presented to overcome this can be sorted into two categories: global and local enhancement of particles. The former increases the dust content of the disk by decreasing the gas content, which can be achieved by photoevaporation, winds or gas accretion by a giant planet. Once the disk metallicity is super-solar ($Z \gtrsim 0.02$) , the streaming instability can be invoked to form particle clumps on a global scale (Bai & Stone 2010; Carrera et al. 2015; Johansen et al. 2015). As photoevaporation occurs in the late stages of disk evolution and accretion assumes an already present planet, this mechanism may explain the formation of asteroids and rocky planets, but is rather ill suited explain the formation of cores for large gas giants.

The latter, a local enhancement of the dust density, can occur whenever a local pressure maximum exists in the disk (Whipple 1972). Equations 2.55 -2.58 show that dust drifts radially inwards if $\eta > 0$ and outwards if $\eta < 0$, which is equal to the disk gas rotating at sub-keplerian or super-keplerian velocity, respectively. Figure 2.9 shows now the case where the disk has a local pressure maximum: Inside

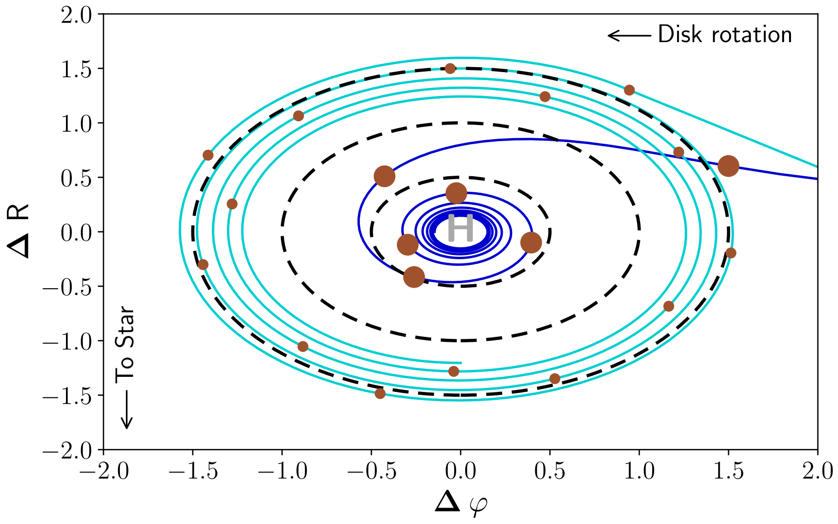

Figure 2.10: Illustration explaining the concentration of particles in anti-cyclonic vortices. As shown in figure 2.9, particles drift towards local pressure maxima like the ones found in anti-cyclones (H = high pressure system). Particles encountering a vortex will thus be caught by it and spiral towards the center. Because larger particles are affected stronger by radial drift, they will concentrate more quickly towards the point of highest pressure. This leads to a size segregation with distance from the vortex center as illustrated by the two blue curves, where larger dots represent larger grain sizes.

the radial position of the maximum, the pressure gradient is positive, leading to $\eta < 0$ and outward particle drift. Outside of the maximum, the pressure gradient is strongly negative, leading to $\eta > \eta_{\mathrm{global}} > 0$ and an enhanced inward drift. Because $\eta = 0$ at the point of the pressure maximum, the dust rotates at keplerian speed and does not drift. Therefore, dust naturally accumulates inside local pressure maxima, which are thus often termed *dust traps*.

Because local dust traps can occur early in the lifetime of a protoplanetary disk, much work has been done in recent years to identify them. One possibility identified are zonal flows, axisymmetric structures with a local pressure maximum in radial direction. They form in disks with active magneto-rotational instability and have been shown to efficiently concentrate particles and form precursors to planetesimals (Johansen et al. 2009, 2011; Dittrich et al. 2013).

Another possibility is the concentration of particles in vortices. As discussed in section 2.1.5, protoplanetary disks only contain anti-cyclonic vortices. And because they have a pressure maximum in their center, they can act as particle traps (Barge & Sommeria 1995). Particles who encounter a vortex will then spiral towards its center, with larger particles concentrating towards the center more quickly then smaller ones as shown in figure 2.10. Klahr & Henning (1997) and Lyra & Lin (2013) presented theoretical predictions on the particle density enhancement possible inside vortices, and simulations of dust in in both fiducially created and spontaneously formed vortices have confirmed their nature as traps (Fromang & Nelson 2005; Klahr & Bodenheimer 2006; Meheut et al. 2012; Flock et al. 2017a). Raettig et al. (2015), using shearing-box simulations and 2 way drag forces, showed that particles trapped in vortices can trigger the streaming instability locally and start to form clumps, even for initially low global dust-to-gas ratios. Because the back reaction of the particles affects the gas flow, vertically integrated 2D simulations showed that vortices get destroyed once the particle load inside them becomes to largeSurville et al. (2016). Recent 3D simulations published in Lyra et al. (2018) however showed that vertically extended vortices do not suffer the same fate, but merely get deformed close to the dust rich midplane.

2.3 Radiative Transfer

So far, we have only looked at the theoretical models used to describe protoplanetary disks. To test these models against observations, we need to calculate how our models would look like when seen through a telescope. This is where we need Radiative transfer calculations.

A fundamental principle of radiation is that, if we look at a package of rays of light travelling through vacuum, the intensity I_ν at frequency ν of the ray stays constant:

$$\frac{\partial I_\nu}{\partial s} = 0 \tag{2.63}$$

where s represents the distance travelled along the ray. Note that, in general, $I_\nu = I_\nu(s, \mathbf{n})$ is a function of both the distance s travelled and the direction of the ray $\mathbf{n}$.

If the rays travel through a medium, energy can be added through emission or subtracted through absorption or scattering. Therefore, neglecting scattering for the moment, equation 2.63 modifies to the fundamental radiative transfer equation

$$\frac{\partial I_\nu}{\partial s} = j_\nu - \alpha_\nu I_\nu \tag{2.64}$$

where j_ν is the emission coefficient and α_ν is the absorption coefficient, which is defined as the inverse of the photon mean free path $\lambda_{\text{photon}} = \frac{1}{\alpha_\nu}$. Because the mean free path is dependent on the density of the traversed medium, we can write $\alpha_\nu = \rho\kappa_\nu$ with κ_ν being the mass-weighted opacity of the medium. We can then define the optical depth of the medium as:

$$\tau = \int_{s_0}^{s_1} \rho(s)\kappa_\nu(s)\mathrm{d}s \tag{2.65}$$

which gives the logarithm of the incident radiation at s_0 to the transmitted radiation at s_1 and therefore gives a measure at how effective the medium is at absorbing photons. A medium with optical depth $\tau \ll 1$ absorbs only a fraction of the incident photons and is termed to be optically thin, whereas a medium with $\tau \gg 1$ is said to be optically thick.

Using the optical depth, equation 2.64 can be rewritten to:

$$\frac{\partial I_\nu}{\partial \tau} = -I_\nu + S_\nu \tag{2.66}$$

where I introduced the source function $S_\nu = \frac{j_\nu}{\alpha_\nu}$ as the ratio between emission and absorption coefficient. In local thermal equilibrium (LTE), Kirchhoff's law states that this ratio has to be equal to the Planck function B_ν, so $S_\nu = B_\nu$. Integrating equation 2.66 then gives the formal solution to the radiative transfer equation

$$I_\nu = e^{-\tau_\nu} \left[I_{\nu,0} + \int\limits_0^{\tau_\nu} e^{\tau'_\nu} S_\nu(\tau'_\nu)\, \mathrm{d}\tau'_\nu \right] \quad . \tag{2.67}$$

In protoplanetary disks we also have to consider scattering of electromagnetic radiation off of dust particles. Describing the radiation field as a field of rays passing through a point x, scattering can be described to transfer energy from one ray to another ray pointing into a random direction. Therefore we can introduce the scattering absorption coefficient $\alpha_\nu^{\mathrm{scat}}$ and the scattering emission coefficient j_ν^{scat}. The absorption and emission coefficients then become

$$\alpha_\nu^{\mathrm{tot}} = \alpha_\nu^{\mathrm{abs}} + \alpha_\nu^{\mathrm{scat}} \qquad\qquad j_\nu^{\mathrm{tot}} = j_\nu^{\mathrm{abs}} + j_\nu^{\mathrm{scat}} \qquad , \tag{2.68}$$

and the source function is now given as

$$S_\nu = \frac{j_\nu^{\mathrm{abs}} + j_\nu^{\mathrm{scat}}}{\alpha_\nu^{\mathrm{abs}} + \alpha_\nu^{\mathrm{scat}}} \quad . \tag{2.69}$$

Defining the photon destruction probability as

$$\epsilon_\nu = \frac{\alpha_\nu^{\mathrm{abs}}}{\alpha_\nu^{\mathrm{abs}} + \alpha_\nu^{\mathrm{scat}}} \tag{2.70}$$

and the albedo as

$$\eta_\nu = 1 - \epsilon_\nu = \frac{\alpha_\nu^{\mathrm{scat}}}{\alpha_\nu^{\mathrm{abs}} + \alpha_\nu^{\mathrm{scat}}} \tag{2.71}$$

the source function can be rewritten using the absorption and scattering source functions as

$$S_\nu = \epsilon_\nu S_\nu^{\mathrm{abs}} + (1 - \epsilon_\nu) S_\nu^{\mathrm{scat}} \tag{2.72}$$

and, assuming LTE, equation 2.66 becomes

$$\frac{\partial I_\nu}{\partial \tau} = -I_\nu + \epsilon_\nu B_\nu + (1 - \epsilon_\nu) S_\nu^{\mathrm{scat}} \tag{2.73}$$

where the absorption source function has again been replaced by the Planck function. The scattering source function can now be an arbitrarily complex function of the radiation field and therefore the right hand side is not known a priori any more. A solution to equation 2.73 can therefore only be obtained in general only by using numerical methods. In general, S_ν^{scat} can be written as

$$S_\nu^{\mathrm{scat}} = \frac{1}{4\pi} \oint I_\nu(\mathbf{n}) \phi(\mathbf{n}, \mathbf{n}') \mathrm{d}\Omega \tag{2.74}$$

with $\mathbf{n}$ and $\mathbf{n}'$ being the direction of the incoming and outgoing ray, respectively. $\phi(\mathbf{n}, \mathbf{n}')$ is the scattering source function, which has to fulfil $\phi(\mathbf{n}, \mathbf{n}') = \phi(\mathbf{n}', \mathbf{n}) \geq 0$.

For isotropic scattering, where $\mathbf{n}'$ is independent of $\mathbf{n}$, the source function takes the simple form

$$\phi(\mathbf{n}, \mathbf{n}') = 1 \qquad . \tag{2.75}$$

A more commonly used approximation is the Heyney-Greenstein phase function. Defining the scattering angle θ between $\mathbf{n}$ and $\mathbf{n}'$ via $\mu = \cos(\theta) = \mathbf{n} \cdot \mathbf{n}'$ and the scattering anisotropy factor as

$$g_\nu = \frac{1}{4\pi} \oint \phi(\mu) \mu \mathrm{d}\mu \qquad , \tag{2.76}$$

the phase function can in this approximation be expressed as

$$\phi(\mu) = \frac{1}{2} \frac{1 - g^2}{(1 + g^2 - 2g\mu)^{3/2}} \qquad . \tag{2.77}$$

The values of g_ν can then be tabulated along with the opacities prior to the simulation and the radiative transfer calculation uses equation 2.77.

2.4 Numerical Methods Used in this Thesis

During this thesis, two code packages are used: the magneto-hydrodynamics code PLUTO and the radiative transfer code RADMC3D. Both codes come with an extended user manual and documentation, so I will only briefly introduce the main concepts here. For further reading, the reader is encouraged to consult Toro (2009) for a general introduction into numerical magneto-hydrodynamics and Mignone et al. (2007) for PLUTO in particular. For more information on numerical radiative transfer, a good resource is the review of Steinacker et al. (2013).

2.4.1 Numerical Hydrodynamics with PLUTO

The PLUTO code Mignone et al. (2007) is a multi-purpose magneto-hydrodynamics code able to compute relativistic and non-relativistic hydrodynamical and magneto-hydrodynamical flows. It solves equations 2.1-2.3 using a finite volume approach on a static or adaptively refined grid. The code can be freely downloaded from `http://plutocode.ph.unito.it`.

Godunov's method

Finite volume methods solve the integral form of equations of the general form

$$\frac{\mathrm{d}\mathbf{U}}{\mathrm{d}t} + \nabla \cdot \mathbf{T}(\mathbf{U}) = \mathbf{S}(\mathbf{U}) \tag{2.78}$$

using Godunov's method Godunov (1959), which can generally expressed as a three step process: Reconstruct, solve and average. Here, $\mathbf{U} = (\rho, \rho v, \rho e)$ represents the vector of conserved variables, $\mathbf{T}(\mathbf{U})$ is a rank 2 tensor containing the fluxes of each component of $\mathbf{U}$ as rows and $\mathbf{S}(\mathbf{U})$ is the vector of source terms.

In step 1, reconstruct, the value of $\mathbf{U}$ at the cell interface is constructed from the grid cell average. This is archived in the most basic case by using the volume

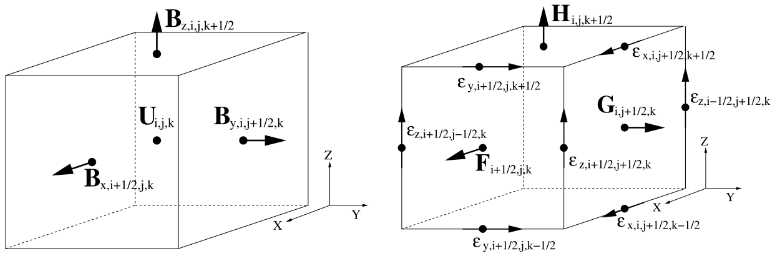

Figure 2.11: Schematic explaining the different quantities used in the text. Left shows the cell averaged value of U positioned at the cell center and the values of the magnetic field at the cell interfaces. Right shows the inter-cell fluxes in the x, y and z direction as F, G, and H, respectively, positioned at the respective cell interface. *Image from Stone et al. (2008).*

averaged value itself, but more sophisticated schemes usually use linear or higher order polynomial interpolations. With this, a Riemann problem is constructed at the cell interface. In the most general form, the Riemann problem can be expressed as

$$\mathbf{U} = \begin{cases} U_{i+\frac{1}{2},\mathrm{L}} & x < x_{i+\frac{1}{2}} \\ U_{i+\frac{1}{2},\mathrm{R}} & x > x_{i+\frac{1}{2}} \end{cases} \tag{2.79}$$

where $U_{i+\frac{1}{2},L(R)}$ is the value of U obtained from the left (right) side of the cell interface located at $x_{i+\frac{1}{2}}$. Because the

Step 2, as the name suggests, solves this problem using a so called Riemann solver. Using an exact Riemann solver is usually a cumbersome and computationally expensive endeavour, so approximate Riemann solvers are usually implemented. The most widely used ones are the solver of Roe or the class of solvers based on a method developed by Harten, Lax and vanLeer. A good introduction into Riemann solvers and Godunov's method in general is Toro (2009), which also contains algorithms for implementing the solvers mentioned above. As the result of this step, one obtains the Riemann fluxes as a solution, which can then be used to evolve the system in time.

Step 3, average, advances the system in time using

$$U_i^{n+1} = U_i^{n+1} + \frac{\Delta t}{\Delta V}\left[A_{i+\frac{1}{2}}F_{i+\frac{1}{2}} - A_{i-\frac{1}{2}}F_{i-\frac{1}{2}}\right] \qquad , \tag{2.80}$$

where U_i^n and U_i^{n+1} are the cell averages at time t and $t+\Delta t$, respectively, and $F_{i\pm\frac{1}{2}}$ are the Riemann fluxes from the left and right cell interface. The cell interface area is represented by $A_{i\pm\frac{1}{2}}$ and the cell volume by ΔV. Δ represents the time step.

To ensure stability of the method, the cell average can only depend on the Riemann problem from its direct left and right interface. To ensure this, the time step has to be chosen in a manner that the signal from one interface does not reach the next interface. The timestep is therefore limited by the *Courant-Friedrichs-Lewy* condition:

$$\Delta t = C \min_d \frac{\Delta l^d_{\mathrm{min}}}{|\lambda^d_{\mathrm{max}}|} \tag{2.81}$$

where $\Delta l^d_{\mathrm{min}}$ represents the smallest grid cell size and $|\lambda^d_{\mathrm{max}}|$ the fastest signal speed of each dimension d. C is the Courant number which obeys $C \leq 1$. For the methods employed in this thesis, a value of $C = 0.3$ is chosen.

Methods available in PLUTO

The goal of the PLUTO developers was (and is) to provide a modular multi-purpose code. Therefore, for all three stages mentioned above, multiple options are implemented in the code.

For the interpolation/reconstruction the available options are flat reconstruction for 1st order and multiple linear, total variation diminishing (TVD) reconstruction algorithms for 2nd order accuracy in space, e.g. monotonized central difference or the harmonic mean limiter of van Leer. A full list is available in the code manual. Higher order available limiters are the third order Weighted Essential Non Oscillatory (WENO) and a fourth order piecewise parabolic (PPM) reconstruction. Although these schemes are higher order, the global spatial accuracy of the code is second order.

The Riemann solvers implemented in the code are, among others, the solvers of Roe, Lax-Friedrich and Harten-Lax-vanLeer (HLL) as well as modifications of the latter for inclusion of the central contact wave (HLLC) and Alvfen waves (HLLD). The time integration in the last step can be either done using an Euler or a 2nd or 3rd order Runge-Kutta scheme. Alternatively, for some configurations, the use of the MUSCL[1]-Hancock scheme is possible. Because experience has shown some combinations of options to give better results than others, the code manual contains a list of suggested combinations.

Throughout this thesis, the following configuration is chosen for simulations: Piecewise parabolic reconstruction, the hllc Riemann solver and a 3rd order Runge-Kutta scheme for the time integration.

A Note on Coordinate Systems

The PLUTO code can be used with cartesian, cylindrical and spherical grids, which can either be static or be refined at runtime using adaptive mesh refinement. Because spherical geometry is the closest match to protoplanetary disk models, computations presented in this thesis are done in spherical coordinates only, using a static grid with linear grid cell division in polar and azimuthal direction and a logarithmic grid in radial direction. When appropriate, a coordinate transformation to cylindrical coordinates is made for visual presentation of the results, the underlying averages however are always done in spherical coordinates and the data is stored on the spherical grid defined in the simulation.

2.4.2 Radiative transfer with RADMC3D

RADMC3D Dullemond et al. (2012) is a continuum radiative transfer code for dusty protoplanetary disks, freely available from `http://www.ita.uni-heidelberg.de/~dullemond/software/radmc-3d/` . It uses the Monte Carlo method to simulate

---

[1] Monotonic Upwind Scheme for Conservation Laws

multiple scattering in dusty media using different levels of scattering accuracy and compute the dust temperature and images of the disk self-consistently. The code comes with an extensive manual explaining the code functionality and the basics of Monte Carlo radiative transfer calculations, and on which most of this section is based on. The lecture notes of Dullemond (2013) are used as an additional source of information mainly on the opacity calculation.

Monte-Carlo Method

As the name Monte Carlo, already suggests, Monte-Carlo methods use a statistical approach to simulate the radiative transfer equation. This makes them a different class of methods from for example discrete ordinate methods, which instead of solve the radiative transfer equation directly.

In this method, the luminosity of the source, e.g. the central star, is divided into thousands of photon packages, which in turn represent many photons. These packages are sent successively into the simulation in randomly drawn directions. The photon packages then travel through the medium for some time until they undergo a scattering or absorption event. The distance at which this happens is drawn again randomly using a distribution function dependent on the optical depth of the surrounding medium. If the photon package is scattered, the new direction is drawn randomly from a probability function dependent on the scattering approach selected. If the photon is instead absorbed, and we are calculating the temperature of the medium, we force it to be immediately re-emitted in a random direction and with a new frequency calculated with the prescription from Bjorkman & Wood (2001). When the absorption/re-emission event happens, the photon package deposits energy in the cell and therefore changes the temperature in it. The photon package travels this way through the simulation until the package reaches the edge of the simulation grid and escapes. If we are instead interested in the scattering source function, the calculation can additionally be stopped once the photon package has travelled many optical depths (usually around 30) and can therefore be considered extinct. Then the next photon package is launched and the calculation repeats until all packages have traversed the system.

Opacity Calculation

Among other input parameters, RADMC3D needs to be supplied tabulated opacities of all grain species. These can be calculated using the Mie scattering code of Bohren & Huffman (1983), modified by B. Draine [2]. The RADMC3D code package includes a fortran wrapper to bring the output of the code into code compatible form, as well as a full python version of the code.

Mie scattering Mie (1908) calculates the scattering and absorption opacity using a spherical harmonic series expansion of the solution to the Maxwell equations describing the interaction of light with a dielectric homogeneous sphere. Because Mie theory only applies to spherical grains, it can be a bad approximation for realistic grains, which can have any kind of shape and may even align with e.g. the magnetic field in the disk. But for most applications the assumptions made are acceptable. To compute the opacities using Mie theory, the complex refractive index

---

[2] Available from `https://www.astro.princeton.edu/~draine/scattering.html` .

of the materials the grains are composed of have to be supplied. Grains found in protoplanetary disks are mostly comprised of silicates, carbon, ices or a mixture of these. The material properties can be obtained from the Jena Database of Optical Constants[3].

A Typical Production Run

Before the calculation can start, input files containing the dust (and if desired, the gas) densities for each grain size, the corresponding opacities for each grain size, the luminosity sources, the grid and a top level input file containing code flags have to be compiled. The work flow then has two steps: In step 1, invoked with `mctherm`, the dust temperature is calculated using the Monte-Carlo algorithm described above. Here, the dust is assumed to be in thermal equilibrium with the gas. This step outputs the file `dust_temperature.dat`.

Armed with the dust temperature, one can proceed to step 2: The computation of a spectral energy distribution (SED, using `sed`) or an image (using `image`). During this step, because we have the temperature and therefore the absorption but not the scattering source function, RADMC3D first carries out a scattering Monte Carlo run to compute the scattering source function, which is to large to store on file permanently. The scattering in RADMC3D can be treated as isotropic or anisotropic using either the Heyney-Greenstein approximation described above or by considering the full scattering matrix (see the code documentation for more information). Then the image is calculated using Monte Carlo Ray tracing. Because the code traces a preset finite amount of photon packages and therefore only a finite subset of photon paths, the final image can contain Monte Carlo noise. In most cases, the default number of photon packages is sufficient, but especially when dealing with optically thick media a higher number of photon packages may be required to get rid of the noise.

---

[3] `https://www.astro.uni-jena.de/Laboratory/Database/jpdoc/f-dbase.html`

CHAPTER 3

VORTEX FORMATION AND SURVIVAL IN PROTOPLANETARY DISKS SUBJECT TO VERTICAL SHEAR INSTABILITY

From Manger & Klahr (2018)

3.1 Introduction

Turbulence in disks around young stars is still one of the most interesting questions in modern astrophysics (Turner et al. 2014). Balbus & Hawley (1991) introduced the magneto-rotational instability (MRI) as a promising source of turbulence with an alpha viscosity (Shakura & Sunyaev 1973) large enough to explain angular momentum transport on timescales set by observations. But more recent work shows the MRI to be hampered by non-ideal magnetic effects such as resistivity or ambipolar diffusion (Lesur et al. 2014). They show that the instability can be damped efficiently in parts of the disk by low ionization fractions, where then other sources of turbulence can and have to be considered (Lyra & Klahr 2011).

Several possible mechanisms for pure hydrodynamic turbulence have since been proposed, acknowledging the fact that a Keplerian flow with radially increasing angular momentum profile is hydrodynamic stable as can be seen in a most general way from the Solberg-Hoiland criteria, which is derived for no thermal relaxation (Rüdiger et al. 2002). The global baroclinic instability (aka Subcritical Baroclinic Instability) (Klahr & Bodenheimer 2003; Petersen et al. 2007a,b; Lesur & Papaloizou 2010) and convective overstability (COS) (Klahr & Hubbard 2014; Lyra 2014) rely on radial temperature and density stratifications introducing convective cells in disks with moderate cooling times on the order of $\tau = 1/(\gamma\Omega)$. The Vertical Shear Instability (VSI) (Nelson et al. 2013; Richard et al. 2016; Stoll & Kley 2014) relies on short cooling times to remove the stable vertical stratification to tap into the energy of the vertical shear.

In all of those turbulence models, the formation of vortices has been observed. Raettig et al. (2013) showed them in local simulations of subcritical baroclinic instability, (Flock et al. 2015) in a global context at the edge of the MRI dead zones. The Rossby Wave Instability (Papaloizou & Pringle 1984, 1985; Lovelace et al. 1999; Li et al. 2000, 2001) has been shown to break axisymmetric rings into large vortices. Richard et al. (2016) showed the possibility of small vortex formation within disks susceptible to VSI and Latter & Papaloizou (2018) found the Kelvin Helmholtz Instability acting as a parasitic instability on the VSI modes and forming small vortices in the disk.

Because vortices are naturally identified with local pressure maxima in the context of PPDs, they act as particle traps (Barge & Sommeria 1995). They are found to enhance the dust to gas ratio locally, aiding planetesimal formation via triggering the streaming instability (Raettig et al. 2015) and accelerate core growth for giant planets via pebble accretion (Klahr & Bodenheimer 2006). Large vortices have also been discussed as explanation for features found in (sub-)mm observations of protoplanetary disks with ALMA (van der Marel et al. 2013) and VLA (Carrasco-González et al. 2016).

In this chapter we investigate vortex formation and survival in protoplanetary disk simulations undergoing Vertical Shear Instability, reexamining the work of Richard et al. (2016). We find that once we loosened the restriction to small azimuthal domains (large azimuthal wavenumbers m) and allowed for simulation domains of $\varphi = 180°$ and $\varphi = 360°$, we find large vortices forming in the disks after a few hundred orbits. We also find these larger vortices to survive for hundreds of local orbits, making them excellent particle traps and candidates for planetesimal formation sites. With this, we stress again that non-axisymmetry plays an important role in assessing disk turbulence features (Klahr et al. 1999).

The chapter is structured as follows: Section 3.2 lays out the numerical set-up used in all computations. In Section 3.3 we present our results and in section 3.4, we discuss them in context of recent literature. Finally, section 3.5 summarizes our findings and presents an outlook on future work.

3.2 Simulation Setup

We conduct 3 dimensional simulations using the magneto-hydrodynamics code PLUTO[1]. In this chapter, we use 2 coordinate systems. The simulations are carried out on a spherical grid (r, θ, φ), the model setup and analysis are presented in cylindrical coordinates (R, ϕ, Z),

We implement the disk setup following Nelson et al. (2013). The gas density is defined by

$$\rho = \rho_0 \left(\frac{R}{R_0}\right)^p \exp\left(-\frac{Z^2}{2\,H^2}\right) \tag{3.1}$$

with the disk scale height $H = \frac{c_s}{\Omega_K}$. We chose a ideal equation of state $\rho e = \frac{P}{\gamma - 1}$ with the specific internal energy e,the adiabatic index $\gamma = 5/3$[2] and $P = c_\mathrm{s}^2 \rho$ using a radially changing isothermal sound speed $c_\mathrm{s}^2 = c_0^2 \left(\frac{R}{R_0}\right)^q$. Note that the temperature is related to the isothermal sound speed via $c_\mathrm{s}^2 = kT/\mu m_H$ with k denoting the Boltzmann constant, μ the mean molecular weight and m_H the atomic mass of hydrogen, thus defining a radial temperature gradient in the disk.

---

[1] http://plutocode.ph.unito.it

[2] The value for γ in protoplanetary disks is closer approximated by 1.44 due to the diatomic nature of molecular hydrogen. We instead use the standard $\gamma = 5/3$ of PLUTO. This does not significantly affect the results due to the fast cooling applied in this chapter.

Table 3.1: Simulation parameters for all simulation conducted in this study. We give grid parameters, phi extent and resulting time and space averaged alpha values.

Run	$N_r \times N_\theta \times N_\phi$	$\phi_{\max}[^\circ]$	α
p45	$256 \times 128 \times 96$	45	$1.5 \cdot 10^{-3}$
p90	$256 \times 128 \times 192$	90	$1.4 \cdot 10^{-3}$
p180	$256 \times 128 \times 384$	180	$1.2 \cdot 10^{-3}$
p360	$256 \times 128 \times 768$	360	$1.0 \cdot 10^{-3}$

For all our simulations, we choose $-\frac{2}{3}$ and -1 for p and q respectively, satisfying the requirements set for the VSI.

The $q = -1$ is close to the maximum of $q = -1.5$ that one can expect in a viscously heated disk (see Eq. 11 in Bell et al. (1997)) in regions which are dominated by icy grains. The value for $p = -\frac{2}{3}$ is chosen to be consistent to models in which we try to simulate the COS, by using an identical setup as described here, but using a longer cooling time. This particular value of p has no significant impact on the VSI, but helps to maximise the radial buoyancy for the given p expressed in the radial Brunt-Vaissala frequency N_r^2 (Klahr & Hubbard 2014).

The geometrical scale height is then constant throughout the disk with $H/R = c_0/v_{\mathrm{Kepler}} = 0.1$, which is also nice to evaluate the simulation. H/R might actually be smaller in a real circumstellar disk (Bell et al. 1997) and we tested a value of $H/R = 0.05$, which was also the value choice in the work by Stoll & Kley (2014), yet (Flock et al. 2017b) again uses values of $H/R = 0.1$ for the outer disk. $H/R = 0.05$ simulations are computationally more expensive, as the pressure scale height has to be resolved by at least as many cells as in the $H/R = 0.1$ case, leading to 8 times more cells and reducing the time step by a factor of two. Once our $H/R = 0.05$ simulations are finished, we will publish them in comparison to the $H/R = 0.1$ cases, but we claim that smaller values of H/R will show similar results for runs with comparable resolution per scale height.

The scale height can be expressed as:

$$H \propto \left(\frac{R}{R_0}\right)^{(q+3)/2} \qquad , \tag{3.2}$$

and the initial angular velocity of the disk is given by

$$v_\phi = \Omega_{\mathrm{K}}\, R \left[1 + q - \frac{q\, R}{\sqrt{R^2 + Z^2}} + (p+q)\left(\frac{H}{R}\right)^2\right]^{\frac{1}{2}} \tag{3.3}$$

whereas the radial and vertical velocities are set to zero. All velocity components are initially seeded with a white noise perturbation of $10^{-4}\, c_{\mathrm{s}}$.

The cooling in our model is described by

$$\frac{dP}{dt} = -\frac{P - \rho T_{\mathrm{init}}}{\tau_{\mathrm{relax}}} \tag{3.4}$$

where $T_{\mathrm{init}}(R)$ is the initial Temperature profile and τ_{relax} is the relaxation time scale. It is set to $\tau_{\mathrm{relax}} = dt$ and is about $2 \cdot 10^{-3}/\Omega_0$ in all simulations. This is the shortest cooling time we can realise in our explicit cooling scheme, effectively leading to an almost locally isothermal disk.

In our numerical computations we use the hllc method (Toro 2009) with a ppm reconstruction scheme (Mignone 2014) for spatial integration and a 3rd order Runge-Kutta method for time integration. The mesh extends from $(0.5r_0, \pi/2 - 0.35, 0)$ to $(2r_0, \pi/2 + 0.35, \phi_{\mathrm{max}})$ with r_0 being the radius at $r = 1$ and ϕ_{max} given in table 3.1. We use a logarithmic grid in radial direction and a uniform grid otherwise to preserve the aspect ratio of the individual grid cells. This gives us a resolution of 18 cells per H in vertical and radial direction and 12 cells per H in azimuthal direction. For the largest run (p360), we used about 1.4 million cpu-hours.

We employ outflow boundary conditions in radial direction, reflective boundaries in vertical direction and periodic boundaries in azimuthal direction. To minimise mass loss in radial direction and generally wave reflection at the boundaries, we add damping layers at the inner and outer boundaries in the radial and polar direction with $\Delta R = 1.0\,H$ and $\Delta\theta = 0.05$. Inside the damping layers, we damp the velocities to their initial values if the velocity component normal to the boundary points inside the domain. For the damping we use:

$$\frac{dv_x}{dt} = -\frac{v_x - v_{x,0}}{\tau_{\mathrm{damp}}} \cdot f^2 \tag{3.5}$$

with the damping time $\tau_{\mathrm{damp}} = 0.1\frac{2\pi}{\Omega}$ and $f = \frac{R-R_{\mathrm{b}}}{\Delta R}$ in radial and $f = \max(\frac{R-R_{\mathrm{b}}}{\Delta R}, \frac{\theta-\theta_{\mathrm{b}}}{\Delta\theta})$ in meridional direction . R_{b} and θ_{b} denote the position of the boundary of the damping layer inside the simulation domain.

3.3 Results

We performed simulations with azimuthal extents of 45, 90, 180 and 360 degrees to determine a minimum azimuthal range on which similar behaviour as in a complete 360 degree disk can be expected. The low resolution chosen for all simulations enables simulation times close to 1000 orbits (which for $H/R = 0.05$ needs 16 times the computation cost) enables us to determine the lifetime of the formed vortices and possible influences on disk evolution an planetesimal formation. The simulation parameters are summarized in Table 3.1. In this section, we present the results of our simulations, focusing first on the flow properties and later on vorticity.

3.3.1 Transport properties

We analyse the transport properties of the VSI for all runs in a subdomain of the simulation grid. The subdomain is defined as $R = [0.7 - 1.8]$, $Z = [\pm 2.5H]$, $\phi = [0, \phi_{\mathrm{max}}]$. This is done to avoid possible influence of the imposed boundary conditions on the results.

We look at the Reynolds stresses generated in the disk following the prescription by Klahr & Bodenheimer (2003)

$$T_{r,\phi} = \langle \rho v_r v_\phi \rangle_{\phi,t} - \langle \rho v_r \rangle_{\phi,t} \langle v_\phi \rangle_{\phi,t} \tag{3.6}$$

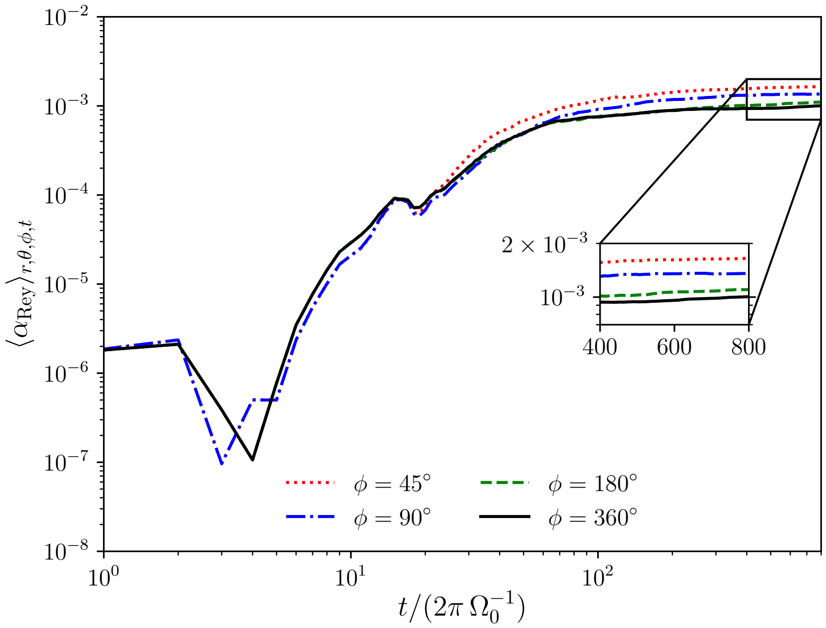

Figure 3.1: Evolution of the alpha values over the simulation time. The alpha values are averaged over the analysis domain an as running average in time. We observe the turbulence to saturate rapidly within around 100 orbits to alpha values of around 10^{-3}. The alpha values for the simulation with smaller azimuthal domain are slightly larger than for the larger domain. The inset highlights the evolution for the last 200 orbits.

and compute the α-parameter of the disk

$$\alpha_r(z) = \frac{\langle T_{r,\phi} \rangle_r}{\langle P \rangle_r} \tag{3.7}$$

with $P = \langle \rho c_{\mathrm{s}}^2 \rangle_{\phi,t}$. This guarantees a mass weighted α and filters out angular momentum flux associated with mean mass transport $\langle \rho v_r \rangle$. We plot the evolution of α over time in figure 3.1. The values are averaged over the whole analysis domain in each direction and up to the given point in time. We find α-values of approximately 10^{-3} in agreement with Stoll & Kley (2014) and (Nelson et al. 2013), but significantly higher than those reported by Richard et al. (2016). The equilibrium alpha values (table 3.1) can be seen to decrease with increasing azimuthal extent. This effect is caused by the use of periodic boundary conditions in phi direction, leading to a large pitch angle for the tightly wound spiral pattern for smaller phi extents.

To look at the vertical structure of the disk, figure 3.2 compares the meridional α profiles of the simulated disks averaged between 500 and 700 orbits and over the radial and azimuthal subdomain. We observe different profiles for each simulation. We find the steepest profile for the simulation p45, showing high alpha values at the disk surface and negative values at the midplane, which suggest moderate inward angular momentum transport in the midplane of the disk and outward transport in the surface layer. The profile flattens for the case p90, with positive alpha values throughout the disk and lower alpha values at the surface compared to run p45. This trend continues for the cases p180 and p360, though the latter show to be in good

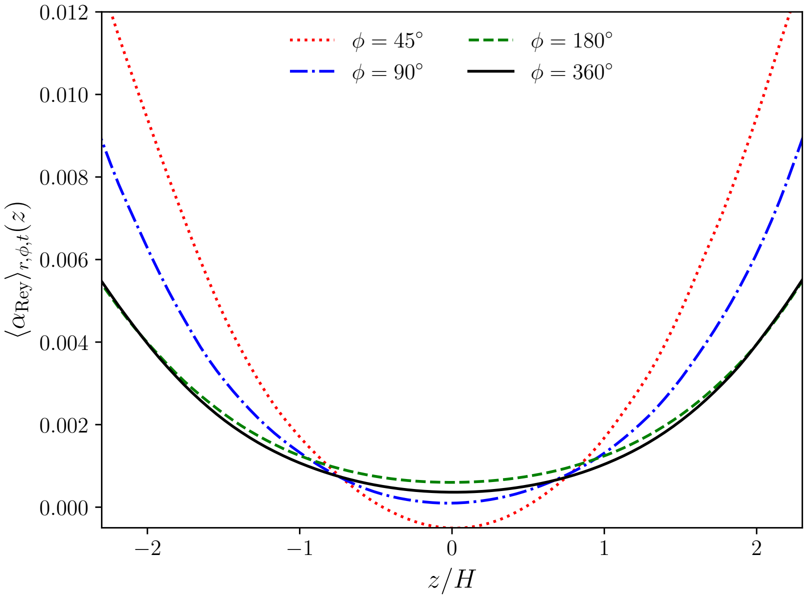

Figure 3.2: Meridional profile of the alpha value. The alpha values are averaged over the radial and azimuthal subdomain and 500-700 orbits. We observe a steeper meridional profile and negative midplane alpha values for the simulations with small azimuthal extent. The profile for the simulations with large azimuthal extent show strictly positive alpha values.

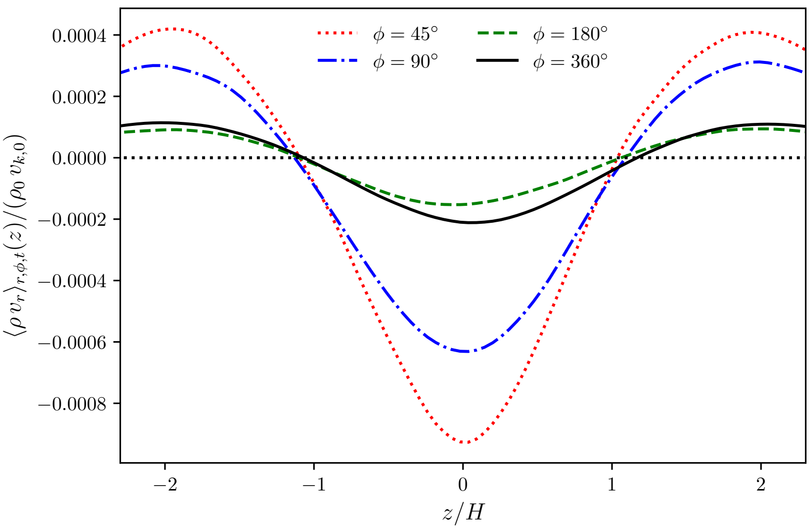

Figure 3.3: Vertical profile of the radial mass flow. We find inward mass flow in the midplane of the disk for all simulations.

agreement with each other. This also suggest angular momentum is transported outward at all heights, albeit with stronger transport in the upper layers of the disk. The vertical profile of the Reynolds-stresses of the disk shows the largest angular momentum transport to occur at $z \approx \pm 1.6H$ for simulation p45 and decreasing to $z \approx \pm 1.3H$ for the full 2π disk.

To investigate this behaviour further, we calculate the radial mass flow of the disk $\rho\, v_r$ as a function of height above the midplane in all our simulations, shown in figure 3.3. We again average over the radial and azimuthal domain of the simulation and over 200 snapshots taken between 500 and 700 local orbits. We find radial mass inflow for all models in the midplane, which aligns with the findings of Stoll et al. (2017), who find the same flow reversal applying an anisotropic viscosity model with a heightened z-viscosity component. Therefore, although there is only small to no outward radial angular momentum transport present in the midplane from the VSI, mass can be accreted efficiently. The angular momentum however is transported vertically from the midplane to the upper layers of the disk, where it is then transported radially outward. This mechanism also gives an explanation to the observed shallower vertical profiles for the models p180 and p360. We argue that due to the large azimuthal extent of the disk, the anisotropy manifests in different magnitudes and therefore leads to an overall shallower profile. This supports our view that treating the disk as too high m leads to incomplete results.

To prove that the vertically averaged angular momentum transport (i.e. our measured mean α-value) is nevertheless sufficient to prescribe the mean radial mass-accretion, we calculate the average radial velocity given from steady-state viscous accretion theory and compare this to the simulation values. Integrating the vertically-averaged steady-state angular momentum equation one obtains

$$\Sigma v_R = \Sigma \nu \frac{\mathrm{d}\Omega}{\mathrm{d}R} = -\frac{3}{2}\alpha \left(\frac{H}{R}\right)^2 \Sigma v_{\mathrm{k}} \tag{3.8}$$

with Σ the disk column density, $\nu = \alpha H^2 \Omega$ the viscosity and $\mathrm{d}\Omega/\mathrm{d}R = -3/2\Omega$. For the case p360 with $\alpha = 10^{-3}$ we get $\Sigma v_R/(\Sigma v_k) = -1.5 \cdot 10^{-5}$. From the corresponding simulation run we get from integrating over figure 3.3 an average value of $\Sigma v_R/(\Sigma v_k) = -2.4 \cdot 10^{-5}$, which agrees well to the predicted value. This shows that angular momentum transport driven by VSI is well described in the picture of α-viscosity, even if transport is most likely realised by travelling spiral waves rather than local Kolmogorov-like 3D turbulence. This also supports our claim that angular momentum is transported mainly vertically from the midplane to higher layers and then transported outward, as the vertically averaged angular momentum matches the value needed for the occurring mass transport despite the low α values measured in the midplane of the disk. Whether the turbulence is truly local, i.e. the dissipation of kinetic occurs also proportional to the measured α-viscosity, was not possible to be determined in our simulations, but should be goal for future setups. This would need the monitoring of local heating and cooling.

We also look at the time evolution of the rms-velocities in the disk, defined as

$$v_{\mathrm{rms}} = \left(\frac{1}{V}\int_V (v_R^2 + v_Z^2) dV\right)^{0.5} \quad . \tag{3.9}$$

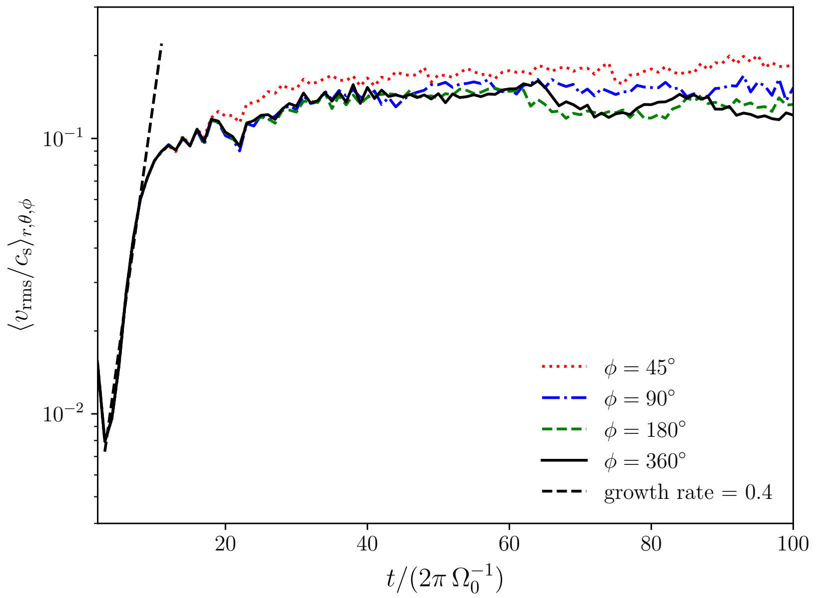

Figure 3.4: Time evolution of the RMS-velocity of the gas. The values are averaged over the radial and azimuthal subdomain. We observe rapid turbulent growth at the onset of the simulation and saturation after a few 10 orbits. We fit the exponential growth rate of the velocity as 0.4 per orbit.

We consider only the radial and vertical component of velocity because the disk rotation profile is not keplerian in this chapter and spatially varying systematic deviations cannot be taken into account. The results are presented in figure 3.4. We find the values of all runs to agree with each other for the first few orbits as expected, as the limit in azimuthal wavenumber does not influence the onset of the instability. The overall onset of the instability is observed earlier than in other studies. This is explained by the specific choice of parameters in our setup, which allows for earlier onset of the instability due to the very short cooling time. The saturated values for cases missing the lower azimuthal wave-numbers p45 and p90 are higher than for the other cases. We measure the growth rate of the velocity perturbations as 0.4 per orbit, about double the value reported by Stoll & Kley (2014), which is in excellent agreement with theory as growth rate is proportional to the pressure scale height $\sigma \sim q\Omega\frac{H}{R}$ (Nelson et al. 2013), which was only half the value we adopted. Note that Stoll & Kley (2014) give their value for the growth rates for the kinetic energy. Comparing the time evolution of the rms-velocity to the time evolution of the alpha value in figure 3.1, we find that the rms-velocity saturates after about 20 orbital periods, while α, the quantity related to angular momentum transport, saturates only after 100 orbital period. This behaviour is linked to the transport of energy to larger scales in the disk and we will discuss this further in section 3.4.1.

Figure 3.5 shows the $v_{\rm rms}$-values as a function of height averaged over the radial and azimuthal subdomain and between 500 and 700 orbits. We find a similar shape for the vertical structure of all runs with low velocities in the midplane and rising with z/H. We find a systematic positive offset for all runs compared to p360 with p45 having the largest offset. This compares to our findings for the α viscosity parameter in figure 3.2, suggesting a smaller $\phi_{\rm max}$ systematically overestimates the

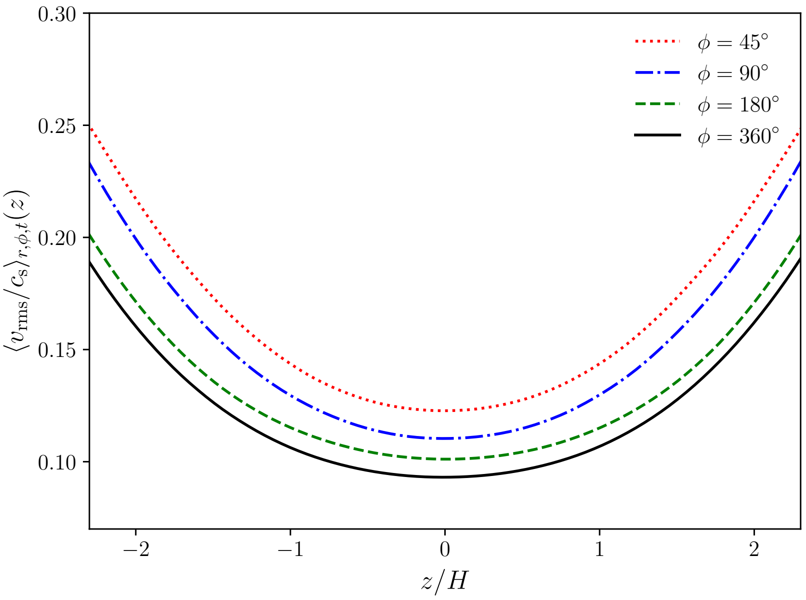

Figure 3.5: Meridional profile of the RMS velocity. The vrms values are averaged over the radial and azimuthal subdomain and between 500 and 700 orbits. We again observe significantly lower values for the run p360 than for the other runs.

turbulence strength.

In spectral line observations of protoplanetary disks the total rms velocity can however not be measured. The most easily accessible quantity is the vertical component of the velocity, which can be measured by determining the line broadening of face-on disks. We separately calculate the height profile for this quantity in figure 3.6. We again see the large offset for the simulations p45 and p90 compared to the case p360, the case p180 shows similar values to the 360° case. The height profile for all simulations follows a similar shape as the total v_{rms} values with low values in the midplane growing with height z.

Cuzzi et al. (2001) related the rms-velocity to the turbulent viscosity parameter α via

$$v_{\mathrm{rms}} = \sqrt{\alpha} c_{\mathrm{s}} \tag{3.10}$$

(their equation 2) if the largest eddies have a rotation frequency comparable to the orbital frequency. To check the applicability of this relation to the turbulence induced by the VSI, we plot the ratio of the height dependent z component of the rms-velocity to the square-root of the simulation averaged alpha value (see table 3.1) in figure 3.7. For all simulations, the ratio of $v_{\mathrm{rms}}/c_{\mathrm{s}}$ to $\sqrt{\alpha}$ is above unity. Therefore the angular momentum transport in our simulations of the VSI is weaker than one would expect from the measured velocities. The deviation depends on height with values closer to unity in the midplane. The overall deviation is largest again for the case p45, which also showed the highest values for $v_{\mathrm{rms}}/c_{\mathrm{s}}$ and α and decreases with ϕ_{max}. For the case of a full disk we find however values larger than for $\phi_{\mathrm{max}} = 180°$. For protoplanetary disks subject to the VSI, the α values calculated from measured turbulent velocities should therefore be treated with caution. Depending on the height above the midplane where the measurement is taken, the values for α could

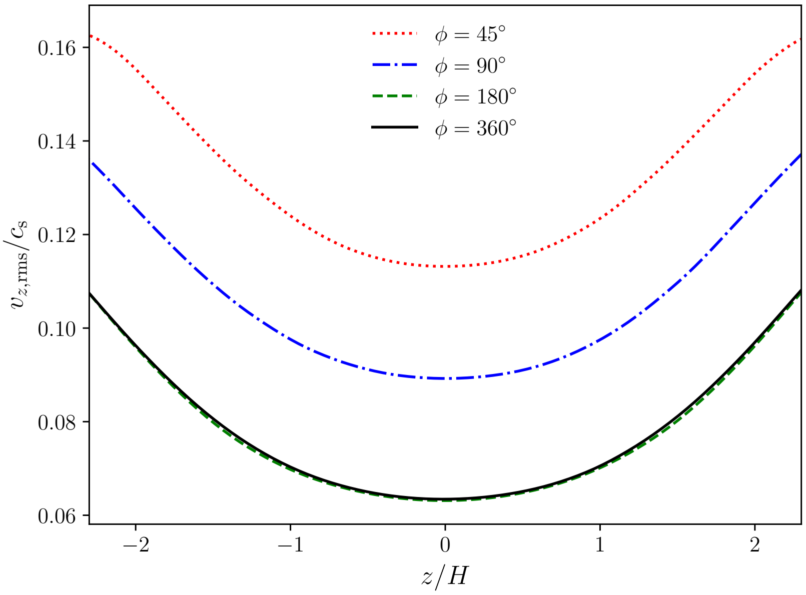

Figure 3.6: Vertical profile of the vertical rms velocity. We average the values over the radial and azimuthal subdomain and between 500 and 700 orbits. We find a large offset for the cases p45 and p90 compared to p180 and p360, which are in good agreement with each other.

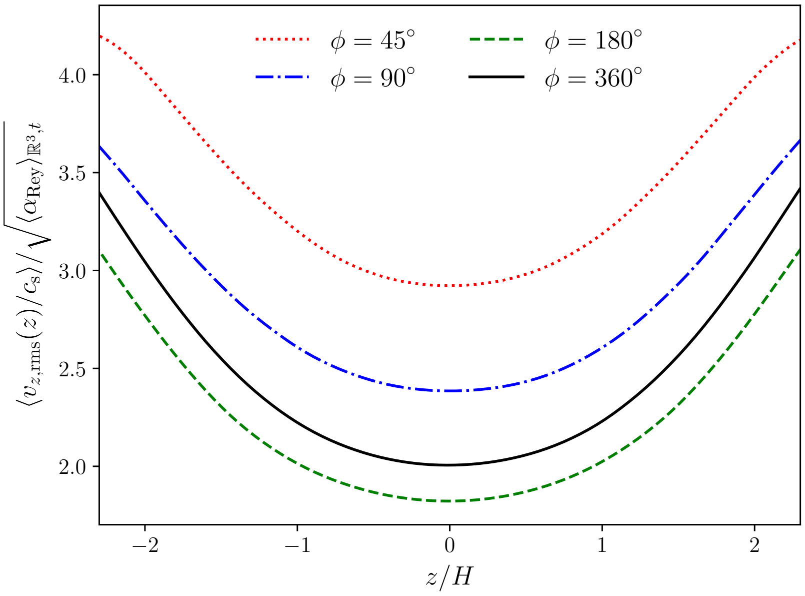

Figure 3.7: Vertical profile of the vertical rms velocity divided by the square root of the total alpha value of the disk (see table 3.1). We average the values over the radial and azimuthal subdomain and between 500 and 700 orbits. All simulations show an offset from unity, so estimating the α-values from $v_{z,\mathrm{rms}}$ leads to an overestimation. We again find a large positive offset for the cases p45 and p90 compared to p360, whereas p180 has a smaller negative offset with respect to p360.

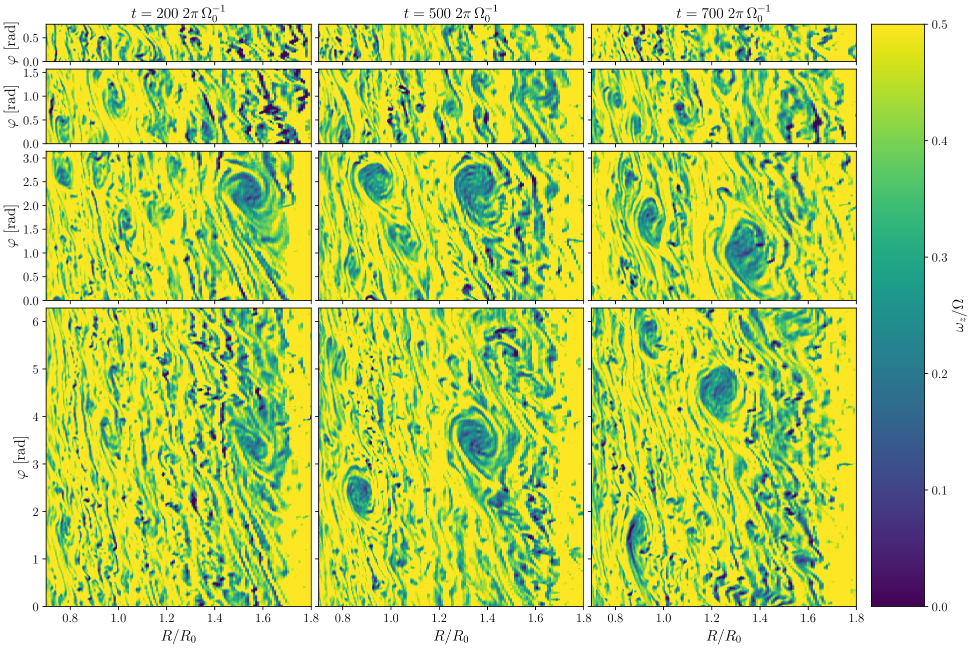

Figure 3.8: The midplane value of the z-component of vorticity after 200, 500 and 700 local orbits into the simulation. The azimuthal size of the simulation increases from top to bottom. For the upper two rows we see the formation of zonal flows and small vortex structures. In contrast to this we see large vortices in the lower rows for the second and third snapshot.

be overestimated by up to one order of magnitude. Also, when comparing the alpha values of simulations and observations, the influence of the azimuthal extent of the simulation should be taken into account.

3.3.2 The influence of ϕ_{max} on the disk structure

To asses the influence of ϕ_{max} on the outcome of the numerical simulation, we plot the z component of the vorticity

$$\omega_z = (\boldsymbol{\nabla} \times \boldsymbol{v})_z \tag{3.11}$$

in the disk midplane for three different times: after 200, 500 and 700 local orbits. The results are presented in figure 3.8. For the case of p45, we find small vortices with aspect ratios $\chi \approx 4$ and zonal flows. All structures show strong variations in time, as can be seen by the differences in the time frames shown in figure 3.8. These structures also appear in the case of p90, where also larger structures similar to vortices emerge in the first frame but are destroyed again in the second frame of figure 3.8, also pointing to high variability with time. This changes for the simulations p180 and p360. Here we observe small, unstable vortices forming quickly in the beginning and additionally two larger vortices with aspect ratios $\chi \approx 8 - 10$ after a few hundred orbits, seen in the left frame in figure 3.8. The large vortices continue to

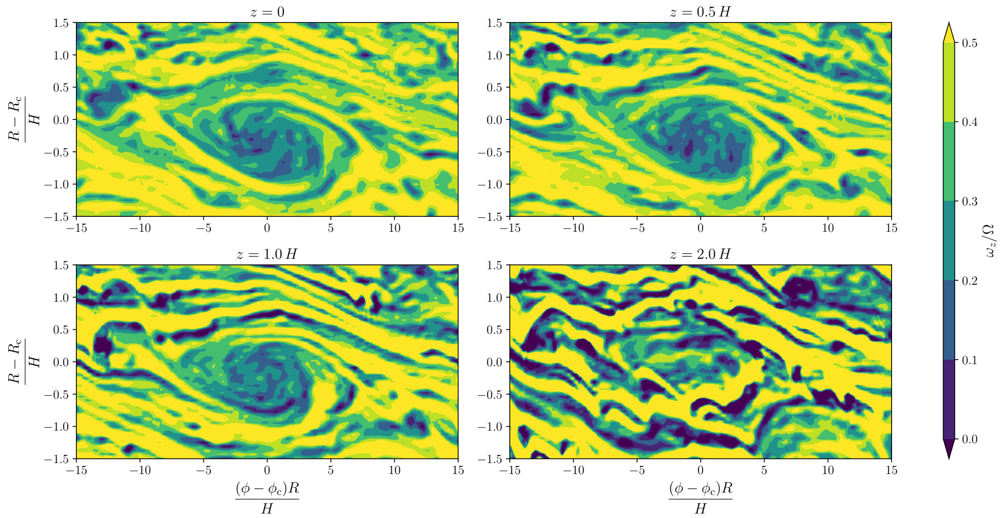

Figure 3.9: Contour plots of the vorticity at different heights above the midplane for the simulation p360 at the position of the outer vortex $(R_\mathrm{c}, \phi_\mathrm{c}) = (1.4\,R_0, 3.5)$ after 500 orbits. The plots show the highly turbulent state in the vortex.

appear both after 500 and 700 orbits (fig. 3.8, middle and right columns), suggesting stability over larger times. The middle and right column also show additional large vortices appearing at later times. This change in overall structure for azimuthal extents larger than 180° suggests that the approximation of large m restricts the development of large, long lived structures in VSI disks.

Looking at the large vortices specifically, we find them to have an inner turbulent structure, similar to the one found in (Raettig et al. 2013; Lyra 2014). Figure 3.9 illustrates this, showing the structures inside the outer vortex of the simulation p360 at $(R_\mathrm{c}, \phi_\mathrm{c}) = (1.4\,R_0, 3.5)$ after 500 orbits (fig. 3.8, middle column). We again plot the z component of vorticity, now for 4 different heights z = 0, 0.5 H, 1 H and 2 H above the midplane of the disk. We multiply the azimuth with the central radius and scale both axis with the local pressure scale height to show the true size of the vortex.

The structure inside the vortex shows changes on small scales, forming a highly turbulent substructure. The turbulent structure is visible throughout the upper and the lower left panel of figure 3.9. In these 3 panels we also find a consistent outer boundary for the vortex as an azimuthally elongated radially narrow region of higher vorticity relative to the inside of the vortex, forming a shell around the vortex. This structure is consistent with the predictions of Lesur & Papaloizou (2009) for the elliptic instability, which we will discuss in section 3.4.2. The lower right panel of figure 3.9 shows the vortex structure fading into the turbulent background structure of the disk, suggesting the vortex extends to about 2 scale heights above and below the midplane.

To asses the influence of the forming vortices on the flow structure reported for the VSI we plot the vertical velocity times density in the R-Z plane in figure 3.10 after 500 orbits, corresponding to the middle column of figure 3.8. Figure 3.10 (b) and (c) show the models p45 and p90 at $\varphi = \pi/8$ and $\varphi = \pi/4$ respectively and (d)

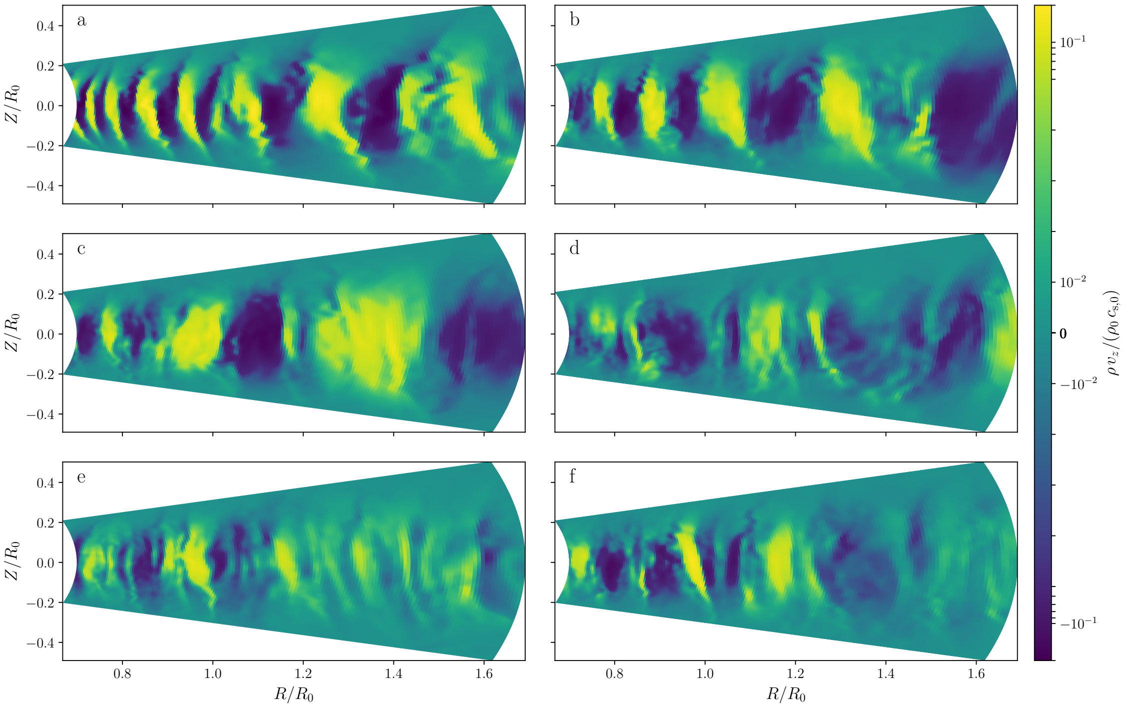

Figure 3.10: Vertical slice of the vertical velocity in the disk for different azimuthal positions after 500 orbital periods. Plot (a) shows a 2D axisymmetric disk after 80 orbits for comparison, (b)-(d) the models p45, p90 and p180 respectively and (e) and (f) the model p360, where (e) is taken at a φ position without a vortex and (f) at the center of the outer vortex shown in figure 3.8 (middle column). The color scale uses linear scaling for absolute values smaller 0.05 and logarithmic otherwise to enhance visibility.

shows the model p180 at $\varphi = 2.5$, the center position of both vortices at that time. Figure 3.10 (e) and (f) show model p360 at 2 different φ positions: (e) at $\varphi = 1.0$, where no large vortices are intersected, and (f) at $\varphi = 3.6$, the center position of the outer vortex. Figure 3.10 (a) shows the 2D axisymmetric simulation with the same r,z resolution from the resolution study shown in appendix A after 80 orbits. The snapshot from the 2D run is taken at an earlier time to avoid the non-linear phase of the axisymmetric VSI, which differs from the full 3D simulations due to the occurrence of the RWI in 3D.

We find a similar vertical velocity profile as reported by Nelson et al. (2013),Stoll & Kley (2014) and Flock et al. (2017b) with strong vertical motions present over the whole height of the disk. We find the run p45 agreeing well with the early stage of the 2D comparison simulation, showing a pattern of disk annuli of $\Delta R \approx 0.5H$ with alternating positive and negative vertical velocity and symmetry about the midplane of the disk. In (c) we see the overall pattern still preserved for the case p90, but the annuli now have a larger radial width of $\Delta R \approx H$. This picture changes once the disk is able to form vortices. Fig. (d) shows the case of p180 at the centre position of the inner vortex. The ordered pattern seen in (a)-(c) is broken at the radii of the vortices, although it is still partly visible at other radii. The size of the annuli of alternating velocity also decreases in this simulation. Both vortices have negative vertical velocities, although the velocity is greatly reduced

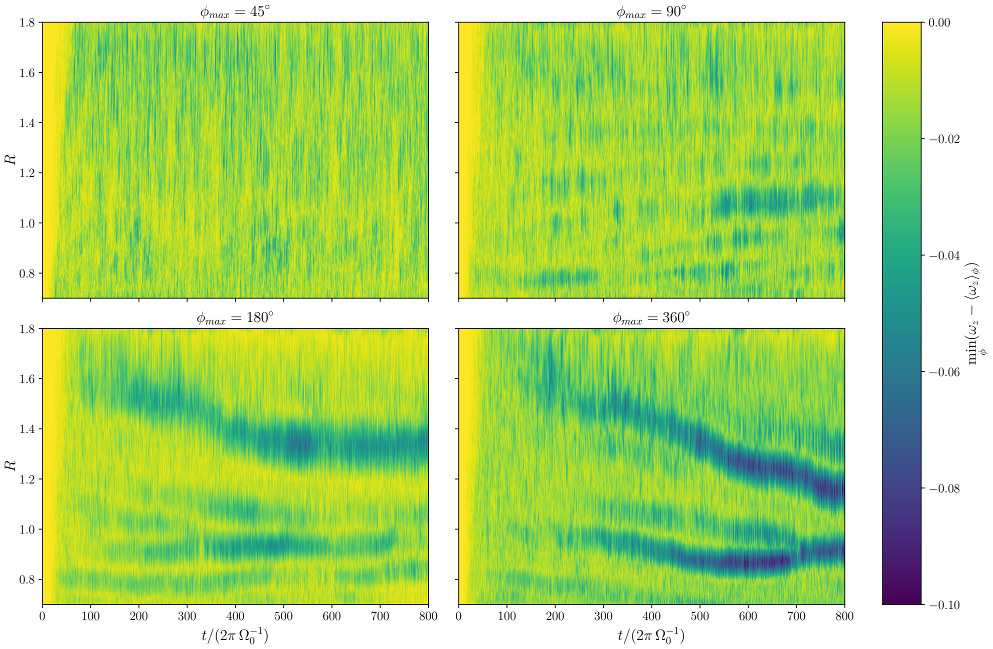

Figure 3.11: Track of the vortex radial position over time via a function of ω_z. Only the cases p180 and p360 in the lower panels show vortices surviving over hundreds of orbits, indicated by the darker lines. The lower panels also show the position of the vortex moving to smaller radii with time.

with respect to the surrounding, especially for the outer vortex. Figure (f) shows a similar behaviour for the case p360. The overall structure of the disk is less ordered than for the axisymmetric case and the vortex has a lower vertical velocity as the surrounding disk, although a similarity with the VSI velocity pattern is retained. This is also true for slices at φ positions outside the vortex, shown in (e). There we also find the pattern of positive and negative v_z annuli, although their strength and width again is diminished with respect to the axisymmetric case. Interestingly, we also find a turbulent ring structure at the raidal position of the outer vortex in (e). This could indicate the vortex is embedded in a larger flow structure or the occurrence of small vortices which are elongated in z-direction. Comparing (e) and (f) in the inner part of the disk, we find the radial positions of the annuli described above do not coincide, indicating the annuli are not axisymmetric anymore for these larger disks.

3.3.3 Vortex lifetime

For planetesimal formation the lifetime of a vortex is a critical factor determining the trapping efficiency. Therefore we are interested in the lifetime of the vortices generated by the instability. A distinctive signature of a large anticylonic vortex is a minimum in local vorticity stretching out over a fraction of a disk annulus. We therefore apply a box filter in radial and azimuthal direction to the midplane z-vorticity values. In azimuth, we apply a filter width of 48 and 96 grid cells for p45 and p90 respectively and 200 grid cells for both p180 and p360. In radial direction, the filter width is 30 grid cells, equalling $2H$. The filter damps fluctuations on scales smaller than the filter width, enhancing the visibility of large scale structures. To outline the radial position of the large vortices, we then find the minimum in the deviation of the smoothed ω_z from the azimuthal average in the respective annulus. The calculation of the deviation from the azimuth ensures we exclude the large azimuthal flow structure occurring at the outer boundary in figure 3.8. Figure 3.11 shows the evolution of this value as a function of radius and time, outlining the radial position of the vortices in the disk over the run of the simulation.

We observe multiple long living vortices emerging in run p180 and two in run p360, seen in the lower panel in figure 3.11. They start with distances of 1 to 5 pressure scale heights and are observed to migrate inwards with a migration rate lower than 0.0005 R_0/Ω. Paardekooper et al. (2010) find similar migration rates for vortices in laminar 2D vertically integrated disks. Though their results are not directly transferable to the case presented here, we think the underlying mechanism is the most plausible explanation of the phenomenon observed. The outward migration of the inner vortex in p360 can be explained by the occurrence of a surface density maximum moving outward. The vortex is trapped in the maximum and is dragged outward again, as it cannot drift across it (Paardekooper et al. 2010). Figure 3.11 in conjunction with fig.3.8 also shows vortices interacting and after some time merging once one vortex migrates within one pressure scale height radial distance to another.

In contrast, we don't observe the same in the simulations p45 and p90, shown in the upper row of figure 3.11. We do not see any sign of larger vortices in simulation p45, which is in agreement with (Richard et al. 2016). The case p90 shows a vortex forming after around 150 and another after 550 and existing at least intermittently. This suggests the phi range of a simulation to be crucial in the development and sustaining of large, long lived vortices.

3.4 Discussion

3.4.1 RWI as secondary Instability

In this section, we now focus on evidence in our simulations that suggests the triggering of the Rossby-Wave-Instability (RWI) to initiate vortices. We therefore calculate the values of the critical function $\mathscr{L}$ as given in equation 2.45 from an azimuthally averaged density, pressure and velocity structure of our simulation. We also averaged the field quantities over θ before calculating $\mathscr{L}$.

Figure 3.12 shows $\mathscr{L}/\mathscr{L}_0$ as a function of radius after 200, 500 and 700 orbits. In the top row we show the results from p45. All plots show multiple strong global maxima, suggesting the disk to be in principle susceptible to the RWI. The amplitude of the extrema decreases with time but they stay as distinctive features throughout the simulation time. In the bottom row we show $\mathscr{L}/\mathscr{L}_0$ for p360. Here we also find extrema, but fewer in number and not as distinct as for p45. Also, the overall amplitude of the extrema is lower as in the other case.

Taking a closer look at the lower right plot in figure 3.12, we find the most distinctive peaks at R=1.0,1.3 and 1.45. Comparing these to the initial locations of the vortices we find in the lower left subplot of figure 3.11, we find them to be in

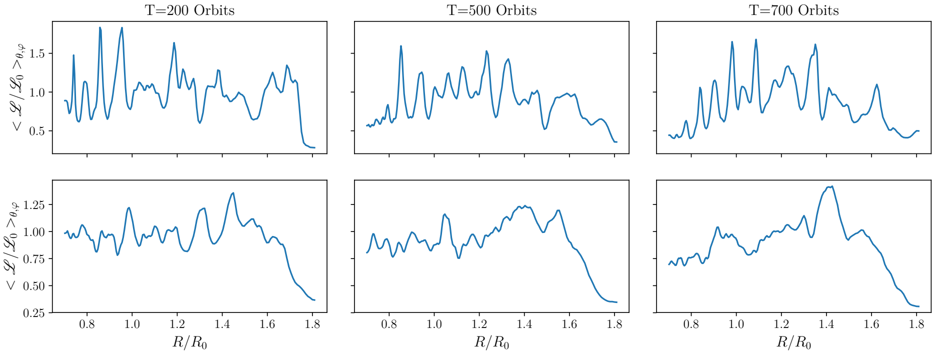

Figure 3.12: The critical function $\mathscr{L}$ of the RWI for 3 different times normalized by the initial profile. The upper row represents the run p45 and the lower represents run p360.

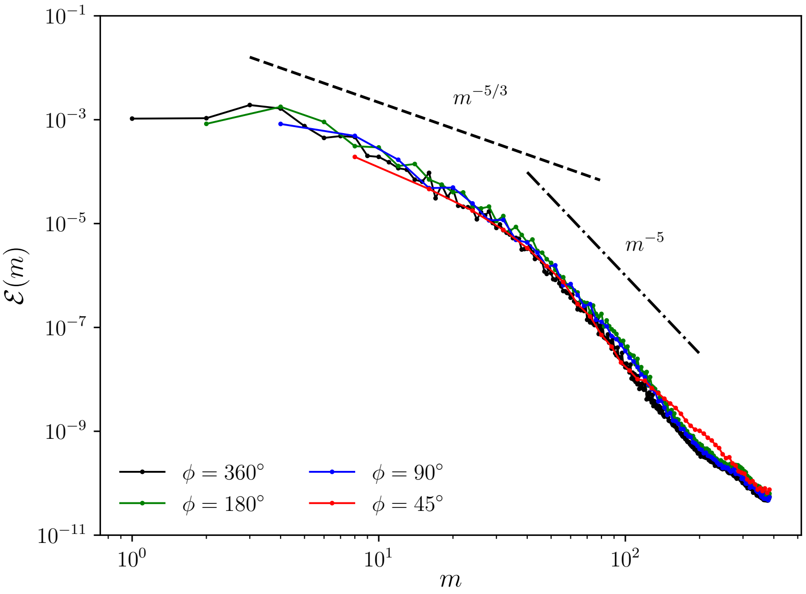

Figure 3.13: Kinetic energy spectrum at 700 orbits. Note the distinctive broken power law behaviour characteristic for 2D turbulent fluid flow with both inverse energy and downward enstrophy cascade. For comparison we plot the power laws $\mathcal{E}(m) \propto m^{-5/3}$ and $\mathcal{E}(m) \propto m^{-5}$, indicators of the inverse energy and downward enstropy cascade respectively.

good agreement. This is clear evidence that the RWI is triggering the large vortices we observe in our simulations. The decrease in amplitude of the extrema after saturation of the instability has been shown for artificial RWI vortices by (Meheut et al. 2010) and can explain the decrease we witness in the p360 case.

To investigate this, we also look at the azimuth of the kinetic energy spectrum in the midplane of the disk.

$$\mathcal{E}(m) = 0.5 \sum_i \langle |(\mathcal{F}(v_{i,z=0}))^2| \rangle_r \qquad i \in [r, \theta, \phi] \tag{3.12}$$

$\mathcal{F}$ denotes the Fourier transform of the respective velocity component.

(Li et al. 2000) showed the RWI has a maximum growth rate for the azimuthal wave number m in the range of $m = 3-6$. These wavenumbers can only be accessed for simulations with an azimuthal extent equal or larger than 90 degree. Therefore the RWI is expected to only grow inefficiently in the p45 simulation. Figure 3.13 shows the radial average of the azimuthal component of the kinetic energy spectrum after 700 orbits.

We find a broken power law for $\mathcal{E}(m)$ in all our simulations. At smaller wavenumbers m, the slope falls as $m^{-\frac{5}{3}}$, as expected for the upward Kolmogorov cascade in a rotationally dominated flow above the Rhines scale (Rhines 1975), i.e. where the eddy turn over time is longer than the rotational period of the system. At large wavenumbers, the spectrum behaves $\propto m^{-5}$, a scaling in agreement with a 2D enstrophy downward cascade. This result indicates that our simulations are predominantly 2D/rotation dominated due to the fast rotating flow in the disk. This is supported by our finding that the Reynolds stresses saturate at a later time than the rms-velocity. The rms-velocity directly traces the turbulence generated at smaller scales induced by the VSI, but α_{Rey} traces the angular momentum transported at larger scales. The difference in saturation time is then explained with the observed inverse energy cascade in the disk, which has to transport the energy generated at small scales to the larger scales on which angular momentum is transported in the disk. This is supported by the fact that we find from figure 3.13 that the energy injection of the VSI occurs at about $m = 40 - 60$, which is about $1 - 1.5$ pressure scale heights.

At the smallest wavenumbers m, we find a maximum for $\mathcal{E}(m)$ at $m = 3$ and $m = 4$ for the cases with $\phi_{\max} = 180^\circ$ and 360°, whereas for the other cases the energy piles up at $m = 4$ and $m = 8$ for $\phi_{\max} = 90^\circ$ and 45°, the largest respective wavenumber accessible. For the cases with $\phi_{\max} \leq 180^\circ$, the large vortices formed by the RWI extract energy from the flow, whereas the absence of large vortices in the other simulations forces the energy to be deposited in the largest mode accessible in the simulation. This can also explain the systematically higher rms-velocities we found for $\phi_{\max} = 45^\circ$ and 90° in figures 3.4 and 3.5.

To confirm we are in the rotation dominated regime in our simulations, we plot the Rossby number

$$\mathrm{Ro} = \frac{u}{l \cdot \Omega_0} \tag{3.13}$$

with u being the flow velocity at length scale l. The Rossby number gives the relative importance of Coriolis forces vs. inertial forces and is smaller unity if Coriolis forces are non-negligible for the flow in the system. We can express this number also as a function of wavenumber m using the kinetic energy spectrum to define the velocity spectrum.

$$\mathrm{Ro}(m) = \frac{\sqrt{m/(2\pi\, R_0)\mathcal{E}(m)}}{m/(2\pi\, R_0) \cdot \Omega_0} \tag{3.14}$$

We plot $\mathrm{Ro}(m)$ as a function of azimuthal wavenumber m in figure 3.14. We find the Rossby number stays below unity at all scales accessible in our simulations, confirming we are indeed rotationally dominated. We also find $\mathrm{Ro} \approx$ const. at the largest wave numbers m, indicating a change of slope for $\mathcal{E}$ not prominently visible in figure 3.13. Of course we only investigate one component of the turbulent spectrum,

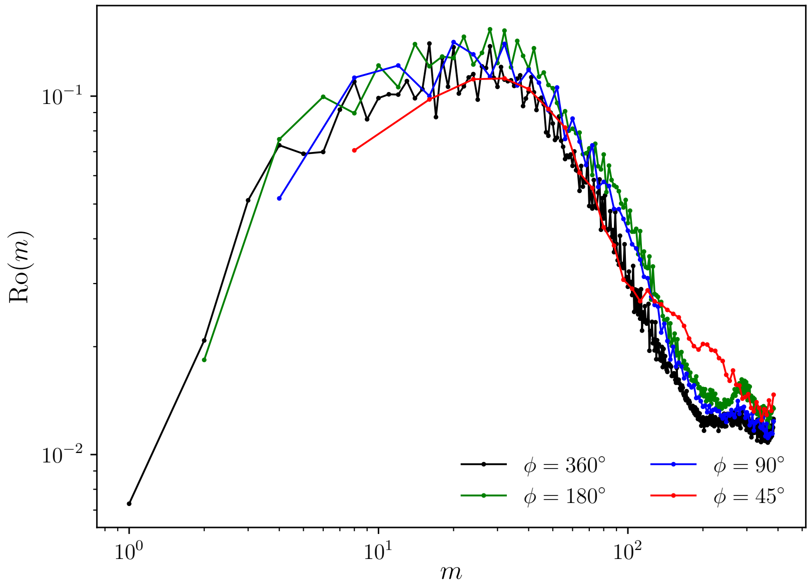

Figure 3.14: Rossby number as a function of azimuthal wavelength at 700 orbits. We find Ro to rise at large scale and later fall towards larger scales, with a maximum at the energy injection scale. The Rossby number stays below unity at all scales resolved in our simulation.

because neither the radial nor the vertical wave numbers are as easy measurable as the azimuthal component. VSI is known to favour high radial and low vertical wave-numbers, yet this investigation was not feasible with the current data sets, but shall be attempted in the future. In any case the low values for Ro are an indication that all our turbulence is strongly rotational dominated and thus most likely not isotropic anyway.

Because Ro < 1 in our simulation, we now revisit equation 3.10 . Cuzzi et al. (2001) developed the equations under the assumption that the disk turbulence is isotropic and follows a Kolmogorov dissipation law, which implies that turbulence has to be in the Ro > 1 regime, which is clearly not the case here. From equation 3.13 we can estimate the wavenumber at which our system should satisfy this condition. For a typical velocity $v_{\rm rms} = 0.01 v_{\rm k,0}$ we get

$$m_{\rm Ro=1} = \frac{v_{\rm rms} \cdot m}{2\pi \, R_0} \approx 600 \frac{1}{R_0} \,, \tag{3.15}$$

a value much larger than the Nyquist-wavenumber of our setup. This suggests that the rms-velocities in the disk act on much larger scales than the turbulence scales, and the ansatz presented in Cuzzi et al. (2001) is not always valid in protoplanetary disks. We however consider only the azimuthal direction in our analysis, leaving the possibility of a different scaling in the other spatial directions. Nevertheless, even if there might be more energy at large radial and vertical wavenumbers $k_R, k_z \equiv 600/R$, this still means that turbulence is also on small scales highly anisotropic, asking for revisiting the Kolomogorov picture for small scale turbulence in protoplanetary disks. Also, the results of section 5.3 show the ansatz works quite well despite $v_{\rm rms}$ being generated on different scales than assumed for the turbulent α.

3.4.2 Influence of elliptic instability

In section 5.3 we described a turbulent substructure occurring inside the large vortices in our simulation runs p180 and p360. Lesur & Papaloizou (2009) showed a similar effect for vortices with aspect ratio $\chi > 8$ influenced by elliptic instability. The larger vortices in our simulations have aspect ratios $8 < \chi < 11$ and fit well with the predictions. We do not observe the predicted decay of these vortices by the elliptic instability, similar to the reports of Lesur & Papaloizou (2009). In how far this an effect of an inactive elliptic instability (EI), maybe suppressed by low resolution, or an overlap with the VSI is open for future investigations. At $\chi = 10$ the minimum growth time of the elliptic instability should be about 17.6 Orbits. But maybe the vortices receive additional driving from absorbing smaller vortices (as observed for Jupiter's Red Spot), which so far counteract destruction from the EI.

The occurrence of the EI also naturally explains the fast destruction of the small vortices we observe in all simulation runs. These vortices have $\chi < 4$ and are strongly influenced by the fast growing modes of the elliptic instability reported for this size regime.

3.5 Summary & Conclusions

We have performed full 3D hydrodynamical simulations of protoplanetary disks undergoing Vertical Shear Instability. We used four different azimuthal extents ranging between $\pi/2$ and 2π to asses the influence of non-axisymmetry on the development of the instability.

We summarize our main findings as follows:

- We find the Vertical Shear Instability to be capable of seeding vortices with large ($\chi > 8$) aspect ratios using the disk parameters $p = -\frac{2}{3}$, $q = -1$ and $\frac{H}{R} = 0.1$. This has to our knowledge not been reported for simulations of this instability. The vortices we observe are long lived (lifetimes larger than 500 local orbits) and can aid in the growth of planetesimals in protoplanetary disks via particle trapping as proposed by Barge & Sommeria (1995).

- We find the angular momentum transport in VSI to be sufficiently efficient and in agreement with latest assumptions for protoplanetary disks and constraints on planetesimal formation therein (Drążkowska & Alibert 2017). Interrestingly, despite most angular momentum is transported outward at large z, the radial mass flux is also outward at large z but inward close to the midplane. This is due to additional strong vertical transport of angular momentum in agreement with (Stoll et al. 2017). This leads to transport of angular momentum away from the midplane into upper layers, where it is then transported outwards.

- As a direct consequence, depending on the height z above the midplane, the ration of $v_{\mathrm{rms}}(z)$ to $\sqrt{\alpha}$ ranges between 2.0 and 3.5. This height depending ratio has to be taken into consideration when inferring disk α values from rms-velocity measurements.

- The choice of the size of the simulation domain, especially of $\phi_{\max}$ has a significant impact on the outcome of the simulation. We find for $\phi_{\max} < 90$ no indication for larger, long lived vortices forming. Furthermore we find a systematic increase of α-values and rms-velocities with decreasing $\phi_{\max}$.

Our findings for the VSI on smaller scales are therefore consistent with the results reported by Nelson et al. (2013),Stoll & Kley (2014, 2016),Richard et al. (2016) and Flock et al. (2017b) for the low azimuthal extent cases, while identifying their limitations on more global disk scales. We propose future work on instabilities in protoplanetary disks include global 360° simulations to identify possible low m effects suppressed in current simulations of disks sections.

Furthermore, we find resolution as an important factor, both for the development of the RWI and the EI in global disk simulations. We suggest the lower radial resolution used in Stoll & Kley (2014) as a possibility why they did not find vortex formation in their work. Although they use different parameters in their work ($p = -1.5$, $q = -1$ and $\frac{H}{R} = 0.05$), we do not find significant differences to their work in preliminary results of a parameter study we conduct. The results of this study will be the subject of a follow up publication. We also propose further high resolution simulations should be performed to investigate the influence of the EI on the longevity of the vortices generated.

3.A 2D resolution study

We performed a resolution study in 2D to confirm we resolve the instability in the radial and meridional direction. We conducted 3 runs with radial domain sizes of $N_r = 128$, 256 and 512 and $N_\theta = 128$ and 3 additional runs with $N_r = 256$ and $N_\theta = 64$, 128 and 256. In figures 3.15 and 3.16 we show the RMS-velocities for the initial growth phase.

We find convergence for radial domain sizes $N_r \geq 256$ and $N_\theta \geq 128$, proving the values we chose for the 3D simulations to be sufficient to capture the relevant physics in the early growth phases of our simulations. We also show the slope for a growth rate of $\Gamma = 0.42$ per orbit as a guidance value (black dashed curve). The growth rates found for the 2D simulations are in good agreement with the results presented above for the 3D case, supporting the validity of our choice of simulation domain parameters.

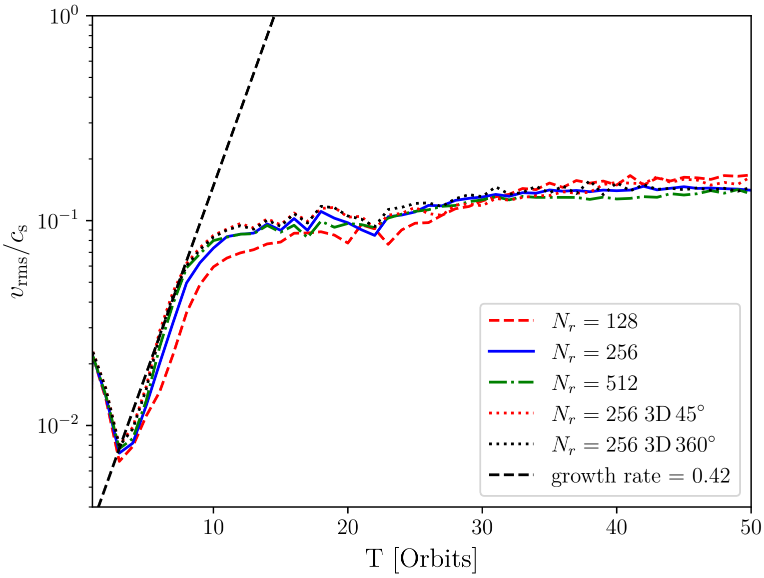

Figure 3.15: RMS velocities for the 2D resolution study in radial direction. We find convergence for the domain sizes above $N_r = 256$. For comparison, we also plot the values from the 3D model presented in figure 3.4.

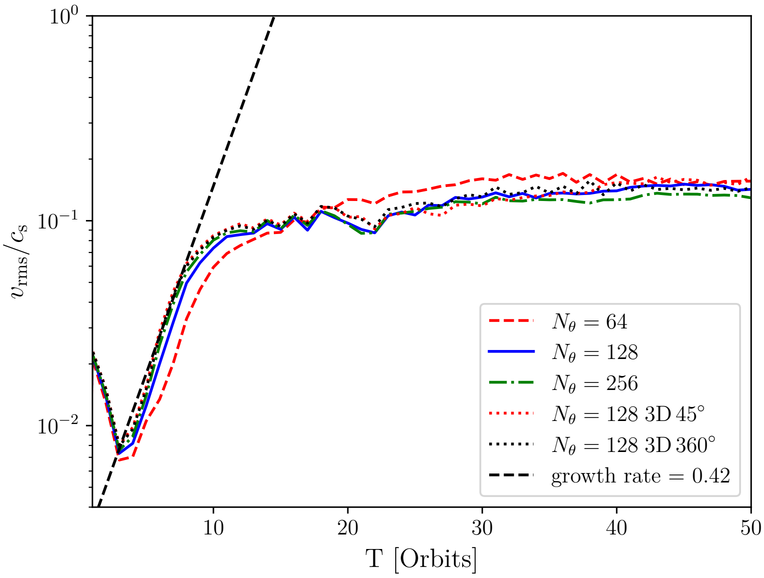

Figure 3.16: RMS velocities for the 2D resolution study in vertical direction. We find convergence for the domain sizes larger or equal $N_\theta = 128$. For comparison, we again also plot the values from the 3D model presented in figure 3.4.

Chapter 4

HIGH RESOLUTION PARAMETER STUDY OF THE VERTICAL SHEAR INSTABILITY

From Manger et. al. in preparation

4.1 Motivation

In chapter 3 we showed that the VSI is capable of seeding multiple large scale vortices. But we showed this only for one possible combination of disk parameters that could influence the instability. Therefore it is not possible to say if vortices always form once the VSI reaches its saturated nonlinear phase. In this chapter, I present the results of the first high resolution 3D parameter study conducted for protoplanetary disks with Vertical Shear Instability. With this study I want to investigate on one hand if the results obtained in resolution studies of 2D axisymmetric resolution studies are applicable in 3D, but also investigate if vortex formation is ubiquitous in disk with VSI and if this is the case, if and how the appearance of the vortices relates to the disk parameters. With this parameter study I also want to reconcile the differences observed in published simulations of the VSI by Stoll & Kley (2014) and my previous work presented in chapter 3. To make the simulations comparable, I choose the numerical setup to achieve a resolution of approximately 18 cells per scale height in all directions in all simulations.

The chapter is structured as follows: In section 4.2 I briefly describe the methods and initial conditions used in this study. In section 4.3 I present the simulation results and in section 4.4 I take a closer look at the vortices formed in the disk. Section 4.5 presents a resolution study in azimuthal direction. Finally, in section 4.6 I summarise the results and present conclusions for this chapter.

4.2 Model

In this chapter, we use a setup similar to the one used in chapter 3. The initial conditions are defined in force equilibrium, with the density defined as

$$\rho = \rho_0 \left(\frac{R}{R_0}\right)^p \exp\left(-\frac{Z^2}{2\,H^2}\right) \tag{4.1}$$

and the initial angular velocity of the disk given by

$$v_\phi = \Omega_\mathrm{K}\, R \left[1 + q - \frac{q\,R}{\sqrt{R^2 + Z^2}} + (p+q)\left(\frac{H}{R}\right)^2\right]^{\frac{1}{2}} \qquad . \tag{4.2}$$

We use an ideal equation of state $\rho e = \frac{P}{\gamma - 1}$ with the pressure defined as $P = c_\mathrm{s}^2 \rho$. Here, isothermal the sound speed $c_\mathrm{s}^2 = c_0^2 \left(\frac{R}{R_0}\right)^q$ is a function of radius, where we choose $q = -1$ in all our simulations. All other quantities used are defined in table 4.1. We again use a simple cooling prescription with

$$\frac{dP}{dt} = -\frac{P - \rho\, c_{\mathrm{s,init}}}{\tau_\mathrm{relax}} \tag{4.3}$$

where, to force the disk to be approximately isothermal, we define the relaxation time τ_relax equal to the simulation time step dt.

For our computations we use the multi-purpose MHD Godunov code PLUTO (Mignone et al. 2007) with a hllc solver (Toro 2009). We use the piecewise parabolic method (PPM) by Mignone (2014) for the spatial reconstruction and a 3rd-order Runge-Kutta time integration. All simulations performed are listed in table 4.2 with their parameters. We choose the grid sizes listed in column 3 of table 4.2 to ensure all simulations run share a common resolution of circa 18 cells per H in all directions.

We use periodic boundary conditions in azimuthal direction and modified outflow conditions in vertical direction, where we ensure zero inflow into the domain and additionally extrapolate the Gaussian density profile into the ghost zones. In radial direction, we use reflective boundaries combined with buffer zones, where we relax all variables to their initial values. These buffer zones are excluded in our analysis of the simulations.

4.3 Analysis of the Disk Gas Kinematics

In this section, we present the results of our parameter study on the influence of radial density gradient and disk aspect ratio on the vertical shear instability, focusing particularly on the angular momentum generating stresses and gas rms-velocities.

4.3.1 Stress-to-Pressure ratio

To measure the strenght of the VSI turbulence in the disk, we calculate the $T_{r,\phi}$ component of the viscous stress tensor

$$T_{r,\phi} = \langle \rho v_r v_\phi \rangle - \langle \rho v_r \rangle \langle v_\phi \rangle \tag{4.4}$$

which controls the amount of angular momentum transport generated by the disk turbulence. To present the values in a non-dimensional fashion, we normalise $T_{r,\phi}$ by the pressure to obtain α as defined by Shakura & Sunyaev (1973):

$$\alpha_r = \frac{T_{r,\phi}}{P} \qquad . \tag{4.5}$$

Symbol	Definition	Description
R, ϕ, Z		cylindrical coordinates
r, θ, φ		spherical coordinates
R_0, Z_0		cylindrical reference coordinates
ρ		density
ρ_0		reference density
H	$= \frac{c_s}{\Omega_K}$	disk pressure scale height
h	$= \frac{H}{R} = \frac{c_\mathrm{s}}{v_\mathrm{K}}$	disk geometric scale height
P	$= c_\mathrm{s}^2 \rho$	pressure
c_s	$= c_0 \left(\frac{R}{R_0}\right)^{q/2}$	isothermal sound speed
c_0	$= \frac{kT_0}{\mu m_H}$	reference sound speed
p	$= \frac{\mathrm{d}\log\rho}{\mathrm{d}\log R}$	radial density slope
q	$=\frac{\mathrm{d}\log T}{\mathrm{d}\log R} = -1$	radial temperature (sound speed) slope
e		specific internal energy
γ	$= 1.44$	adiabatic index
v_ϕ		azimuthal velocity
v_K	$= \sqrt{\frac{GM_\star}{R}}$	Kepler azimuthal velocity
Ω_K	$= v_K R^{-1}$	Kepler angular frequency
τ_relax		temperature relaxation time
$T_{r,\phi}$	eqn. 4.4	rϕ component of viscous Stress tensor
α	$= \frac{T_{r,\phi}}{P}$	turbulence parameter
v_rms	eqn. 4.6	root mean squared velocity
ω	$= \nabla \times \mathbf{v}$	vorticity

Table 4.1: List of all symbols used within this chapter.

model	domain size	grid size	p	h	$\langle\alpha\rangle/10^{-4}$
p0.6h0.1	$0.5 - 2.0 : \pm 3.5 : 0 - 2\pi$	256×128×1024	-0.66	0.1	8.4 ± 2.6
p1.5h0.1	$0.5 - 2.0 : \pm 3.5 : 0 - 2\pi$	256×128×1024	-1.5	0.1	9.5 ± 2.1
p1.5h0.07	$0.6 - 1.6 : \pm 3.5 : 0 - 2\pi$	256×128×1464	-1.5	0.07	2.7 ± 0.6
p0.6h0.05	$0.7 - 1.4 : \pm 3.5 : 0 - 2\pi$	256×128×2048	-0.66	0.05	1.5 ± 0.3
p1.5h0.05	$0.7 - 1.4 : \pm 3.5 : 0 - 2\pi$	256×128×2048	-1.5	0.05	1.2 ± 0.2
p1.5h0.03	$0.8 - 1.2 : \pm 3.5 : 0 - 2\pi$	256×128×3402	-1.5	0.03	0.5 ± 0.2

Table 4.2: List of simulation and model parameters. From left to right: model name, physical domain size in ($r_{\mathrm{in,out}}/R_0$: z/H : φ), numerical grid size in ($\mathrm{N_r} \times \mathrm{N}_\theta \times \mathrm{N}_\varphi$), density slope parameter, disk aspect ratio and space and time averaged stress to pressure value.

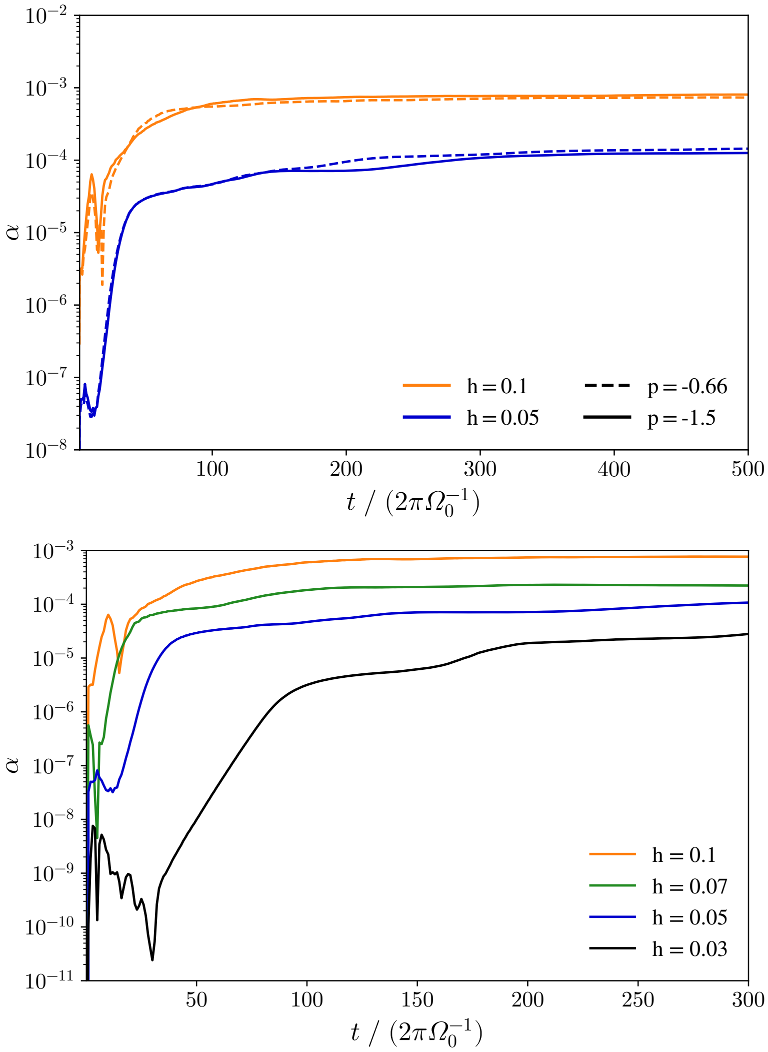

Figure 4.1: Cumulative space and time average of the stress-to-pressure ration for simulations with different density slopes p (top) and aspect ratios h at constant p=-1.5 (bottom).

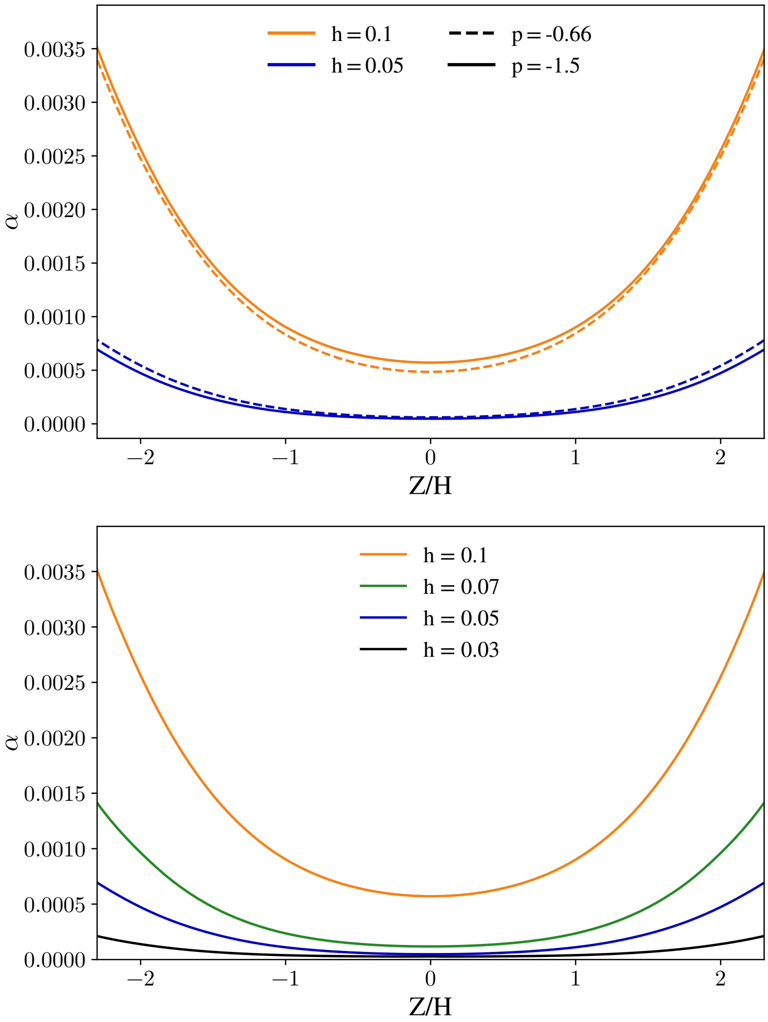

Figure 4.2: Stress-to-pressure ratio as a function of height. Top shows the dependence on the density slope p, bottom shows the dependence on disk aspect ratio h. The values are averaged in space and from 600-1000 orbits.

In figure 4.1 we present the cumulative space and time averaged values of α. The top panel of figure 4.1 compares simulations with two different density slopes $p = -0.66$ and $p = -1.5$ at two different values of the disk aspect ratio $h = 0.05$ and $h = 0.1$, whereas the bottom panel compares simulations with four different values of h and a constant value of $p = -1.5$.

The time evolution of the simulations with $h = 0.1$ shows a rapid growth of the α value in the first few tens of orbits of the simulation, after which a slower growth phase leads to growth to the final saturated phase of the turbulence after around 100 orbits, where values of $\alpha = 9{\cdot}10^{-4}$ are reached. These values are comparable the ones we reported for our simulations in chapter 3 for simulations with lower azimuthal but similar radial and meridional resolution. A similar behaviour is observed for the simulations with $h = 0.05$, which also show a first strong growth phase up to around 50 orbits, after which slower growth phase is observed until around 300 orbits, where a steady state value of $\alpha = 1 \cdot 10^{-4}$ is reached. This value is significantly smaller than the value reported by Stoll & Kley (2014), but still one order of magnitude larger than the values reported in Flock et al. (2017b).

Comparing all four simulation runs, we find that the density slope p does not significantly influence the average value of the turbulent stresses. The comparison however shows a clear correlation of the disk aspect ratio with the turbulent α values of the disk. This result has been expected, as the disk aspect ratio is proportional to the disk temperature and therefore a larger value of h leads to a larger overall temperature in the disk and to stronger turbulent velocities as visible in figure 4.3. We therefore ran additional simulations with aspect ratios $h = 0.07$ and $h = 0.03$, presented in the lower panel of figure 4.1 along the simulations discussed above. In comparing these four simulation, we see a clear trend with disk aspect ratio emerging: Simulations with larger h show overall stronger turbulent angular momentum transport, with $\alpha = 9 \cdot 10^{-4}$ for $h = 0.1$ going down to $5 \cdot 10^{-5}$ for $h = 0.03$. A full list of averaged saturated alpha values is listed in 4.2, where the errors listed are calculated for fluctuations in time only. The additional simulations also confirm the trend for later onset of turbulent growth and longer times until saturation. The occurrence of this trend is consistent with the results of Nelson et al. (2013), who observed this behaviour for the kinetic energy in their 2D axisymmetric simulations.

Figure 4.2 shows the dependence of α on height above the midplane, where the top panel again compares two different density slopes at $h = 0.05$ and $h = 0.1$ and the bottom panel. The values are averaged over the remaining dimensions and between 600 and 1000 reference orbits. We again find no evidence that the initial density gradient p influences the generated stresses. For both $h = 0.05$ and $h = 0.1$ the deviations between the curves representing $p = -0.66$ and $p = -1.5$ are minor and can be explained with statistical effects. In both the top and bottom panel the trend of overall increasing α with increasing h is observed. We also find that higher h leads to a larger difference between the *alpha* values in the midplane and the upper disk layers, though the general dependence of α with height described in chapter 3 is found in all simulations. This is also in accordance with simulations presented by e.g. Stoll & Kley (2014), Stoll et al. (2017) and Flock et al. (2017b).

4.3.2 rms-velocities

We now take a look at the initial growth phase of the VSI by calculating the rms-velocity defined as

$$v_{\mathrm{rms}} = \sqrt{\left(v_r - \langle v_r \rangle\right)^2 + \left(v_\theta - \langle v_\theta \rangle\right)^2 + \left(v_\varphi - \langle v_\varphi \rangle\right)^2} \quad , \tag{4.6}$$

with brackets representing spatial averages in ϕ direction. The averages $\langle v_r \rangle$ and $\langle v_\theta \rangle$ are assumed equal to zero.

In figure 4.3 we plot the spatial average of the rms-velocity as a function of time for the first 200 orbits of the simulations. We find that the simulations for $h = 0.1$ with different values of p start their growth at a similar time and with identical growth rates of $\Gamma = 0.36$ per orbit. This value of Γ is also in good agreement with the values obtained in chapter 3. We also observe the secondary growth phase seen already in the time evolution of the α value and also reported in VSI simulations of Stoll & Kley (2014). The simulations both settle to a steady state value of $v_{\mathrm{rms}} \approx 0.1 c_{\mathrm{s}}$. A similar qualitative behaviour is found for the simulation with $h = 0.05$. The onset of the VSI growth is later than for the $h = 0.1$ cases in agreement with the

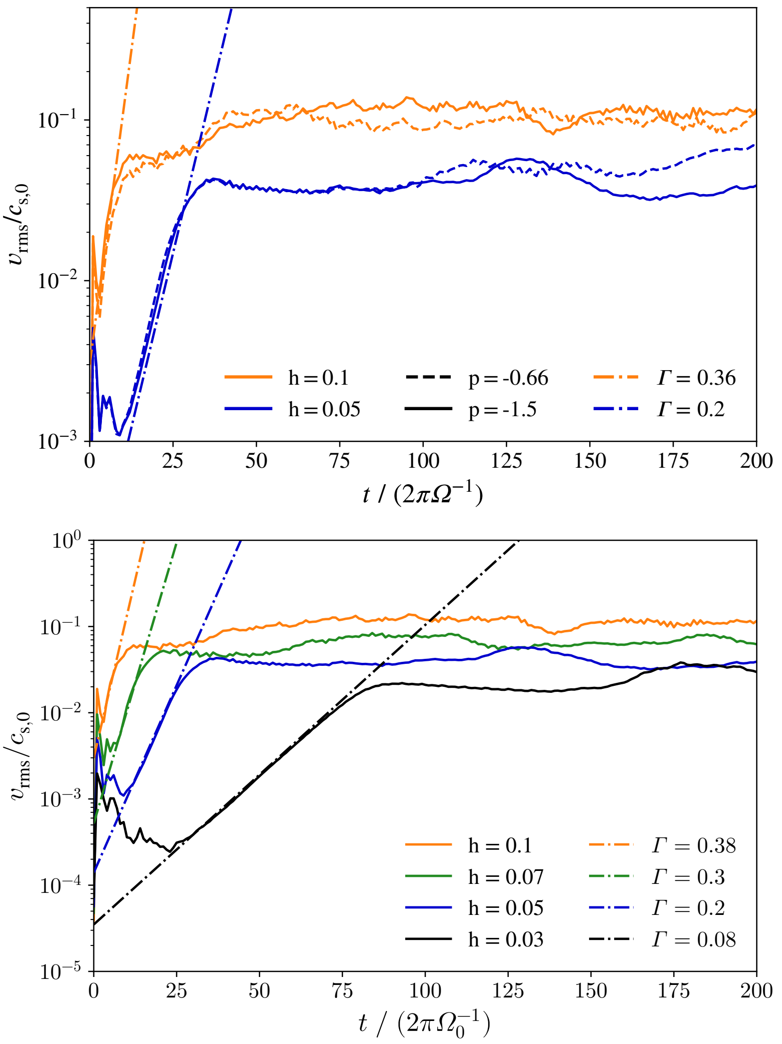

Figure 4.3: Rms-velocities normalised by reference sound speed measured for the initial growth phase of the instability. The top panel compares the disks with $p = -0.66$ and $p = -1.5$ at $h = 0.05$ and $h = 0.05$, while the bottom panel compares different h from 0.03 to 0.1 at a common p value. We additionally plot curves with exponential growth rates Γ for comparison.

results from the analysis of the α stresses. The second growth phase is however not observed in these simulations, instead we find a plateau in the $v_{\rm rms}$ values after the initial growth phase and further growth is only observed after additional 50 orbits. For both values of p we find the initial growth rate to be $\Gamma = 0.2$ per orbit, in agreement with the value found by Stoll & Kley (2014) for their simulations.

The difference in the growth rate between the simulations with different h is expected. Stoll & Kley (2014) showed that for nearly isothermal disks the growth rates obtained by Nelson et al. (2013) can be to first order expressed as

$$\Gamma \sim |q| h \Omega \qquad . \tag{4.7}$$

From this formula it is expected that the growth rate rises proportional to the aspect ratio of the disk, which is what we observe.

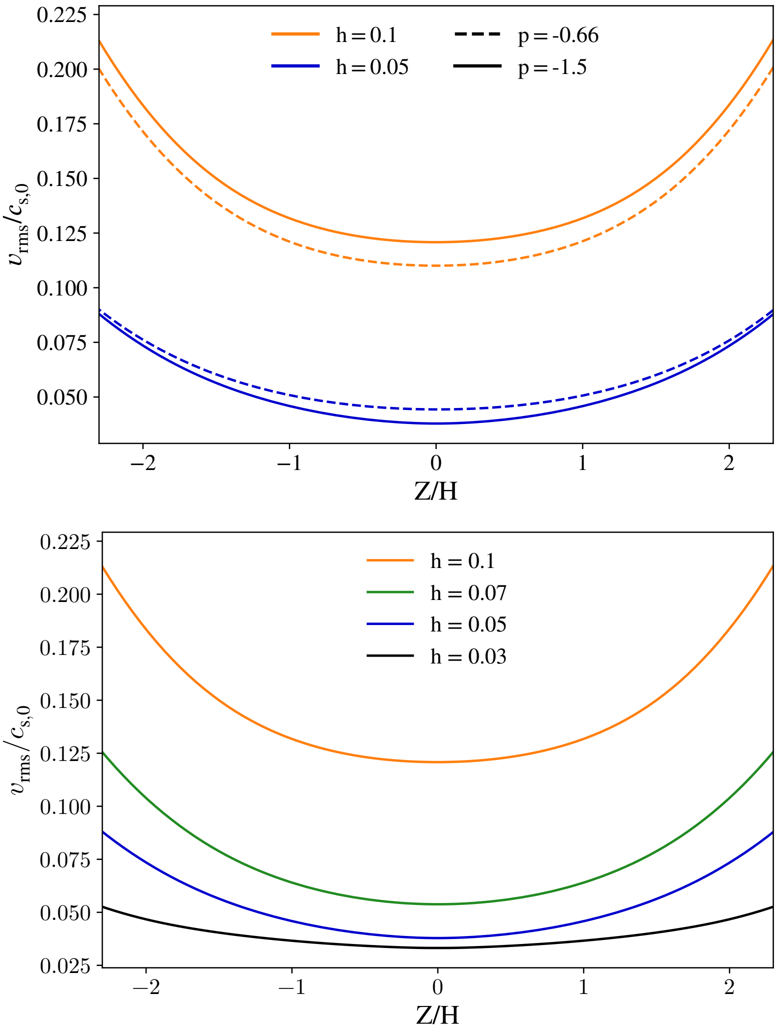

Figure 4.4: Rms-velocities as a function of distance from the disk midplane. The averages are calculated for the remaining dimensions and over the simulation time. Simulations shown in each panel ar the same as in figure 4.3.

In the bottom panel of figure 4.3 we redo the above analysis for the simulations with $p = -1.5$ and different values of h. For the simulation with $h = 0.07$ we find a growth rate of $\Gamma = 0.3$ which is in good agreement with the scaling of equation 4.7. For $h = 0.03$ we however get $\Gamma = 0.08$, which is lower than we would expect based on the growth rates of the other simulations in combination with equation 4.7, from which a growth rate of $\Gamma = 0.12$ would be expected.

In figure 4.4 we look at the vertical dependence of the rms-velocities. In the top panel, we again find the curves corresponding to the same h to agree well with each other, supporting our claim that the initial density gradient does not influence the simulation result. For $h = 0.1$ the rms-velocity at the miplane is $v_{\rm rms} = 0.13c_{\rm s}$ and rises to $v_{\rm rms} = 2c_{\rm s}$ in the upper layers. These results are consistent with the results obtained in chapter 3 taking into account that we included the ϕ component of velocity in the calculation of $v_{\rm rms}$ presented in this chapter. Comparing the results for the different h shown in the bottom panel of figure 4.4, we find that the overall shape of the $v_{\rm rms}$ stays similar for all cases, although the difference between the

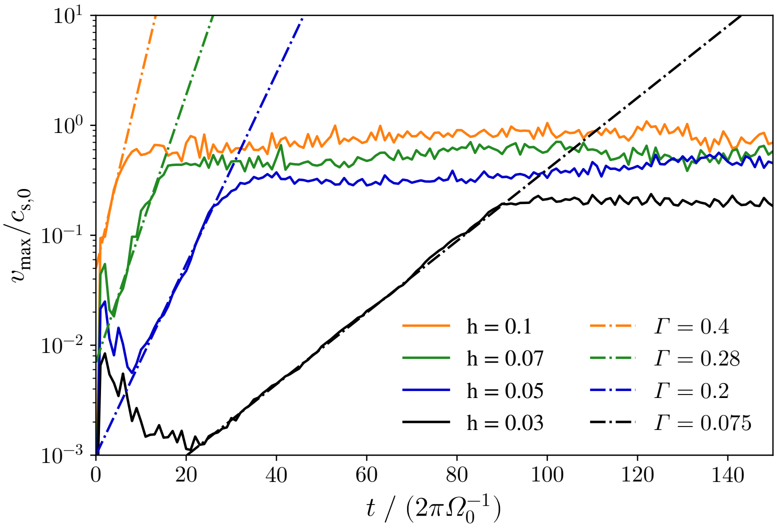

Figure 4.5: Maximum perturbed velocity as a function of time for the initial growth phase for different values of h. We again show exponential growth rates as a comparison.

velocity at $z = 0$ and $z = 2H$ increases with increasing h. A similar correlation exists between h and the v_{rms} value at $z = 0$, which is larger for higher h. This is expected, as a warmer disk has more shear energy available to be converted into turbulence.

Because of the vertical dependenc of the velocity fluctuations and the fact that the growth of an instability is in fact governed by the larges and not the root-mean-square velocity, we calculate the maximum velocity as

$$v_{\mathrm{max}} = \sqrt{v_r^2 + v_\theta^2} \quad . \tag{4.8}$$

We neglect the ϕ component of velocity in this case as the VSI has been shown to grow axisymmetrical. The results are shown in figure 4.5 for the simulations with $p = -1.5$, where we again plot growth rates for comparison. We find the growth rates obtained using v_{max} to be in good agreement with the ones obtained using v_{rms}.

To compare our results with the theoretical ones presented in Lin & Youdin (2015) we calculate the h independent growth rate

$$\sigma = \frac{\Gamma}{h\Omega} \quad .$$

For the simulations with $h = 0.1$, 0.07 and 0.05 we obtain $\sigma = 0.64$, which is in good agreement with the results presented by Lin & Youdin (2015) for a disk simulation with $z_{\mathrm{max}} = 3H$ and radial wavenumber k=30. Because we obtained a smaller than expected growth rate for $h = 0.03$, this case also have a lower σ and does not align well with their largest expected growth rate.

4.4 Vortex formation and structure: Dependence on disk conditions

To identify vortices in our simulations, we use the vertical component of the vorticity, defined as the rotation of the velocity vector $\mathbf{v}$:

$$\omega_z = (\nabla \times \mathbf{v})_z \qquad . \tag{4.9}$$

In this section, we use the vorticity scaled by the orbital frequency Ω to identify and characterise the vortices forming in the disks at different values of p and h.

4.4.1 Midplane vorticity

Figures 4.6 and 4.7 show the midplane value of the vertical vorticity for the simulations with different p and h after 900 reference orbits. We find vortices forming in all our simulations irrespective of the values assumed for p and h. Each simulation has formed between 2 and around 10 vortices at this point in the simulation, but there is no correlation with the chosen parameters how many vortices form. The strength of the vortices however shows a correlation with the disk aspect ratio, best seen in figure 4.7. The vortices in the bottom left panel corresponding to the simulation p1.5h0.1 appear to have lower absolute vorticity than the simulations in the top row corresponding to simulations p1.5h0.03 and p1.5h0.05. Because the disk has overall vorticity $\omega_z = \frac{1}{2}\Omega_\mathrm{K}$, the lower absolute vorticity in the centre of the vortices in the lower right panel corresponds to a larger relative vorticity and therefore vortex strength.

In figure 4.7 it can also be seen that both simulations in the bottom row are currently undergoing merging events of large vortices.

Additionally, the run p1.5h0.03 shows a ordered band structure in vorticity, which does not appear in the other simulations at this stage, although the simulations with h=0.05 show axisymmetric bands at some radii. The band structure however appears for all simulations during the growth phase of the VSI, but it breaks down soon after. In chapter 3 we already put forward the hypothesis that the RWI is working as a secondary instability in our simulations, and the breakdown of this azimuthal structure could be an indication of the onset of the RWI. In this case, the RWI would not be fully saturated for the simulation p1.5h0.03 even at this late stage, likely due to the longer growth time of the VSI in combination with a lower vorticity maximum generated in the disk.

4.4.2 Vortex size

Because we are also interested in the size and shape of the vortices formed, we choose one vortex from each simulation for a close up inspection. Figures 4.8 and 4.9 show the vortices taken from figures 4.6 and 4.7, respectively, in a local coordinate system centred on the vortex. We express the radial and azimuthal coordinate as a function of the local pressure scale height for easier comparison. The center coordinates of each panel are listed in the corresponding figure caption.

We find that the vortices share a common size of 1-1.5 local scale heights in radial diameter and an azimuthal size between 10 and 20 H, leading to aspect ratios

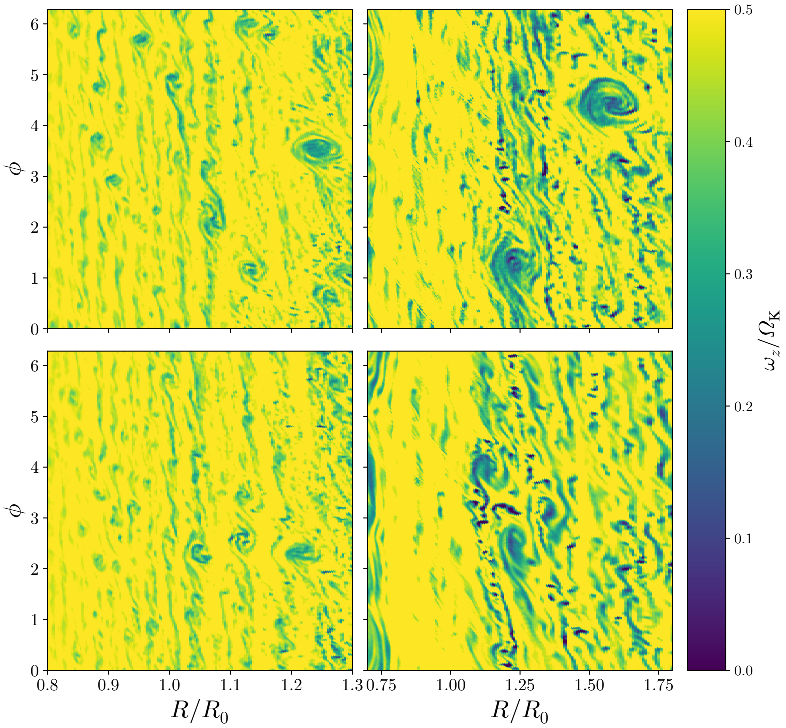

Figure 4.6: Midplane vorticity for different values of p and h. The top row shows simulations with p=-0.66 and the bottom row with p=-1.5. For the left column, the aspect ratio of the simulations is h=0.05, resulting in less extended structures than seen in the right column where h=0.1 .

χ in the range of 8.5 - 20. Figure 4.9 again shows the dependence of the relative vorticity on the disk scale height, but no correlation of vortex size or aspect ratio with disk aspect ratio h can be found. Figure 4.8 seems to indicate that the vortices are larger for simulations with p=-0.66, but as the vortices depicted from the simulation p1.5h0.1 are currently merging, this could be artificial. This is supported by the fact that the top left panel of figure 4.6 shows run p0.66h0.05 to also form vortices with a sizes comparable to the ones found in p1.5h0.05.

4.4.3 Vortex evolution

To track the radial position of the vortices over time, we use the same technique employed in chapter 3. Therein, we calculate the radial positions of the vortices in each timestep by first applying a box filter to the vertical vorticity to eliminate all structures smaller than 1 H in radius and 6 H in azimuth. Then the azimuthal average of the vorticity is subtracted from this to exclude possible zonal flows and then the minimum value in azimuthal direction is calculated.

The results are shown in figures 4.10 and 4.11. In all cases, we find the formation of long lived vortices at the radial positions of the vortices depticted in figures 4.6 and 4.7, though the time after which the stable vortices appear seems not directly correlated to neither density gradient nor aspect ratio. For example, the simulations p1.5h0.05 and p0.66h0.1 show stable vortex formation early on, while p1.5.h0.1 first shows intermittent large vortices before forming long time stable vortices. The same

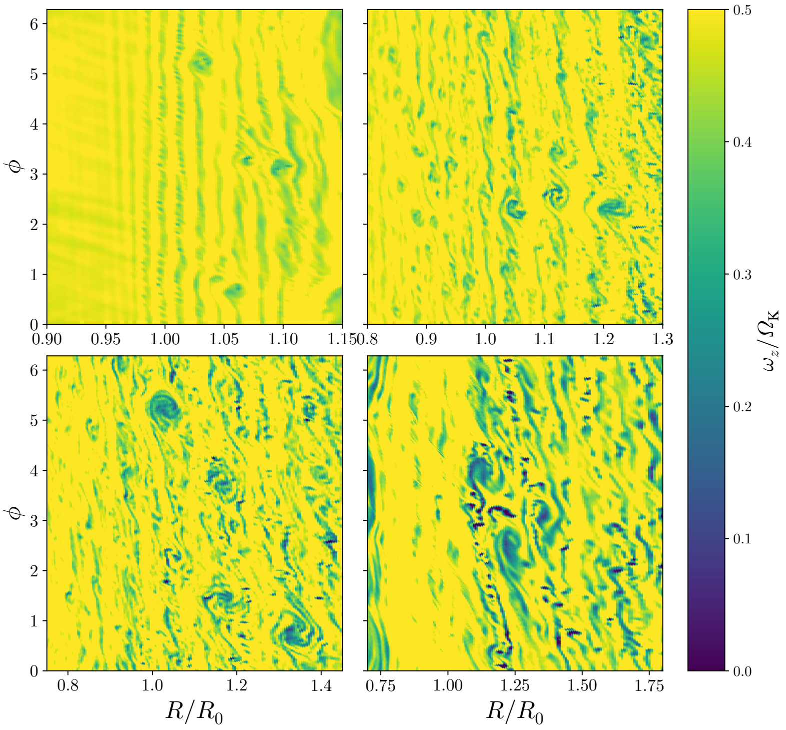

Figure 4.7: Midplane vorticity for different values of the disk aspect ratio h. The top left panel shows the simulation with the smallest h=0.03, increasing to h=0.05 in the top right, h=0.07 in the bottom left and h=0.1 in the bottom right panel. All simulations have initially p=-1.5. Note the increase in vorticity and decrease of overall structure with increasing h.

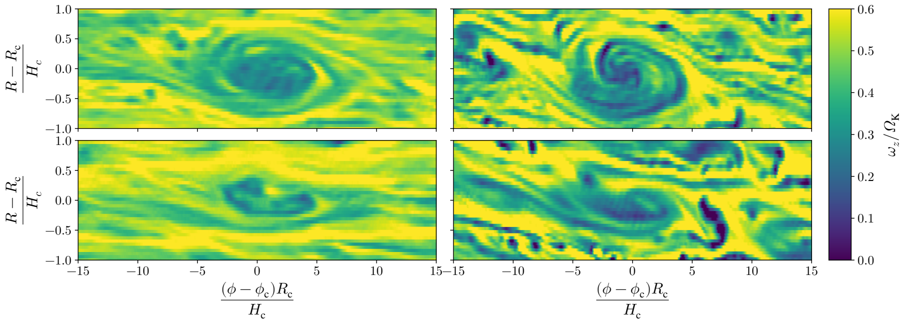

Figure 4.8: Vortex extent for different values of p and h. The simulations are, clockwise from the top left: p0.66h0.05 with $R_c, \phi_c = 1.25, 3.5$, p0.66h0.1 with $R_c, \phi_c = 1.6, 4.5$, p1.5h0.1 with $R_c, \phi_c = 1.25, 2.5$ and p1.5h0.05 with $R_c, \phi_c = 1.05, 2.25$.

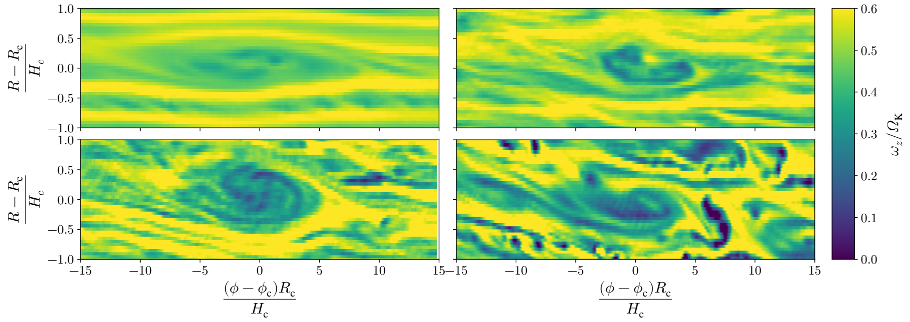

Figure 4.9: Vortex extent for different values of h. The simulations are, clockwise from the top left: p1.5h0.03 with $R_c, \phi_c = 1.03, 5.25$, p1.5h0.05 with $R_c, \phi_c = 1.05, 2.25$, p1.5h0.1 with $R_c, \phi_c = 1.25, 2.5$ and p1.5h0.07 with $R_c, \phi_c = 1.03, 5.25$.

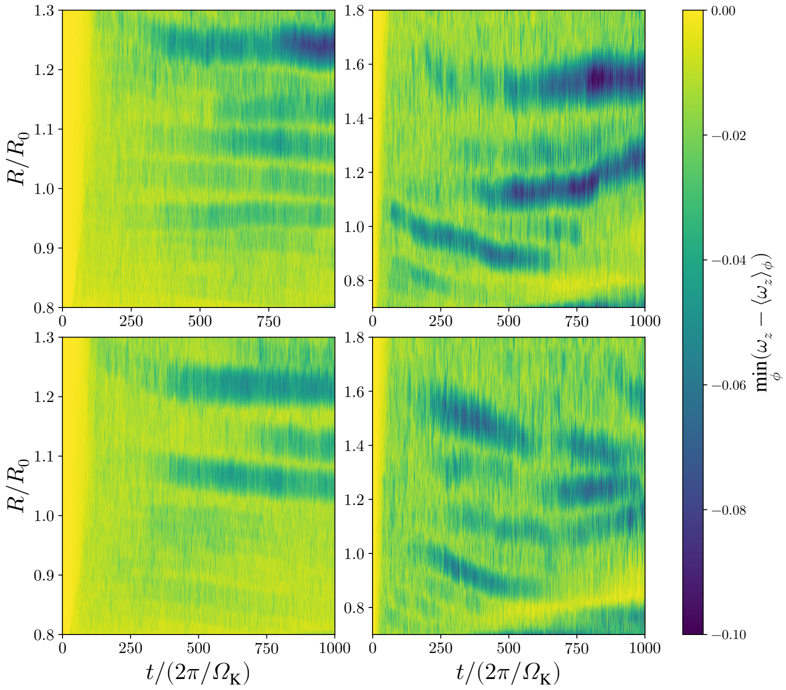

Figure 4.10: Evolution of the vortex radial position as a function of time. The panels are sorted as in figure 4.6 with columns corresponding to aspect ratio and rows to density gradient. The color shows the azimuthal minimum of the vertical vorticty subtracted by the azimuthally averaged vorticity. To extract only larger scale minima, we apply an image filter prior to the calculation.

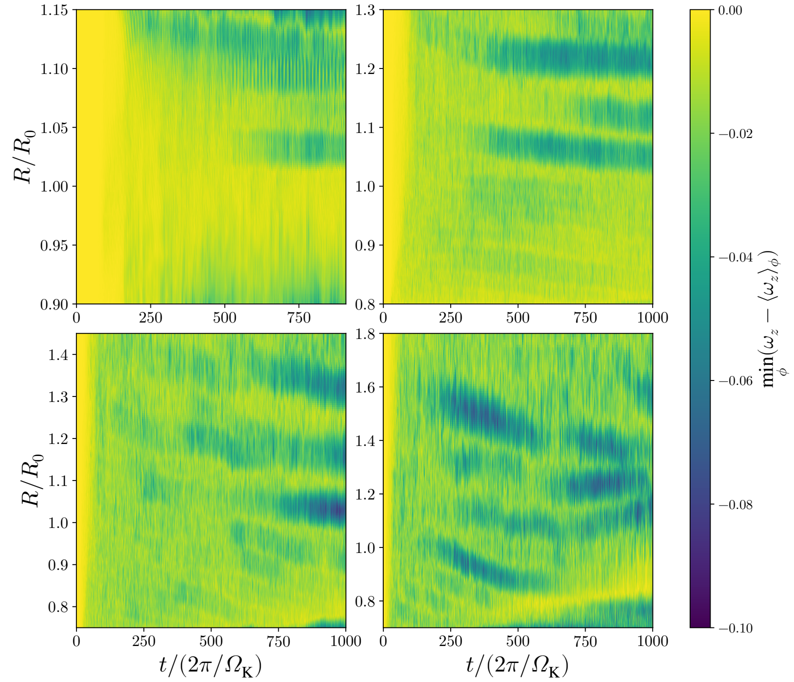

Figure 4.11: Same as figure 4.10, but now for the different disk aspect ratios as in figure 4.7.

can be found upon inspecting additional frames of the run p1.5h0.07 which in figure 4.11 only shows strong stable vortices emerging well after 750 orbits, but vortices can be found much earlier in the simulation, though their constant interaction makes it hard to detect them with this method. An exception in both the time of onset of vortex formation and the number of vortices formed is again run p1.5h0.03 which shows only one stable vortex forming after around 600 orbits, though this could be again attributed to the longer evolution timescale of the VSI itself.

Upon inspection of the time series of the midplane vorticity, we also find that even if a vortex has established itself, new vortices can be formed at the same radial distance to the star, of which one example can be seen in the bottom left panel of figure 4.7. The newly formed vortex catches up with the dominant vortex after a few tens to hundred orbit and is eventually absorbed into the stronger vortex. We also find evidence of this in other runs, e.g. p0.66h1.5, but as both examples occur for vortices located close to the reference radius we cannot exclude that this happens for other vortices also. The effect is most easily observed close to R_0 because we take one snapshot after each completed orbit at R_0, leading the azimuthal position of the vortices with $R > R_0$ and $R < R_0$ to drift due to the radial dependence of Ω.

Different to our results from chapter 3, we observe vortex destruction in our simulations with h=0.1. In both simulations, vortices formed early and close in in the disk are destroyed after ca. 500 and 300 orbits for p==0.66 and p=-1.5, respectively. For the case p=-0.66 this is due to a vortex forming radially close to the vortex and interacting with it until it is destroyed. For the case p=-1.5 something similar seems to happen, but we cannot exclude the influence of the boundary in this case.

We also observe the migration of the vortices over time in all cases except

model	grid size ($N_r \times N_\theta \times N_\varphi$)	$\langle\alpha\rangle/10^{-4}$
n128	256×128×128	4.9 ± 1.0
n256	256×128×256	5.4 ± 1.3
n512	256×128×512	6.8 ± 1.6
n1024	256×128×1024	7.2 ± 1.5

Table 4.3: List of parameters for the resolution study. The simulation n1024 is identical to p1.5h0.1 from table 4.2.

p0.66h0.05 and p1.5h0.03. For the former this is likely due to the large amount of vortices formed in the disk which prevents radial migration due to the interaction of the vortices with each other. For the latter, it is simply the late time of the formation of the vortices that prohibits us from detecting migration, though it is possible that it occurs later on. For the migrating cases, the migration is stronger for simulations with larger aspect ratio. This can be explained by the fact that the vortices formed in disks with larger h are stronger, but we cannot exclude the influence of the disk surface density gradient, which changes most for the cases with large h due to overall mass loss.

4.5 Azimuth resolution study

To determine the minimum grid resolution in azimuthal direction required to achieve a converged nonlinear state of the VSI and form vortices, I perform a small resolution study. For all simulations I use the parameters of the simulation run p1.5h0.1 described in table 4.2 and vary only n_ϕ. The simulations performed are listed in table 4.3.

Figure 4.12 shows the results of the parameter study. We find that both the spatial average of α and v_{rms} show converged values which is the expected outcome as the VSI modes grow axisymmetrically.

We also find that the cases n256, n512 and n1024 give similar results when looking at the vertical profiles of α and v_{rms}, and the results are similar. Contrary to this, the simulation n128 shows steeper profile of both values with height than the other simulations. Looking at figure 4.13, we find that n128 is the only case in which no vortex formation is observed. We find a similar behaviour in our analysis presented in chapter 3 for the α value for different spatial sizes in the azimuthal direction, where the profile is also steeper for the case where we exclude that vortices form in the disk. Therefore, the formation of vortices could have an influence on the strength of the angular momentum transport higher up in the disk.

4.6 Conclusions

In this chapter we present the first 3D high resolution parameter study on the Vertical Shear Instability. In this study, we focus our attention on the parameter

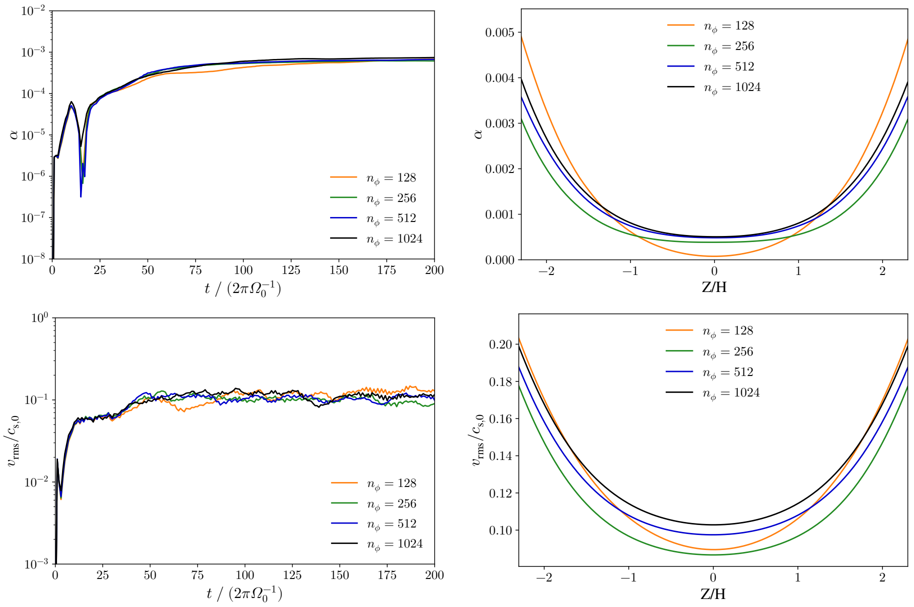

Figure 4.12: Turbulence analysis of the simulations performed for the resolution study. The top row shows the α value as a function of time on the left and the the dependence on height on the right. The bottom row shows the same for the rms-velocity.

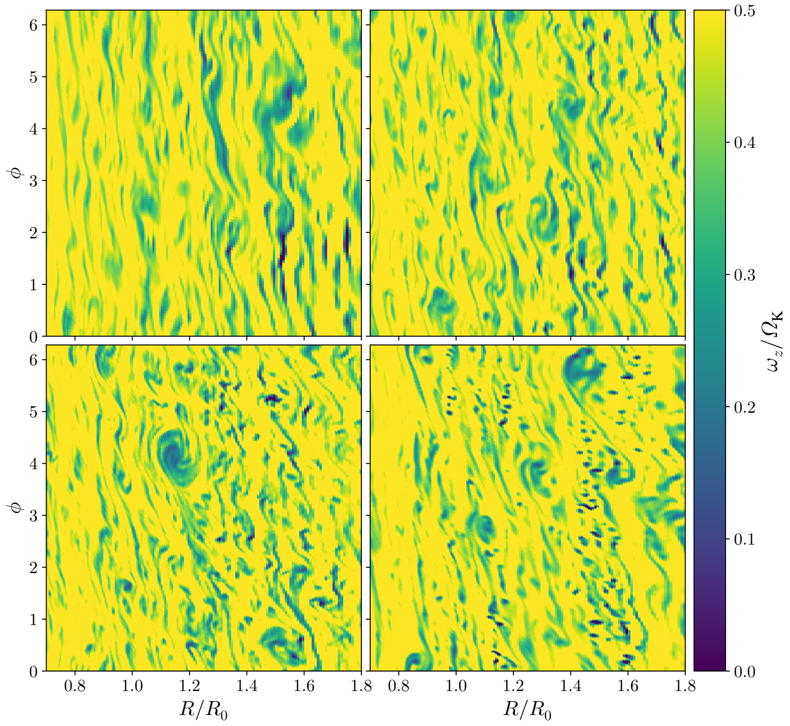

Figure 4.13: Midplane vorticity after 500 orbits for each simulation considered in the resolution study.

determining the initial density slope p of the disk and the disk aspect ratio h. The analysis of the parameters determining cooling time and temperature gradient will be the the focus of a future work. For now, we assume $\tau \approx 10^{-4}$ and and $q = -1$.

We find that the VSI is capable to support angular momentum transport with α values up to a few times 10^{-4} for the largest scale height. With decreasing scale height, the α value decreases down to a value of a few times 10^{-5} for the lowest scale height investigated. The α values we find in our simulations are in accordance with the values we reported in chapter 3, but lower than the values found by Stoll & Kley (2014). We find a similar relation with h for the rms velocities and the instability growth rates, which are also increasing with increasing h. The growth rates we find are in good agreement with previous studies of chapter 3 and Stoll & Kley (2014). In vertical direction, the quantitative behaviour we observed in chapter 3 is recovered. Contrary to the aspect ratio of the disk, the density gradient does not show any influence on the disk turbulence. This result is expected, as the VSI itself is not sensitive to the density gradient.

We find that the VSI is able to seed multiple vortices in all considered parameter combinations and the vortices in all simulations live for hundreds of orbits. The vortices generally have a radial diameter between 1 and 1.5 local scale heights, which is close to the diameter of 2 H allowed by the disks radial shear. Most vortices have aspect ratios of $\chi \simeq 8$ but values of up to 20 are found. The time at which the first stable vortex appears is not correlated with any of the investigated parameters, and it is likely that such a time is random. We also do not find a correlation between the number of vortices found simultaneously in the disk and any of the investigated parameters.

An interesting observation is that the turbulence sustained by the VSI steadily creates new vortices even at radii at which a large scale vortex has already been established for a longer period of time. This could indicate that the VSI constantly works to replenish the vorticity gradient that drives the Rossby-Wave-Instability, which once replenished sufficiently creates new vortices. These new, weaker vortices are then eventually absorbed by the larger vortex already present.

In this work, we considered the disk to be comprised purely of gas. In reality, the disk contains ca. 2% solids, which have been shown to change the buoyancy of the disk and can therefore have an impact on the growth of the VSI especially near the midplane (Lin 2019). Future simulations should therefore investigate whether vortices also emerge in a dusty disk when the vsi is suppressed close to the midplane. We also suggest further simulations of the VSI are conducted to narrow down the possible alpha values generated by the instability, as there is as of yet no convergence on the values reported in this work or previous works from the literature.

CHAPTER 5

VORTEX SIGNATURES CAN BE PRODUCED BY VERTICAL SHEAR INSTABILITY

From Manger & Klahr, 2019 submitted to A&A

5.1 Introduction

In recent years high resolution imaging of protoplanetary disks has shown how diverse the shape and structure of disks forming around young stars can be. In almost all disks investigated so far either rings, spirals or asymmetric, vortex-like structures have been observed. Some examples among the disks showing asymmetric features are OphIRS48 (van der Marel et al. 2013, 2015), MWC 758 (Marino et al. 2015; Boehler et al. 2018; Dong et al. 2018) and HD 135344B (Pérez et al. 2014; van der Marel et al. 2016; Cazzoletti et al. 2018), whereas HL Tau is known for its rings (ALMA Partnership et al. 2015), although non-axisymmetic features have recently been detected using the VLA (Carrasco-González et al. 2016). Spirals have for example been detected in near infrared observations of MWC 758 (Benisty et al. 2015) and sub-mm observations of Elias 2-27(Pérez et al. 2016).

There are many explanations for the observed structures. The most common explanation is a planet inciting spiral arms as well as carving a gap. The gap formation can then excites vortices via the Rossby Wave Instability (Lovelace et al. 1999; Li et al. 2000) due to the density gradient present at the gap edges, explaining the vortices observed at these positions. But recent studies have shown that weakly magnetised protoplanetary disks with Magneto-Rotational instability (MRI) in the inner disk to also trigger the RWI at the edge of the the so-called MHD dead zone, where the disk becomes laminar with respect to the MRI(Dzyurkevich et al. 2010; Flock et al. 2015). To form vortices inside the dead zone, but also in the outer regions of a weakly magnetised disk, instabilities related to the baroclinicity of the disk have been shown to be promising candidates. The convective overstability (Klahr & Hubbard 2014; Lyra 2014) and its non-linear cousin, the subcritical baroclinic instability (SBI, Klahr & Bodenheimer 2003; Raettig et al. 2013) have been shown to seed and amplify large scale vortices in protoplanetary disks. In chapter 3 we showed the Vertical Shear Instability(Nelson et al. 2013), first investigated in stars as the Goldreich-Schubert-Fricke instability(Goldreich & Schubert 1967; Fricke 1968), to also trigger the formation of large scale vortices via the RWI mechanism.

Vortices also allow the circumvention of a central problem in planet formation: the drift barrier (Birnstiel et al. 2010). At micrometer sizes, particles can stick together to form pebbles of about millimetre size, but the (size-dependent) drift velocity(Weidenschilling 1977) due to the pressure support of the gas prohibits growth much larger than this as dust drifts inward faster than the particles can stick together. But vortices alter the pressure structure in a disk to allow the particles to drift towards the center of the vortex instead of the star. This trapping mechanism enables to form large concentrated over-densities (Barge & Sommeria 1995; Klahr & Bodenheimer 2006; Meheut et al. 2012) in the disk to allow gravity or streaming instability to take over(Raettig et al. 2015) and form planetesimals.

In this chapter we apply a steady state dust concentration model inspired by the work of e.g. Klahr & Henning (1997) and Lyra & Lin (2013, hereafter LL13) to our results presented in chapter 3 to show the capability of the VSI to qualitatively reproduce observations of protoplanetary disks with multiple vortices, which are commonly identified as results of planets orbiting within those disks. We show that the vortices produced by the VSI are visible to observations in this simplified model and that future investigations calculating the dust distribution alongside the gas are required and justify the additional computational cost. In section 5.2 we briefly review the model used by LL13 and describe our application to the gas-only simulation of chapter 3 before presenting and discussing our results in section 5.3. Finally, section 5.4 gives a brief conclusion.

5.2 Model

5.2.1 Gas Disk

For the gas disk structure in our model we use results of numerical simulations presented in chapter 3. Therein, we performed numerical simulations of protoplanetary disks with active Vertical Shear Instability for multiple set-ups with different azimuthal disk ranges and evolution times of 800-1000 orbits at the reference radius. We will use the results of the full 2π simulation presented in chapter 3 after 500 orbits at the reference radius, shown in figure 5.1. The model used in that chapter has a radial midplane density gradient $p = -0.66$, a radial temperature gradient $q = -1.0$ and a geometric scale height $H/R = 0.1$. We are aware that these gradients are different than the values expected at large distances from the star in protoplanetary disks (Pfeil & Klahr 2019). We however argue that the occurrence of vortices in VSI-active disks should not depend on the specific value of the density and temperature gradients as long as they allow for the VSI to grow.

In figure 5.1 we show the vorticity on the left and the gas density on the right at the midplane of our model. In vorticity we clearly detect two large scale vortices on the left side visible as darker oval patches in the disk. At the corresponding positions in the gas disk we find a clear gas density enhancement at the position of the inner vortex and also a slight enhancement at the position of the outer vortex. Additionally, we find many large spiral arms present in the gas disk, launched by small vortices formed in the disk. The small vortices themselves are short lived and

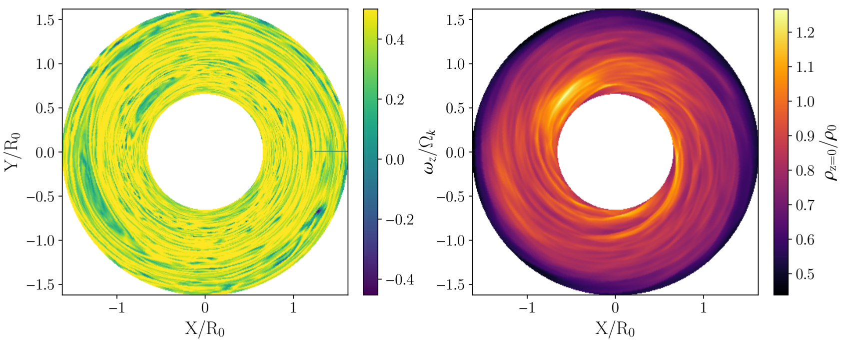

Figure 5.1: Midplane vorticity and gas density of our model. The left image shows the data in the same way as presented in 3.8. The right image shows the corresponding gas density, showing density enhancements at the positions of the vortices and additional spiral arms in the disk.

are not able to concentrate sufficient material to allow for planetesimal formation or detection in observations.

5.2.2 Dust Disk

For the dust component we use a model inspired by various authors (Klahr & Henning 1997, LL13), where the authors derived an analytical solution for the dust density inside a trapping vortex assuming the dust is in a diffusion-sedimentation equilibrium, taking into account the effects of particle drift along pressure gradients. These effects do not work for spiral arms we see in the gas, because they propagate with respect to the gas. Only zonal flows and vortices are quasi geostrophic flow features in which pressure forces are balanced by centrifugal and Coriolis forces. One can prescribe the time averaged gas column density inside a vortex as a Gaussian distribution

$$\Sigma_{\mathrm{g}} = \Sigma_{\mathrm{g,max}} \ \exp\left[-\frac{b^2}{2H_{\mathrm{g}}^2}\right] \tag{5.1}$$

with the vortex coordinate b defined as

$$b = \sqrt{\left(R - R_0\right)^2 + \left(\frac{R_0}{\chi}\right)^2 \left(\phi - \phi_0\right)^2} \qquad . \tag{5.2}$$

Here R is the radial and ϕ the azimuthal coordinate and (R_0, ϕ_0) the position of the vortex center with the vortex scale length $H_{\mathrm{g}} = H/f(\chi)$, which itself is a function of the disk pressure scale height H, the vortex geometry function f and the aspect ratio χ, the maximum gas column density at the center of the vortex $\Sigma_{\mathrm{g,max}}$. The dust will now sediment towards the center of the vortex until the gradients in dust to gas ratio are strong enough to balance sedimentation by diffusion with diffusivity $D = \delta c_s H$, which leads to a smaller scale height h than for the gas as long as the Stokes Number of the particles $\mathrm{St} = \Omega\tau$ is larger than the diffusivity. A good approximation for the scale height of the dust-to-gas ratio is

$$h = H\sqrt{\delta/\mathrm{St}} \qquad . \tag{5.3}$$

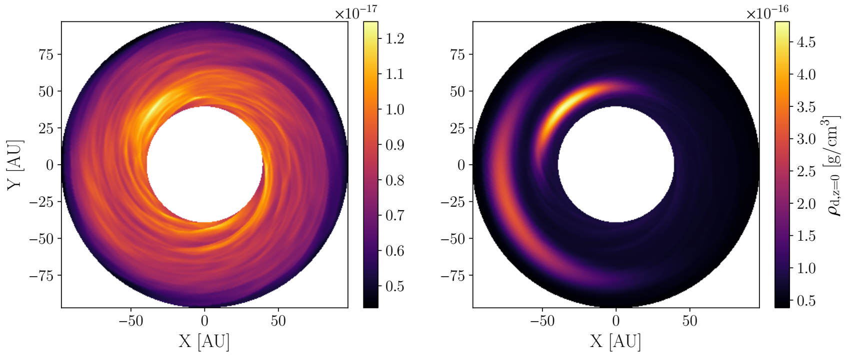

Figure 5.2: Dust midplane density for $a_\bullet = 1\mu$m (left) and 100 μm (right) for the model with $\Sigma_0 = 16$ g/cm^2. The small particles mainly trace the gas flow, whereas the larger particles concentrate inside the vortex.

In an analytic gas vortex (LL13) one would therefor obtain a dust distribution of

$$\Sigma_\mathrm{d} = \epsilon\,\Sigma_\mathrm{g,max}\,(S+1)\;\exp\left[-\frac{b^2}{2H_\mathrm{g}^2}\,(S+1)\right] \qquad . \tag{5.4}$$

where $S = \mathbf{St}/\delta$ describes the relation between the Stokes number of the particles and the turbulent diffusion of the dust. We note that the derivation of Equations 5.1 and 5.4 assumes small Stokes numbers (St $\ll 1$), which limits their application to small grains up to a few millimetres. They also use the shearing sheet approximation, which limits the validity of the equations to a small region around the vortex. As the dust density is also calculated a posteriori from the vortex structure set by the gas, the back reaction of the particles is neglected; which is equal to assuming low dust-to-gas mass ratios.

For our purpose, where we have the true gas distribution inside and outside the vortex we derive only the local dust to gas surface density ratio from the above considerations, i.e. the metallicity $Z = \frac{\Sigma_\mathrm{d}}{\Sigma_\mathrm{g}}$ as function of space. Outside of the dust vortex h, Z is set to the background value, and inside the vortex in increases up to $S+1$ in the very center.

$$Z(R,\phi) = \frac{\Sigma_\mathrm{d}}{\Sigma_\mathrm{g}} = Z_0\left(1 + S\exp\left[-\frac{b^2}{2H_\mathrm{g}^2}\,S\right]\right) \tag{5.5}$$

The vertical distribution of ρ_d is then given by another diffusion-sedimentation process via

$$\rho_\mathrm{d} = \frac{\Sigma_\mathrm{d}}{\sqrt{2\pi}}\exp\left(-\frac{z^2}{2\,h^2}\right) \qquad . \tag{5.6}$$

For simplicity, we assume $\delta = \alpha$ with α the turbulent viscosity parameter as described by Shakura & Sunyaev (1973). We set $\alpha = 10^{-3}$, the global average value obtained in the simulations presented in chapter 3. We also assume that the particles in our model are all small enough to be treated in the Epstein regime, for which the Stokes number can be written as

$$St = \frac{a_\bullet\,\rho_\bullet}{\rho_\mathrm{g}\,H} \tag{5.7}$$

with the dust material density $\rho_\bullet$ and grain size $a_\bullet$.

We fit the column density from the simulations presented in chapter 3 using equation 5.1 to determine the position of the vortices. The best fit of the numerical data sets the inner vortex at $(R_i, \phi_i) = (53.0\text{ AU}, 2.29\text{ rad})$ and the outer vortex at $(R_o, \phi_o) = (79.1\text{ AU}, 3.48\text{ rad})$ for a reference radius of $R_0 = 60$ AU. The aspect ratios are set as determined in chapter 3 as $\chi_i = 8$ and $\chi_o = 10$ and the vortex scale lengths are determined from the vortex solution of Goodman et al. (1987) as $H_{g,i} = 7.9$ AU and $H_{g,o} = 11.8$ AU.

We then use equation 5.6 to determine the dust density for the different particle sizes listed in section 5.2.3,where we assume the particle size to be constant and use equation 5.7 to calculate the local stokes number of the dust. For all particle sizes listed in section 5.2.3 the Stokes number stays well below unity close to the midplane of the disk for all models considered. Only for the models with low disk mass the Stokes number of the largest particles is larger than one in the upper layers of the disk, but the densities in those regions are too low to enact particle back reaction. Additionally, we verified that the total dust to gas ratio does not surpass unity in all but the lowest-mass model. In this model the dust to gas ratio is slightly above unity in the innermost part of the vortex, which would enable streaming instability. But as the region is smaller than the total vortex size, we argue that this would not affect the result significantly because Streaming Instability cannot destroy vortices (Lyra et al. 2018). An example of the dust density for small and medium size particles in the midplane of the disk is shown in figure 5.2.

5.2.3 Radiative transfer

We use the Radiative Transport code RAMC3D[1] to calculate the intensities for the dust continuum emission of the disk. We use the stellar properties of the Herbig Ae star MWC 758 as summarized in Boehler et al. (2018). The stellar mass is $M_\star = 1.4 M_\odot$, the stellar radius $R_\star = 2.0 R_\odot$ and the surface temperature is given as $T = 8130$ K. The system is located at a distance $d = 151$ pc. We set the reference radius of our model at $R_0 = 60$ AU as the vortex structure is observed at a comparable radius and Pfeil & Klahr (2019) predict that the VSI is able to operate at this radius.

The opacity tables are calculated with the BHMIE code of Bohren & Huffman (1983) embedded in a python script. We use Pyroxene grains with a material density of 3 g/cm^3 and assume their total dust-to-gas-mass-ratio to be $\epsilon_{sil} = 3.4 \cdot 10^{-3}$. We are aware that the disk at the assumed radial distance is most likely comprised of a mix of silicate and ice grains, we however refrain from the use of complex mixed opacities in our simplified model. We assume the disk to be comprised of grains having sizes $a_\bullet$ from 0.1 μm to 2 mm, as these are the sizes visible to observation. The grains are binned in eight size ranges with representative sizes of 1 μm, 10 μm, 55μm, 100 μm, 325 μm, 550 μm, 775 μm and 1 mm. We calculate the dust distribution for each of these representative sizes and assume that the dust distribution does not vary significantly inside each bin. The particle mass is distributed between these bins using a power-law distribution for the particle number density

$$n(a_\bullet) \propto a_\bullet^{-3.5} \quad . \tag{5.8}$$

---

[1] http://www.ita.uni-heidelberg.de/ dullemond/software/radmc-3d/

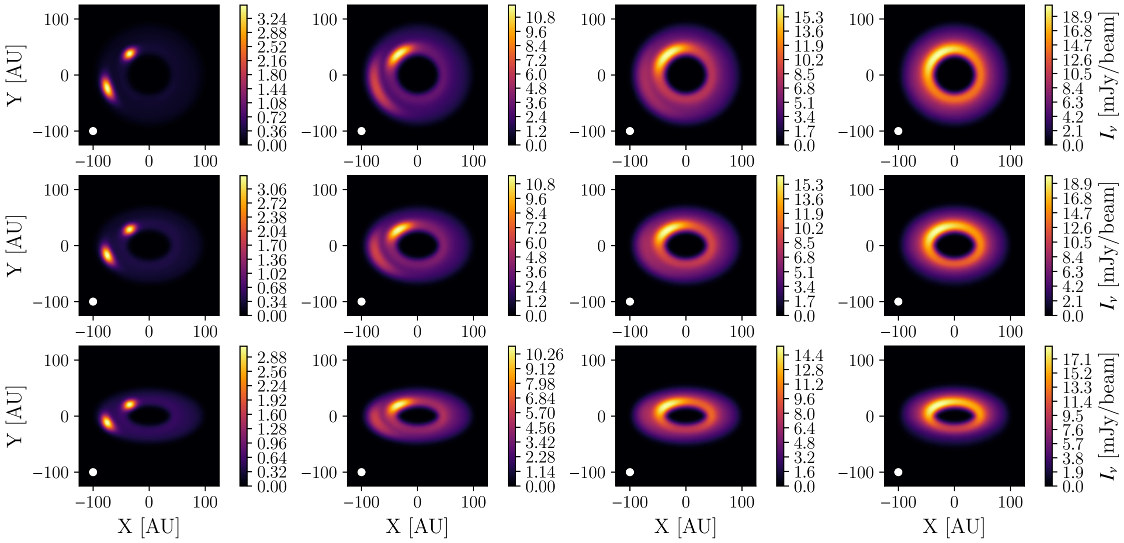

Figure 5.3: Mock observation images of the simulated disks for different disk column densities and inclinations. The reference surface densities from left to right are $\Sigma_0 = 1.6$, 16, 40 and 80 g/cm^2, and the inclinations with respect to the observer from the top row downwards are $i = 20°$, 45° and 60°.

Due to dust growth and planetesimal formation via streaming instability larger grains would certainly also be located inside the vortex. As they are however not accessible to observations, we choose to ignore them in this model.

The images are calculated in a 2-step procedure: We first use a thermal Monte-Carlo simulation with $n_{\text{phot.}} = 10^8$ to determine the temperature of the dust phase in equilibrium with the thermal radiation from the star. We then perform the scattering ray-tracing computation using isotropic scattering with $n_{\text{phot.,scat.}} = 10^8$ to calculate the final image of the disk.

5.3 Results and Discussion

5.3.1 Images

Figure 5.3 shows the intensity map of the simulated disk at 880 μm (ALMA Band 7) folded with a 2D circular Gaussian with $\sigma_{\text{beam}} = 5$ AU (equal to a circular beam with FWHM ≈ 12 AU). We use a different reference column density for each column, increasing from left to right, $\Sigma_0 = 1.6$, 16, 40 and 80 g/cm^2, equal to respectively 1, 10, 25 and 50 times the estimated column density $\Sigma_{\text{ref}} = 1.6$ g/cm^2 of MWC 758. The rows show the disk for each column density at an inclination of 20°, 45° and 60°, respectively.

We find that the inner vortex in our disk is visible in all investigated configurations. For the lower two disk masses also the second vortex is visible in the images, but for the two images on the right hand side the second vortex is outshone by the disk emission. For higher inclinations the presence of the outer vortex is nevertheless deductible in the middle right column despite its weak emission. This is due to the position of the vortex in the lower left part of the disk, increasing the overall

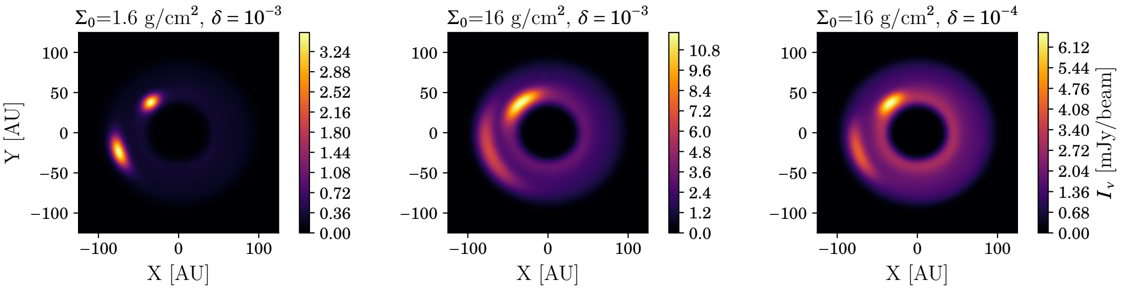

Figure 5.4: Mock images of the simulated disks for the two lowest disk column densities and two different values of the diffusion coefficient δ. We find that lowering δ has a similar overall effect than increasing Σ_0, but due to the influence of δ on the dust settling a constant ratio of δ and Σ_0 does not yield identical results.

intensity on the left side compared to the right side when the disk is inclined. This occurs because the outer vortex is intrinsically weaker than the inner vortex. We also find that the vortices are at least marginally resolved in all cases except for the least massive case, where the inner vortex is not well resolved. Comparing the images to the observations obtained in Boehler et al. (2018), we find that the second colum matches the observations best. This sugests that, to match the observations using the VSI, the disk would need to be around 5 to 10 times more massive, similar to the values reported by Casassus et al. (2019) using VLA observations.

We de-project the images of the disks into polar coordinates accounting for the chosen inclination. From these de-projected images we calculate the ratio between the vortex maximum intensity I_{max} and the average intensity in the ring at the corresponding radius I_{Ring}. We find the ratio to be 7.0 and 7.8 for the inner and outer vortex, respectively, for the least massive case $\Sigma_0 = 1\ \Sigma_{\text{ref}}$. These ratios lower to 2.6 and 2.4, respectively, for the case with $\Sigma_0 = 10\ \Sigma_{\text{ref}}$ and to 1.28 and 1.13 in the most massive case. Therefore the cases with lower gas masses are favoured when comparing our models to the observations of MWC 758, where ratios of 2.6 and 4.0 have been reported (Boehler et al. 2018).

We also looked at the position of the $\tau = 1$ surface for the case of a face-on viewed disk. We find that for the least massive case only the inner part of the disk containing the large grains is optically thick, whereas for the ten times more massive case the entire vortex is at least marginally optically thick. In the 25 and 50 Σ_{ref} cases also the background disk is optically thick, favouring again the less massive disk cases presented in comparison to observations. Also, the emission in the more massive disk cases is likely dominated by the less massive grains compared to the less massive disks, as the largest grains settle to heights in the disk that are invisible to sub-mm wavelengths under these conditions.

5.3.2 Dependence on Turbulence

In the images discussed above, we only vary the column density normalization of the disk to influence the Stokes number of the particles. Looking at equation 5.7, we find that varying the turbulence strength δ has the same effect on the Stokes number as the gas density normalisation, because:

$$S = \frac{a_\bullet \, \rho_\bullet}{\rho_\mathrm{g} \, H \, \delta} \propto \frac{1}{\delta \, \Sigma_0} \qquad . \tag{5.9}$$

We compared the effect of using $\delta = 10^{-4}$ and $\Sigma_0 = 10\Sigma_\mathrm{ref}$ to both the 1 and 10 Σ_ref cases from above. Because of the assumption of $\alpha = \delta$, the particles now settle closer to the midplane as in the above cases. Therefore, the effects of varying δ and Σ_0 while keeping St fixed does not lead to identical results. The disk now has an overall intensity closer to the 10 Σ_ref, whereas the shape of the vortices is comparable to the 1 Σ_ref case. The size of the region having $\tau > 1$ is in between the 1 and 10 Σ_ref cases, indicating that due to the different settling heights of the particles in the lower turbulence the optical properties change and with them the grain sizes we actually observe.

5.3.3 Limitations of the Model

In this chapter, we use a steady state model of dust trapping in vortices using a diffusion-concentration equilibrium. Additionally, we limited our analysis to only one parameter, the gas reference column density. We now briefly discuss the implications of these limitations.

Disk mass: As already stated above, we only vary the reference column density of the gas phase in our models. This leads to massive disks for the 2 largest column densities used in this chapter. The most massive disk has a total gas mass larger than 0.1 $M_\odot$, making it likely for the disk to be gravitationally unstable. We still chose to present these models, as a change in the grain properties could lower the disk mass enough to make the model viable.

Grain Properties: Equation 5.7 also shows that intrinsic grain properties influence the Stokes number of the particles and therefore their spatial distribution inside the vortex. Particles with lower intrinsic density will have a lower Stokes number for the same particle size and disk properties used in this chapter. This would lead to them being spatially more extended, possibly allowing the vortex to be spatially resolved at the wavelength considered even at the lowest disk mass used, closer resembling observations. However, introducing porosity or mixed species grains would also change the opacities of the grains. This goes beyond the scope of this chapter, but should be considered when using more realistic dust-gas models of protoplanetary disks.

Turbulence prescription: We assumed that the turbulent dust diffusion parameter δ equals the turbulent angular momentum transport parameter α. This may not be the case in vortices or the VSI active disk in general. Several instabilities may change δ significantly inside the vortex, e.g. the Streaming Instability (SI). A higher δ inside the vortex would prevent the particles form concentrating in the center, showing a wider vortex signal. Additionally, SI may not concentrate the particles in the center of the vortex, but in filaments (Raettig et al. 2015), also leading to an extended signal. This is especially true for the lowest Σ_0 model, as the dust to gas ratio for the largest grains rises above unity, so they would start to dominate the gas flow and trigger the SI. Also the Stokes numbers are higher than 0.1 throughout the disk for the 1mm grains, suggesting that they would get destructed due to high relative velocities (Birnstiel et al. 2010). To model this correctly, realistic simulations using two-way drag forces in dust-gas simulations in vortices measuring both α and δ are needed.

Vortex evolution: The vortices in our analysis are relatively young (200 and 120 orbits at their local radii), so the vortices may still be adjusting to the disk surrounding and get stronger as time progresses. Also, vortices have been shown to be amplified by the SBI mechanism, which is also active in regions that are dominated by the VSI (Pfeil & Klahr 2019). So it is likely that the vortex would gain strength in time, enabling it to trap particles more efficiently. Additionally, we showed in chapter 3 that the vortices migrate and merge and also new vortices form, making the intensity maps calculated in this chapter a snapshot view of an evolving system.

5.4 Conclusions

In this chapter we applied the diffusion-concentration equilibrium dust model for vortices presented by LL13 to the fully turbulent 3D protoplanetary disk models from chapter 3. We find that the particles concentrated in vortices generated in VSI turbulent disk can explain the observed asymmetries in protoplanetary disks commonly explained through the presence of giant planets. The vortices generated in the disk, especially the outer vortex in our case, are large enough and can attract enough dust mass to be spatially resolved in typical ALMA observations. Our model is also able to match the peak to average intensity ratio of of observed vortices for gas surface density values of 5 to 10 times the value estimated from observations, consistent with recent estimates from Casassus et al. (2019). Therefore there does not have to be a planet present to seed the vortex, which would naturally explain the non-detection of giant planets inside the disk gaps.

In our analysis, we use a simplified model and restrict it to varying only the reference column density and turbulence strenght. A thorough model of dust within the VSI would need the direct calculation of the coupled dust-gas equations, which is rather expensive. Our results nevertheless show that computational models including dust are warranted, as they will lead to new, additional models explaining observations. Additionally, these simulations will be able to model the dust in the disk both in sub-mm emission and in near infrared scattered light, possibly showing distinguishing criteria between the planet and the disk instability models.

CHAPTER 6

SUMMARY AND OUTLOOK

6.1 Summary

Idenftifing large scale structure formation in the turbulent protoplanetary disk is a crucial ste in the current paradigm of planet formation. Without a localized pressure maximum furming in the early gas-dominated disk, the dust density enhancement necessary to enable gravo-turbulent planetesimal formation is hard to achieve. In this dissertation, I investigated whether the turbulence generated by the Vertical shear instability is able to generate the necessary structures. To this end, I conducted high resolution 3 dimensional global simulations using the grid based hydrodynamics code PLUTO.

While chapters 1 and 2 provide an introduction into the topic and the physical processes relevant to this work, chapter 3 presents the first simulations of the VSI that show non-axisymmetric large scale structures in the form of vortices forming in the disk. The vortices I find have a radial extent of about 1.5 local disk scale heights and an aspect ratio $\chi > 8$ and persist for more than 500 orbits, which is ideal fo trap particles with small to moderate stokes numbers. I also present evidence to support the theory that a secondary Rossby-Wave-Instability is active in the disk and is the cause of the vortices I observe.

The characterization of the turbulence generated by the VSI shows that it is sufficient to facilitate angular momentum transport in agreement with previous studies of the instability (Stoll & Kley 2014; Flock et al. 2017b) latest models of planetesimal formation (Drążkowska & Alibert 2017). It also shows that the angular momentum transport in disks with this instability present is not transported outward purely radially, but rather in an first upward then outward directed fashion, largely due to the anisotropy of the turbulent stresses generated (Stoll et al. 2017). Additionaly, the root-mean-squared velocities and α-values measured are dependent on the vertical distance from the midplane of the disk. I therefore advise caution when one compares simulations and observations, especially if the depth probed by the observation is not well constrained.

On the numerical side , I show that one of the shortcomings of previous models was the trade-off of physical azimuthal disk extend for higher numerical resolution, as simulations with azimuthal disk extends smaller than 180° do not accurately capture the non-axisymmetric features of the saturated VSI.

Armed with this finding of vortices in VSI turbulence, I present the first global high resolution parameter study of the instability in chapter 4. The study shows that vortex formation and survival is neither dependent on the disks density gradient nor the aspect ratio, meaning vortices can potentially form everywhere in the disk as long as the conditions for the VSI to operate are fulfilled. The vortices I find have radial sizes of 1 to 1.5 local scale heights H independent of the value of H, making the measured size of the vortex a possible indicator of the disks current pressure scale height and therefore its current temperature.

The vortices in the disks are generally found to be long lived, similar to the ones found in chapter 3 and are shown to regularly absorb weaker vortices (re-)forming continuously in the disk, possibly due to the underlying VSI permanently rebuilding the vorticity gradient of necessary for the RWI to operate.

Chapter 5 then addresses the question whether the vortices found in the simulations of the previous chapters can be detected in observations. Because the simulations of chapters 3 and 4 are performed for the gas phase of the disk only, I use an analytic model of the dust density in a steady state vortex to perform radiative transfer calculations of the expected dust phase of the disk. The results show that the vortices seeded in VSI active disks can be readily observed with current sub-mm telescopes and that for moderate disk densities our model already reasonably matches the current observations of the MWC 758 disk (Boehler et al. 2018; Dong et al. 2018).

As a general conclusion to the work presented in this dissertation, I like to say that the vortices shown to be generated in VSI turbulence are an important puzzle piece to understand planetesimal formation in the early phases of protoplanetary disk evolution. The fact that the vortices can form relatively early after the onset of the disk instability (after ca. 4000 yrs at 5Au around a solar mass star) aides in the understanding of the formation of gas giant planets and the fact that the formation is not tied to a specific place in the disk as it is with the mhd dead zone models may help explain the formation of the cores of the ice giants in our solar system and other massive companions on wide orbits. From the observational side, I would like to remark that although the planet model may be the most readily applicable model to explain vortex-like structures in disks, the recent non-detections of sufficiently massive planets in observations combined with work presented here and in other studies should lead to a reconsideration of other, non-planet related sources of structures in protoplanetary disks.

6.2 Outlook

The simulations presented in this thesis use a simplified cooling prescription force the disk to have a short cooling time beneficial to the growth of the VSI. This prescription is excellent if one is interested in the specifics of the instability itself, but it does not accurately represent the reality of protoplanetary disks, which are governed by viscous and radiative heating and cooling processes. Therefore, future simulations should shift their treatment of heating and cooling to radiation hydrodynamical models to obtain more accurate predictions of the features present in actual protoplanetary disks. The simplified prescription should be reserved for investigations into the structure and origin of the turbulence generated by the instability in question.

To this end, the parameter study presented in chapter 4 should be continued to investigate the remaining free parameters governing the VSI, namely the disk temperature gradient q and the cooling time τ. Further investigations are also required to better understand the mechanisms behind the non Kolmogorov like structure of the turbulence and the formation of the vortices.

Additionally, although the motivation for the search for structures forming in turbulent protoplanetary disks is mainly the concentration of dust in particle traps, the numerical simulations presented in this work do not include the dust phase. Future simulations of the VSI should change this. Simulations using passively coupled tracer particles or using low dust to gas ratios should further investigate the results presented in chapter 5. Also, recent simulations using the full two-way drag coupling of the gas showed that a high concentration of dust particles modifies the buoyancy of the disk gas and can therefore suppress the mechanism driving VSI turbulence, especially near the midplane of the disk (Lin & Youdin 2017; Lin 2019). Future simulations using two-way drag should therefore investigate whether vortex formation is still possible in dusty protoplanetary disk environments and if additional new constraints emerge from the treatment of the dust phase.

Appendix **A**

List of Figures and Tables

A.1 List of Figures

A.2 List of Tables

LIST OF OWN PUBLICATIONS

List of first-author papers used in this thesis

Here I list all first-author papers already published or in preparation that are used in this thesis.

- **N. Manger** and H. Klahr. *Vortex formation and survival in protoplanetary discs subject to vertical shear instability*. MNRAS, 480:2125–2136, 2018.
- **N. Manger** and H. Klahr. *Vortex Signatures can be produced by Vertical Shear Instability*. A&A, 2019 subm.
- **N. Manger**, H. Klahr, W. Kley and M. Flock in prep.

Appendix C

Bibliography

Adams, F. C., Lada, C. J., & Shu, F. H. 1987, ApJ, 312, 788

Adams, F. C. & Watkins, R. 1995, ApJ, 451, 314

ALMA Partnership, Brogan, C. L., Pérez, L. M., et al. 2015, ApJ, 808, L3

Andre, P., Ward-Thompson, D., & Barsony, M. 1993, ApJ, 406, 122

Andrews, S. M., Wilner, D. J., Hughes, A. M., Qi, C., & Dullemond, C. P. 2009, ApJ, 700, 1502

Ansdell, M., Williams, J. P., van der Marel, N., et al. 2016, ApJ, 828, 46

Arlt, R. & Urpin, V. 2004, A&A, 426, 755

Armitage, P. J. 2009, "Astrophysics of Planet Formation" (Cambridge University Press)

Armitage, P. J. 2011, Annual Review of Astronomy and Astrophysics

Armitage, P. J. 2019, Saas-Fee Advanced Course, 45, 1

Bai, X.-N. & Stone, J. M. 2010, The Astrophysical Journal, 722, 1437

Balbus, S. A. & Hawley, J. F. 1991, Astrophysical Journal, 376, 214

Barge, P. & Sommeria, J. 1995, A&A, 295, L1

Barranco, J. A. & Marcus, P. S. 2005, ApJ, 623, 1157

Barranco, J. A., Pei, S., & Marcus, P. S. 2018, ApJ, 869, 127

Baruteau, C., Barraza, M., Pérez, S., et al. 2019, MNRAS, 768

Bell, K. R., Cassen, P. M., Klahr, H. H., & Henning, T. 1997, ApJ, 486, 372

Benisty, M., Juhasz, A., Boccaletti, A., et al. 2015, A&A, 578, L6

Birnstiel, T., Dullemond, C. P., & Brauer, F. 2009, A&A, 503, L5

Birnstiel, T., Dullemond, C. P., & Brauer, F. 2010, A&A, 513, A79

Birnstiel, T., Fang, M., & Johansen, A. 2016, Space Sci. Rev., 205, 41

Bjorkman, J. E. & Wood, K. 2001, ApJ, 554, 615

Blum, J. & Wurm, G. 2008, Annual Review of Astronomy and Astrophysics, 46, 21

Boehler, Y., Ricci, L., Weaver, E., et al. 2018, ApJ, 853, 162

Bohren, C. F. & Huffman, D. R. 1983, Absorption and scattering of light by small particles (Wiley, New York)

Brauer, F., Dullemond, C. P., & Henning, T. 2008, A&A, 480, 859

Carrasco-González, C., Henning, T., Chandler, C. J., et al. 2016, ApJ, 821, L16

Carrera, D., Johansen, A., & Davies, M. B. 2015, A&A, 579, A43

Casassus, S., Marino, S., Lyra, W., et al. 2019, MNRAS, 483, 3278

Cazzoletti, P., van Dishoeck, E. F., Pinilla, P., et al. 2018, ArXiv e-prints, arXiv:1809.04160

Clarke, C. & Carswell, B. 2007, Principles of Astrophysical Fluid Dynamics (Cambridge University Press)

Cuzzi, J. N., Hogan, R. C., Paque, J. M., & Dobrovolskis, A. R. 2001, ApJ, 546, 496

Davis, S. W., Stone, J. M., & Pessah, M. E. 2010, ApJ, 713, 52

Dittrich, K., Klahr, H., & Johansen, A. 2013, Astrophysical Journal, 763, 117

Dominik, C. & Tielens, A. G. G. M. 1997, ApJ, 480, 647

Dong, R., Liu, S.-y., Eisner, J., et al. 2018, ApJ, 860, 124

Drazin, P. G. & Reid, W. H. 2004, "Hydrodynamic Stability" (Cambridge University Press)

Drążkowska, J. & Alibert, Y. 2017, A&A, 608, A92

Dubrulle, B., Morfill, G., & Sterzik, M. 1995, Icarus, 114, 237

Dullemond, C. P. 2013, Radiative transfer in astrophysics, Lecture notes, http://www.ita.uni-heidelberg.de/dullemond/lectures/radtrans_2013/index.shtml

Dullemond, C. P., Juhasz, A., Pohl, A., et al. 2012, RADMC-3D: A multi-purpose radiative transfer tool

Dzyurkevich, N., Flock, M., Turner, N. J., Klahr, H., & Henning, T. 2010, Astronomy and Astrophysics, 515, A70

Dzyurkevich, N., Turner, N. J., Henning, T., & Kley, W. 2013, ApJ, 765, 114

Flock, M., Fromang, S., Turner, N. J., & Benisty, M. 2017a, ApJ, 835, 230

Flock, M., Nelson, R. P., Turner, N. J., et al. 2017b, ApJ, 850, 131

Flock, M., Ruge, J. P., Dzyurkevich, N., et al. 2015, A&A, 574, A68

Fricke, K. 1968, Zeitschrift für Astrophysik, 68, 317

Fromang, S. & Nelson, R. P. 2005, MNRAS, 364, L81

Fu, W., Li, H., Lubow, S., & Li, S. 2014, ApJ, 788, L41

Gammie, C. F. 1996, ApJ, 457, 355

Garaud, P., Meru, F., Galvagni, M., & Olczak, C. 2013, ApJ, 764, 146

Godon, P. & Livio, M. 1999, ApJ, 523, 350

Godunov, S. K. 1959, Matematicheskii Sbornik, 47(89), 271

Goldreich, P. & Schubert, G. 1967, Astrophysical Journal, 150, 571

Goodman, J., Narayan, R., & Goldreich, P. 1987, MNRAS, 225, 695

Hayashi, C. 1981, Progress of Theoretical Physics Supplement, 70, 35

Hess, S. L. 1969, Icarus, 11, 218

Johansen, A., Blum, J., Tanaka, H., et al. 2014, Protostars and Planets VI, 547

Johansen, A. & Klahr, H. 2005, ApJ, 634, 1353

Johansen, A., Klahr, H., & Henning, T. 2006, ApJ, 636, 1121

Johansen, A., Klahr, H., & Henning, T. 2011, Astronomy & Astrophysics, 529, A62

Johansen, A., Mac Low, M.-M., Lacerda, P., & Bizzarro, M. 2015, Science Advances, 1, 1500109

Johansen, A., Oishi, J. S., Mac Low, M.-M., et al. 2007, Nature, 448, 1022

Johansen, A., Youdin, A., & Klahr, H. 2009, ApJ, 697, 1269

Kant, I. 1755, Allgemeine Naturgeschichte und Theorie des Himmels oder Versuch von der Verfassung und dem mechanischen Ursprunge des ganzen Weltgebäudes nach Newtonischen Grundsätzen abgehandelt (Petersen, Königsberg and Leipzig)

Kataoka, A., Tanaka, H., Okuzumi, S., & Wada, K. 2013, A&A, 557, L4

Keppler, M., Benisty, M., Müller, A., et al. 2018, A&A, 617, A44

Klahr, H. & Bodenheimer, P. 2006, ApJ, 639, 432

Klahr, H. & Hubbard, A. 2014, The Astrophysical Journal, 788, 21

Klahr, H., Pfeil, T., & Schreiber, A. 2018, in Handbook of Exoplanets (Springer International Publishing AG)

Klahr, H. & Schreiber, A. 2016, in IAU Symposium, Vol. 318, Asteroids: New Observations, New Models, ed. S. R. Chesley, A. Morbidelli, R. Jedicke, & D. Farnocchia, 1–8

Klahr, H. H. & Bodenheimer, P. 2003, ApJ, 582, 869

Klahr, H. H. & Henning, T. 1997, Icarus, 128, 213

Klahr, H. H., Henning, T., & Kley, W. 1999, ApJ, 514, 325

Kratter, K. & Lodato, G. 2016, Annual Review of Astronomy and Astrophysics, 54, 271

Krijt, S., Ormel, C. W., Dominik, C., & Tielens, A. G. G. M. 2015, A&A, 574, A83

Lada, C. J. 1987, in IAU Symposium, Vol. 115, Star Forming Regions, ed. M. Peimbert & J. Jugaku

Lada, C. J. & Wilking, B. A. 1984, ApJ, 287, 610

Laplace, P. S. d. 1796, Exposition du Systéme du Monde (Imprimerie Cercele-Social, Paris)

Latter, H. N. & Papaloizou, J. 2018, MNRAS, 474, 3110

Lesur, G., Kunz, M. W., & Fromang, S. 2014, A&A, 566, A56

Lesur, G. & Papaloizou, J. C. B. 2009, A&A, 498, 1

Lesur, G. & Papaloizou, J. C. B. 2010, A&A, 513, A60

Li, H., Colgate, S. A., Wendroff, B., & Liska, R. 2001, ApJ, 551, 874

Li, H., Finn, J. M., Lovelace, R. V. E., & Colgate, S. A. 2000, ApJ, 533, 1023

Lin, M.-K. 2012a, ApJ, 754, 21

Lin, M.-K. 2012b, MNRAS, 426, 3211

Lin, M.-K. 2019, MNRAS, 485, 5221

Lin, M.-K. & Youdin, A. N. 2015, ApJ, 811, 17

Lin, M.-K. & Youdin, A. N. 2017, ApJ, 849, 129

Lobo Gomes, A., Klahr, H., Uribe, A. L., Pinilla, P., & Surville, C. 2015, ApJ, 810, 94

Lovelace, R. V. E., Li, H., Colgate, S. A., & Nelson, A. F. 1999, ApJ, 513, 805

Lynden-Bell, D. & Pringle, J. E. 1974, MNRAS, 168, 603

Lyra, W. 2014, ApJ, 789, 77

Lyra, W., Johansen, A., Zsom, A., Klahr, H., & Piskunov, N. 2009, A&A, 497, 869

Lyra, W. & Klahr, H. 2011, A&A, 527, A138

Lyra, W. & Lin, M.-K. 2013, ApJ, 775, 17

Lyra, W. & Mac Low, M.-M. 2012, ApJ, 756, 62

Lyra, W., Raettig, N., & Klahr, H. 2018, Research Notes of the American Astronomical Society, 2, 195

Lyra, W. & Umurhan, O. 2018, arXiv e-prints, arXiv:1808.08681

Manger, N. & Klahr, H. 2018, MNRAS, 480, 2125

Marcus, P. S., Pei, S., Jiang, C.-H., & Barranco, J. A. 2016, ApJ, 833, 148

Marcus, P. S., Pei, S., Jiang, C.-H., et al. 2015, ApJ, 808, 87

Marino, S., Casassus, S., Perez, S., et al. 2015, ApJ, 813, 76

Mayor, M. & Queloz, D. 1995, Nature, 378, 355

McNally, C. P., Nelson, R. P., Paardekooper, S.-J., & Benítez-Llambay, P. 2019, MNRAS, 484, 728

Meheut, H., Casse, F., Varniere, P., & Tagger, M. 2010, A&A, 516, A31

Meheut, H., Lovelace, R. V. E., & Lai, D. 2013, MNRAS, 430, 1988

Meheut, H., Meliani, Z., Varniere, P., & Benz, W. 2012, Astronomy and Astrophysics, 545, A134

Mie, G. 1908, Annalen der Physik, 330, 377

Mignone, A. 2014, Journal of Computational Physics, 270, 784

Mignone, A., Bodo, G., Massaglia, S., et al. 2007, The Astrophysical Journal Supplement Series, 170, 228

Nakagawa, Y., Sekiya, M., & Hayashi, C. 1986, Icarus, 67, 375

Nelson, R. P., Gressel, O., & Umurhan, O. M. 2013, Monthly Notices of the Royal Astronomical Society, 435, 2610

Okuzumi, S., Tanaka, H., Kobayashi, H., & Wada, K. 2012, ApJ, 752, 106

Ormel, C. W., Spaans, M., & Tielens, A. G. G. M. 2007, A&A, 461, 215

Paardekooper, S.-J., Lesur, G., & Papaloizou, J. C. B. 2010, ApJ, 725, 146

Papaloizou, J. C. B. & Pringle, J. E. 1984, MNRAS, 208, 721

Papaloizou, J. C. B. & Pringle, J. E. 1985, MNRAS, 213, 799

Paszun, D. & Dominik, C. 2009, A&A, 507, 1023

Pedlosky, J. 1992, Geophysical Fluid Dynamics, Springer study edition (Springer New York)

Pérez, L. M., Carpenter, J. M., Andrews, S. M., et al. 2016, Science, 353, 1519

Pérez, L. M., Isella, A., Carpenter, J. M., & Chandler, C. J. 2014, ApJ, 783, L13

Petersen, M. R., Julien, K., & Stewart, G. R. 2007a, ApJ, 658, 1236

Petersen, M. R., Stewart, G. R., & Julien, K. 2007b, ApJ, 658, 1252

Pfeil, T. & Klahr, H. 2019, ApJ, 871, 150

Pohl, A. 2018, PhD thesis, Heidelberg University

Raettig, N., Klahr, H., & Lyra, W. 2015, ApJ, 804, 35

Raettig, N., Lyra, W., & Klahr, H. 2013, ApJ, 765, 115

Raymond, S. N., Kokubo, E., Morbidelli, A., Morishima, R., & Walsh, K. J. 2014, in Protostars and Planets VI, ed. H. Beuther, R. S. Klessen, C. P. Dullemond, & T. Henning, 595

Rhines, P. B. 1975, Journal of Fluid Mechanics, 69, 417

Richard, S., Barge, P., & Le Dizès, S. 2013, A&A, 559, A30

Richard, S., Nelson, R. P., & Umurhan, O. M. 2016, MNRAS, 456, 3571

Roddenberry, G. 1987-1994, Star Trek: The Next Generation (USA: Paramount Domestic Television)

Rüdiger, G., Arlt, R., & Shalybkov, D. 2002, A&A, 391, 781

Rybicki, G. B. & Lightman, A. P. 1986, Radiative Processes in Astrophysics (Wiley-VCH)

Safronov, V. S. 1972, ”Evolution of the protoplanetary cloud and formation of the earth and planets.” (Jerusalem (Israel): Israel Program for Scientific Translations, Keter Publishing House)

Schreiber, A. 2018, PhD thesis, Heidelberg University

Shakura, N. I. & Sunyaev, R. A. 1973, Astronomy and Astrophysics, 24, 337

Steinacker, J., Baes, M., & Gordon, K. D. 2013, ARA&A, 51, 63

Stoll, M. H. R. & Kley, W. 2014, A&A, 572, A77

Stoll, M. H. R. & Kley, W. 2016, A&A, 594, A57

Stoll, M. H. R., Kley, W., & Picogna, G. 2017, A&A, 599, L6

Stone, J. M., Gardiner, T. A., Teuben, P., Hawley, J. F., & Simon, J. B. 2008, ApJS, 178, 137

Surville, C. & Barge, P. 2015, A&A, 579, A100

Surville, C., Mayer, L., & Lin, D. N. C. 2016, ApJ, 831, 82

Tassoul, J.-L. 1978, Theory of rotating stars (Princeton: University Press)

Testi, L., Birnstiel, T., Ricci, L., et al. 2014, in Protostars and Planets VI, ed. H. Beuther, R. S. Klessen, C. P. Dullemond, & T. Henning, 339

Thompson, M. J. 2006, An introduction to astrophysical fluid dynamics (London: Imperial College Press)

Toro, E. F. 2009, Riemann Solvers and Numerical Methods for Fluid Dynamics (Springer-Verlag Berlin Heidelberg)

Turner, N. J., Fromang, S., Gammie, C., et al. 2014, Protostars and Planets VI, 411

Urpin, V. 2003, A&A, 404, 397

van der Marel, N., Cazzoletti, P., Pinilla, P., & Garufi, A. 2016, ApJ, 832, 178

van der Marel, N., Pinilla, P., Tobin, J., et al. 2015, ApJ, 810, L7

van der Marel, N., van Dishoeck, E. F., Bruderer, S., et al. 2013, Science, 340, 1199

Varnière, P. & Tagger, M. 2006, A&A, 446, L13

Weidenschilling, S. J. 1977, Monthly Notices of the Royal Astronomical Society, 180, 57

Weidenschilling, S. J. 1977, Ap&SS, 51, 153

Weizsäcker, C. F. 1948, Zeitschrift Naturforschung Teil A, 3, 524

Weizsäcker, C. F. v. 1943, Zeitschrift fur Astrophysik, 22, 319

Whipple, F. L. 1972, in From Plasma to Planet, ed. A. Elvius, 211

Windmark, F., Birnstiel, T., Ormel, C. W., & Dullemond, C. P. 2012, A&A, 544, L16

Woolfson, M. M. 1993, Quarterly Journal of the Royal Astronomical Society, 34, 1

Wurm, G., Paraskov, G., & Krauss, O. 2005, Icarus, 178, 253

Youdin, A. & Johansen, A. 2007, ApJ, 662, 613

Youdin, A. N. & Goodman, J. 2005, ApJ, 620, 459

Youdin, A. N. & Lithwick, Y. 2007, Icarus, 192, 588

Zsom, A., Ormel, C. W., Güttler, C., Blum, J., & Dullemond, C. P. 2010, A&A, 513, A57

ACKNOWLEDGEMENTS

As the work on this dissertation, and with it a chapter of my life, comes to a close, I would like to thank the people who accompanied and supported me on this journey.

First and foremost, I would like to thank my supervisor Hubert Klahr for supporting me throughout these years. I am very grateful for the opportunity to join the planet formation theory group at MPIA and for the continued trust he put in me, allowing me to do both my Master and PhD research under his supervision, even though at times I was less than an easy personality to deal with. I am very grateful for the opportunity to learn about hydrodynamic instabilities from him and also for the many on and off topic discussions we had throughout these years. I am also very grateful for his support during my times of crisis and allowing me to take the time and space I needed, and also for being the person I could try more than a few psychology lessons out on.

Next, I would like to thank my colleagues from the scientific community. I especially thank Cornelis Dullemond for agreeing to be on my thesis committee and also for the many helpful discussions we had over the years. Adriana Pohl for introducing me to the world of radiative transfer simulations. Mario Flock and Wilhelm Kley for their very helpful comments on my work and some new insights on the VSI that will keep me occupied even in the future. Thanks to all of my colleagues for their kind help with any questions and problems I had along the way.

Also, I want to thank the members of the PSF theory group. Although they are to numerous to mention, thank you all for being such an awesome group and always making me feel welcome. Special thanks go to my Elsässer office mates Christian Lenz and Hans Baehr for putting up with my random questions and comments and to Andreas Schreiber for talking me into joining the Star Wars cinema trips – I would have missed out on something awesome.

Last but not least, I want thank my family for their loving support all those years. My mum, for always believing in me and picking me up when I am down. For always having an open ear and encouraging me to reach for the stars – both literally and figuratively. Thank you. None of this would have been possible with out you. My dad, for always keeping me on my toes when arguing science with him. And lastly, thanks to my awesome brother, Marcel, for being a down to earth constant in my life and for all the times I could borrow his couch if I needed to visit home.

DECLARATION/ERKLÄRUNG

I hereby assure that I have written this work independently and have used no other than the specified resources.

Ich versichere, dass ich diese Arbeit selbstständig verfasst habe und keine anderen als die angegebenen Quellen und Hilfsmittel benutzt habe.

Heidelberg, June 1, 2019

....

Natascha Manger

Disks around young stars are the birth place of planetary systems like our own solar system. Thus, the study of turbulent processes in protoplanetary disks is not only important to understand the transport of angular momentum to explain for example the angular momentum deficit of our own sun, but also to understand how large scale structures emerge, which are recently regularly observed and which also represent a crucial puzzle piece in the understanding of how dust grains can grow into planetesimals via gravoturbulent processes.

In this thesis, I conduct high resolution studies of three-dimensional global models of turbulent protoplanetary disks using the magneto-hydrodynamics code PLUTO. I focus my studies on the Vertical Shear Instability (VSI), which has been shown to operate efficiently at disk radii beyond a few AU in typical protoplanetary disks.

I show that vortices with radial diameters of around 1.5 local pressure scale heights and aspect ratios $\chi > 8$ form in VSI turbulent disks and that these vortices can survive more than 500 orbits. The vortices are forming irrespective of the underlying disk density gradient and aspect ratio and can therefore act as pressure traps for small to medium sized particles over a wide range of the disk. I also show evidence that these dusty vortices are compatible with detections of dust concentrations by current sub-mm interferometers. These findings therefore present a crucial puzzle piece which will help the understanding under which conditions and how early after the formation of a disk around a young star planetesimals can form via gravoturbulent planetesimal formation.

Front cover: Artist impression of a dusty protoplanetary disk ©*NASA/JPL-Caltech*